Development of Statistical Models for Functional Near-infrared Spectroscopy Data Analysis Incorporating Anatomy and Probe Registration Prior Information

by

Xuetong Zhai

Master of Science, University of Pittsburgh, Pittsburgh, PA, 2014
Bachelor of Engineering, Huazhong University of Science and Technology, Wuhan, China, 2012

Submitted to the Graduate Faculty of
the Swanson School of Engineering in partial fulfillment
of the requirements for the degree of

Doctor of Philosophy

University of Pittsburgh

2020

UNIVERSITY OF PITTSBURGH

SWANSON SCHOOL OF ENGINEERING

This dissertation was presented

by

Xuetong Zhai

It was defended on

November 6, 2020

and approved by

Theodore Huppert, Ph.D., Associate Professor,

Department of Electrical and Computer Engineering

George Stetten, M.D., Ph.D., Professor

Department of Bioengineering

Howard Aizenstein, M.D., Ph.D., Professor

Department of Psychiatry

Robert Krafty, Ph.D., Professor

Department of Biostatistics and Bioinformatics, Emory University

Dissertation Director: Theodore Huppert, Ph.D., Associate Professor,

Department of Electrical and Computer Engineering

Development of Statistical Models for Functional Near-infrared Spectroscopy Data Analysis Incorporating Anatomy and Probe Registration Prior Information

Xuetong Zhai, PhD

University of Pittsburgh, 2020

Functional near-infrared spectroscopy (fNIRS) is a non-invasive technology that uses low-levels of non-ionizing light in the range of 650 – 900 nm (red and near-infrared) to record changes in the optical absorption and scattering of tissue. In particular, oxy-hemoglobin (HbO) and deoxy-hemoglobin (HbR) have characteristic absorption spectra at these wavelengths, which are used to discriminate blood flow and oxygen metabolism changes. As compared with functional magnetic resonance imaging (fMRI), fNIRS is less costly, more portable, and allows for a wider range of experimental scenarios because it neither requires a dedicated scanner nor needs the subject to lay supine.

Current challenges in fNIRS data analysis include: (i) a small change in brain anatomy or optical probe positioning can create huge differences in fNIRS measurements even though the underlying brain activity remains the same due to the existence of "blind-spots"; (ii) fNIRS image reconstruction is a high-dimensional, under-determined, and ill-posed problem, in which there are thousands of parameters to estimate while only tens of measurements available and existing methods notably overestimate the false positive rate; (iii) brain anatomical information has rarely been used in current fNIRS data analyses.

This dissertation proposes two new methods aiming to improve fNIRS data analysis and overcome these challenges – one of which is a channel-space method based on anatomically defined region-of-interest (ROI) and the other one is an image reconstruction method incorporating anatomical and physiological prior information. The two methods are developed using advanced statistical models including a combination of regularization models and Bayesian hierarchical modeling. The performance of the two methods is validated via numerical simulations and evaluated using receiver operating characteristics (ROC)-based tools. The statistical comparisons with conventional methods suggest significant improvements.

Table of Contents

List of Tables

List of Figures

Preface

The purpose of this dissertation is to develop new statistical models to improve functional near-infrared spectroscopy (fNIRS) data analysis. The original motivation of this project arose from the limitations of fNIRS due to its "blind-spots" effects and the nature of ill-posed inverse problems. The methods proposed in this dissertation include a taper-weighted contrast vector to statistically test the non-involvement of specific brain regions in an evoked task and a Bayesian hierarchical model for fNIRS image reconstruction. Both methods utilize prior information such as brain anatomy and probe registration. These methods are supposed to be of interest to life scientists using fNIRS imaging in their studies and engineers/statisticians developing analysis methods for fNIRS data.

The work presented in this dissertation could have never been completed without the support I received from many people on my PhD study journey. I would like to acknowledge and thank them in no particular order.

To my advisor Dr. Theodore Huppert, who has provided me outstanding mentorship. Thank you for your detailed guidance and continual support. I have learned so much from you not only the knowledge and skills but also your passion and insight into research works.

To my committee members, Drs. George Stetten, Howard Aizenstein, and Robert Krafty, for your excellent expertise, guidance, and support.

To my colleagues from Dr. Huppert's lab, Drs. Hendrik Santosa and James Hengenius, for your help in our collaboration and your valuable feedback on this dissertation manuscript.

To my previous advisor Dr. Dev Chakraborty for encouraging me to pursue a PhD degree and your guidance and support in the beginning years.

To the Department of Bioengineering and the Chair Dr. Sanjeev Shroff for the wonderful educational resources provided and the support during my transition period between labs.

To the University of Pittsburgh Center for Research Computing for the additional support through the computing resources provided.

To my whole family including my grandparents, aunts, uncles, cousins, etc., especially my parents Mr. Lizhong Zhai and Ms. Aimin Wang for your support, inspiration, and love.

1.0 Introduction

Functional near-infrared spectroscopy (fNIRS) is a non-invasive technology that uses low-levels of non-ionizing light in the range of 650 – 900 nm (red and near-infrared) to record changes in the optical absorption and scattering of tissue [1]. In particular, oxy-hemoglobin (HbO) and deoxy-hemoglobin (HbR) have characteristic absorption spectra at these wavelengths, which are used to discriminate blood flow and oxygen metabolism changes [2]. Typically, light is sent into the tissue from source positions on the scalp. This light diffuses through the tissue and a small fraction of the light is detected at a discrete set of optical detector positions placed several centimeters from the originating source position. These channel-space measurements are sensitive to changes in the optical properties of the tissue along this diffuse volume between the light source and detector. During an evoked functional task, the changes in blood flow and oxygenation in the brain result in fluctuations in optical absorption due to hemoglobin in this local region and this gives rise to changes in the fNIRS measurements in the source-detector pairs (channels) crossing this region. Using a grid of these optical source and detector positions embedded in a head probe, functional brain activity can be recorded from regions of the surface of the brain's cortex. Over the last three decades, fNIRS has been used in a variety of different brain imaging studies and populations (reviewed in [3, 4, 5, 6]). In particular, the ability to noninvasively record brain activity without participant immobilization or a specialized dedicated scanner environment (cf. magnetic resonance imaging; MRI) make this technique well suited for studies in pediatric populations (reviewed in [3, 7, 8, 9]). However, there exist limitations in the current fNIRS data analysis.

Problem 1: Channel-space fNIRS measurements are highly dependent on underlying brain structure.

fNIRS provides measurements of evoked functional changes in the brain during cognitive tasks; however, this method does not give any direct information about either the underlying structure or the anatomy of head. As a consequence, one challenge of fNIRS is that these measurements highly depend on the relative sensor positions on the scalp, which vary from subject to subject. Small displacements in the probe location, due to head size, anatomy or probe setup, can lead to huge differences in the measurement values in the channel-space, even if the underlying brain signals are exactly the same. Most current fNIRS studies utilize what is called a nearest-neighbor measurement geometry in which measurements are made between only the closest optical source-detector pairs. While these geometries are easier to set up on participants, a limitation of this approach is that these probes contain numerous "blind-spots" where there are underlying brain areas with little to no sensitivity from the measurements. In these setups, small displacements in the location of sensors can result in large differences in the measured amplitude of brain signals, even if the underlying brain activity remains the same. An example of this is demonstrated in Fig. 1.1, which shows how variations of probe placement with respect to changes in head size affect fNIRS measurements. This simulation has been set up to reflect the measurement geometry of the popular commercial Artinis Octomon fNIRS system. The top images show how the same probe, anchored on Fpz site (middle frontal-parietal) of the 10-20 system, will stretch to slightly different lateral positions as the head size varies. In this example using the projection of area superior frontal gyrus, the sensitivity of this probe varies in a complex way (by up to 5-fold) as this large area of the brain moves in and out of the measurement sensitivity profiles. This effect is even more detrimental for smaller/more focal activation areas. Note that the sensitivity "spikes" in Fig. 1.1 are actually due to the gyrus folding positions relative to the probe for this individual subject.

This is particularly problematic in cross-sectional or longitudinal studies of child development, where the head-size varies between sessions. Moreover, these measurements are also sensitive to inter-subject differences in head anatomy, such as skull thickness and depth of the brain relative to the skin's surface. Thus, this uncertainty increases variance across measurement sessions and reduces statistical effects sizes. This also makes studies of brain activation changes with child age and development difficult.

This "blind-spot" issue can be solved by using more sophisticated probe geometries. However, while we recognize this as a solution to this problem, currently more than 90% of existing fNIRS studies are based on nearest-neighbor probes. With the exception of the Cephalogics company and the NIRx DyNOT system, none of the commercial fNIRS

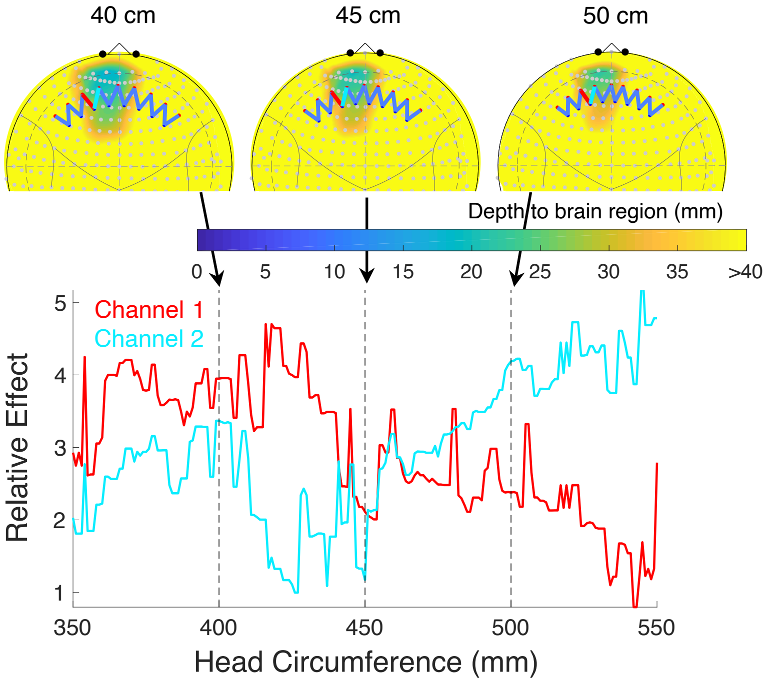

Figure 1.1: Changing the head size of a frontal fNIRS probe anchored on the forehead (Fpz) results in an up to 5-fold variation in the sensitivity to superior frontal gyrus. The top images show the location and depth (from scalp) of this region relative to the fNIRS probe. The two curves in the bottom plot are the relative sensitivity of the two correspondingly colored channels against head circumference.

systems support high density fNIRS measurements. In addition, from past experience, these high-density measurements generally take 2-3 fold longer to set up and adjust compared to simpler probe geometries. Thus, at the moment, these high-density measurements are neither practical nor possible for the majority of fNIRS labs and not a viable solution for existing fNIRS data.

An alternative approach to this would be to use an individual's response to a "localizer" functional task to define consistent underlying brain regions across participants. While, this data-driven approach makes less assumptions than atlas-based models (as will be detailed in this work) to define regions-of-interest, this method requires the ability to robustly measure a specific localizer task response for a given brain-region in each subject. This is not always possible since not all brain regions can be specifically and uniquely defined by localizer tasks, which may involve multiple regions of the brain. In addition, single-subject statistics are often not reliable enough to define individualized regions for many tasks or subject populations. Thus, while the use of a localizer task is recommended when possible, more generalizable solutions are also needed.

Methods for the spatial registration of the fNIRS head cap and measurement channels with respect to the brain have been described in previous work [10, 11, 12, 13]. Although not always possible or practical, fNIRS investigators often record this information with either a three-dimensional camera and registration system (e.g. [14]) or simply by using a tape measure to record head-size and potentially the location of the fNIRS sensors relative to the international 10-20 system. However, although this registration information is recorded as part of fNIRS experimental best-practices by many labs, there has been very little development of quantitative methods to actually quantitatively use this information within fNIRS analysis.

Problem 2: Image-space fNIRS estimates result in high type-I error.

A further consequence appears in fNIRS image reconstruction, which uses the optical absorption changes recorded from light diffusely traveling between the source and detector pairs to reconstruct low-resolution spatial images of the underlying blood flow changes. Such images are often difficult to accurately recover due to optical scattering in the tissue and the limited number of measurements. This means that there is not enough information in the measurements alone to yield accurate and unique estimates of images. Hence, an inverse model is used to estimate the changes within the brain from measurements made only on the head surface. Several different statistical approaches (regularization, Bayesian theory, etc.) for solving inverse problems have been used.

The current image reconstruction through implementations of statistical models are considerably skewed towards high type-I error. According to the preliminary result of simulations, ℓ_2 regularization models overestimates the false positive rate (FPR). In the simulation, a null image (only noise exists) is generated, and ℓ_2 regularization is used to reconstruct the image. The p-value of the significance testing indicates the probability to reject the null hypothesis that no activity is found in the region of interest (ROI). Since the null image contains no activity, the p-values under the null hypothesis should be evenly distributed. However, we found significantly more small p-values than expected. Fig. 1.2 is an example of the histogram of p-values for simulations under null hypothesis, from which we can see that the frequencies are skewed to zero. This problem is considered as the main limitation of the current image reconstruction methods.

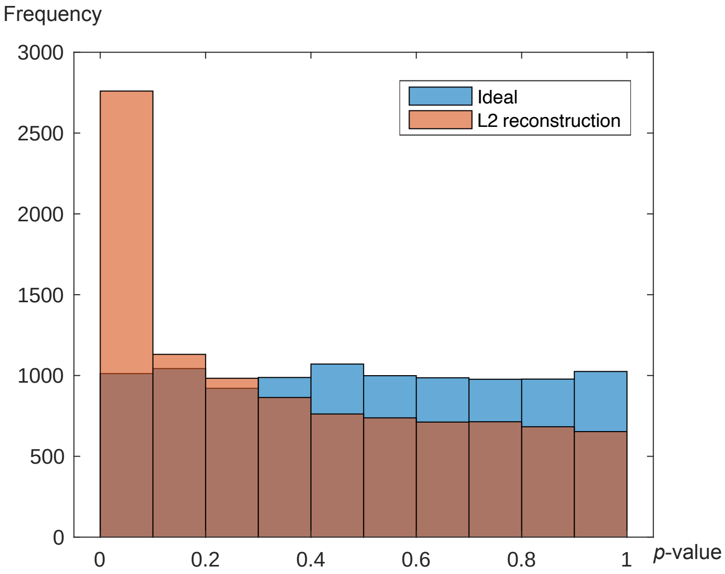

Figure 1.2: The histogram of p-values for 10,000 simulations using current image reconstruction and the ideal distribution under null hypothesis. It can be seen that the empirical p-values are skewed towards 0, i.e., high type-I error.

As we know, ℓ_2 regularization can only make the coefficients close to zero but not exactly equal to zero. However, there is no evoked activity (comparing with the baseline) in most areas of the cerebral cortex during an fNIRS experiment. This could be the reason for the overestimation of FPR that is the main limitation of the current ℓ_2-based reconstruction method. Previous studies show that ℓ_1 regularization (a.k.a., lasso) leads to sparsity (some of the regressors are zero in the result). Thus, a lower FPR is expected from ℓ_1 regularization. In traditional regularization, the coefficients are varied to minimize the loss function from a mathematical perspective. However, the coefficients in this problem represent the hemodynamic responses at each position in the cerebral cortex. The responses within each predefined anatomy region are usually similar but different from some of the other regions, since every region plays a role in the brain's functionality. Therefore, another innovation we propose is to group the coefficients per the anatomy information and use group lasso for the image reconstruction instead of conventional ℓ_1 regularization. All coefficients in a particular group will be included or excluded together in the model; this approach reduces the degrees of freedom of the inverse model. The final result is consequently expected to be more accurate and match the brain anatomy.

The overall objective of this dissertation is to develop more accurate statistical methods utilizing advanced models to improve both channel-space and image-space results incorporating cerebral anatomical information. Two approaches are respectively proposed to address the above two problems. First, we develop a fNIRS data analysis method based on anatomically defined regions-of-interest (ROI) to eliminate the effects of probe location. For the image reconstruction enhancement, we will use advanced statistical models to obtain a more accurate reconstructed image incorporating anatomical and physiological prior information. The two methods are developed using advanced statistical models including combination of regularization models and Bayesian hierarchical modeling. The performances of the two methods which will be compared to the existing reconstruction method using a receiver operating characteristics [15] (ROC)-based method.

This dissertation is organized as follows. Chapter 2 describes the propagation of near-infrared light in brain tissues and the forward model to describe the propagation. Chapter 3 shows several existing approaches for fNIRS data analysis. Chapter 4 provides the background of statistical approaches including the ROC analysis frequently used as the statistical testing method in the dissertation and Bayesian hierarchical modeling that is the main framework for the new image reconstruction model in Chapter 6. Chapter 5 and Chapter 6 fully describes the two major contribution of this dissertation including study significance, formulation of the new methods, simulation study setups, and results analyses, comparisons and discussions. Finally, Chapter 7 summarizes the entire dissertation and gives a discussion on potential future works.

2.0 Light Propagation in Brain Tissues

In this chapter, the propagation of light in brain tissue is quantitatively described including absorption, scattering, and reflection and refraction in Sections 2.1, 2.2, and 2.3. Numerical methods for the computation of light path and the optical forward model in fNIRS are covered in the last two sections.

2.1 Absorption

When light transmits through a medium, photons' energy is taken away by the matter of the medium, the phenomena of which is called light absorption. The probability of photon absorption per unit propagation distance, regardless of scattering, is defined as the absorption coefficient μ_a. The light absorption can be described by the following differential equation

$$\frac{\mathrm{d}I}{\mathrm{d}\ell} = -\mu_a I \tag{2.1}$$

where I and ℓ are the light intensity and transmission length respectively. The relation between the intensity before and after the transmission, named Beer-Lambert law [16, 17, 18] in Eq. 2.2, can be derived from Eq. 2.1 as follows.

$$I(\ell) = I(0)e^{-\mu_a \ell} \tag{2.2}$$

Fig. 2.1 shows the absorption and extinction coefficients [19, 20, 21] of the main chromophores in brain tissue as functions of light wavelength between 600 – 1000 nm. It can be seen from Fig. 2.1 that the hemoglobins have moderate extinction coefficients and the absorption coefficients of water and fat are small for wavelength range of the near-infrared (650 – 900 nm), where the light can transmit several centimeters in the tissue, and light with a wavelength out of this range will be heavily absorbed. This is the main reason that this interval of light is usually used for the measurements.

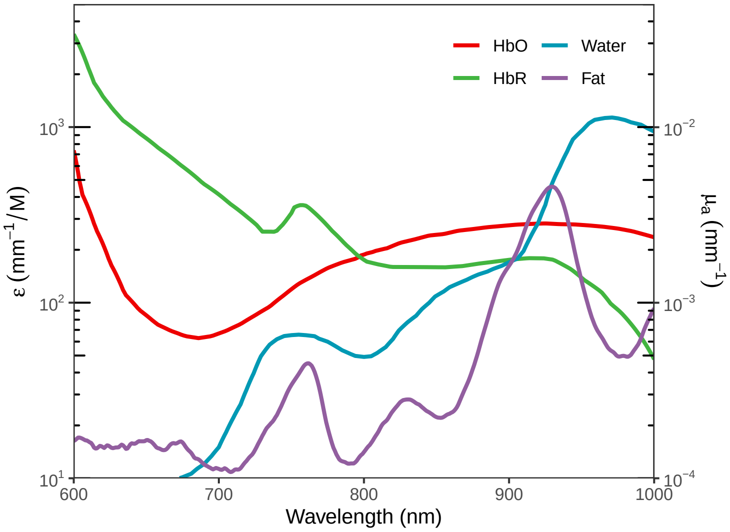

Figure 2.1: The absorption and extinction coefficients of the main chromophores in brain tissue as functions of light wavelength between 600 – 1000 nm. The extinction coefficients (for HbO and HbR) and absorption coefficients (for water and fat) are respectively annotated on the left and right axis in log scale. The chromophores are discriminated by line colors as shown in the legend.

The total absorption coefficient of the brain tissue can be calculated as follows

$$\mu_a = \sum_i \varepsilon_i c_i \tag{2.3}$$

where c_j and ε_i are the concentration and extinction coefficients of each chromophore respectively.

2.2 Scattering

The phenomena of light direction change caused by photon collision with medium matter is defined as light scattering. There are two types of scattering – elastic and inelastic scattering. Inelastic scattering is caused by the exchange of energy with the medium matter and changes light's direction. Since inelastic scattering appears in only a very small portion of photons (about 1 in every 10 million), we only discuss the elastic scattering in this section. The probability of a photon transmitting a distance ℓ before scattering occurring is described using an exponential distribution whose probability density function (PDF) is given by

$$p(\ell) = \mu_s e^{-\mu_s \ell} \tag{2.4}$$

where μ_s is the scattering coefficient. In a scattering event, the probability distribution of direction change angle θ is model by the Henyey-Greenstein function [22] in Eq. 2.5.

$$p(\theta) = \frac{1}{4\pi} \frac{1 - g^2}{(1 + g^2 - 2g\cos\theta)^{3/2}} \tag{2.5}$$

where g is a tissue-dependent anisotropy factor. Fig. 2.2 visualizes several example of the PDF with different anisotropy factor.

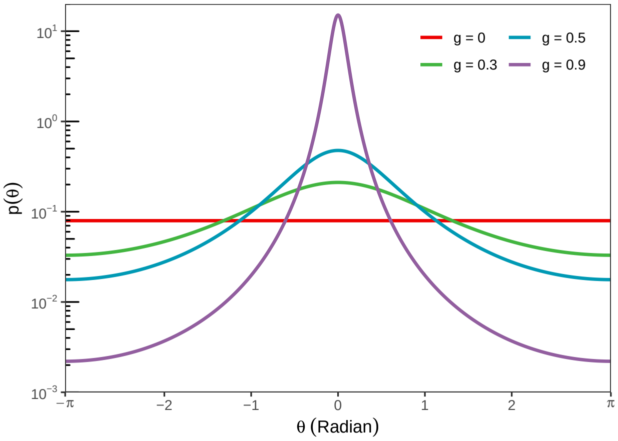

Figure 2.2: Probability density (in log scale) of scattering angle θ with different anisotropic factors (discriminated by line color).

During the light propagation where many scattering events occur, the reduced scattering coefficient μ_s' defined as

$$\mu_s' = (1 - \langle \cos\theta \rangle)\mu_s \tag{2.6}$$

where $\langle \cos\theta \rangle$ denote the mean of $\cos\theta$.

According to Mie scattering theory [23], the reduced scattering coefficient of light with wavelength λ can be modeled by a scaled linear combination of Rayleigh scattering and Mie scattering effects given by Eq. 2.7.

$$\mu_s' = \mu_0 \left[\gamma \left(\frac{\lambda}{\lambda_0} \right)^{-4} + (1-\gamma) \left(\frac{\lambda}{\lambda_0} \right)^{-\alpha} \right] \tag{2.7}$$

where μ_0 is the reduced scattering coefficient of light at the reference wavelength λ_0, α represents the power associated with Mie scattering off of large particles, and γ denote the weight of Rayleigh scattering effect that indicates the intensity of the scattering light off small particles decay proportionally to λ^4.

The average pathlength of photons increases due to scattering. The Beer-Lambert law can be corrected as follows:

$$I(\ell) = I(0) e^{-\mu_a \ell \cdot \mathrm{DPF} + G} \tag{2.8}$$

where DPF is the differential pathlength factor determined by the light scattering, and G is geometry dependent term. Eq. 2.8 is usually called modified Beer-Lambert law (MBLL).

2.3 Reflection and Refraction

Light reflection and refraction appear when traveling across the boundary of two mediums. The refractive index of a medium is defined as $n = \frac{c}{\nu}$ where $c = 2.998 \times 10^8$ m/s and ν are the light speed in a vacuum and medium respectively.

Fig. 2.3 shows an example of light reflection and refraction when light travels across the interface between two mediums with refractive indices n_i and n_o. The angle of incidence (θ_i), reflection (θ_r), and refraction (θ_o) have the following relations.

$$\begin{aligned} \theta_i &= \theta_r \\ n_i \sin\theta_i &= n_o \sin\theta_o \end{aligned} \tag{2.9}$$

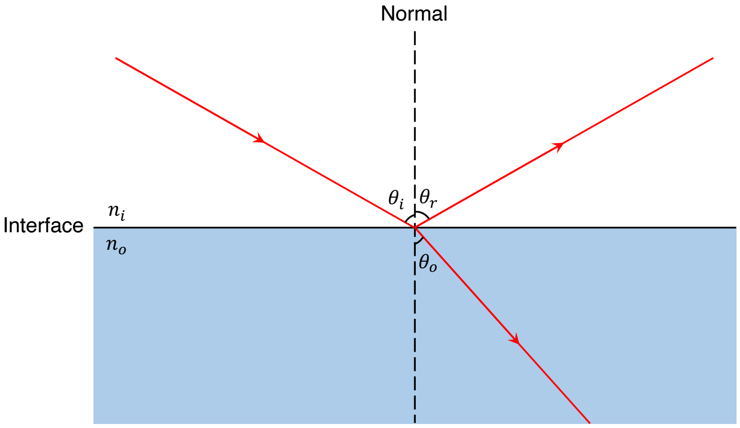

Figure 2.3: An example of light reflection and refraction when light travels across the interface between two mediums with refractive indices n_i and n_o.

The portion of photons reflected by the interface is defined as reflection coefficient R. According to Fresnel's law, R can be decomposed into s-polarized (R_s, perpendicular to the interface) and p-polarized (R_p, parallel with the interface)that are defined as:

$$\begin{aligned} R_s &= \left(\frac{n_i \cos\theta_i - n_o \cos\theta_o}{n_i \cos\theta_i + n_o \cos\theta_o}\right)^2 \\ R_p &= \left(\frac{n_i \cos\theta_o - n_o \cos\theta_i}{n_i \cos\theta_o + n_o \cos\theta_o}\right)^2 \\ R &= \frac{R_s + R_p}{2} \end{aligned} \tag{2.10}$$

2.4 Numerical Methods

The propagation path of light in homogeneous medium be calculated using radiative transfer equation (RTE) [24]. However, for heterogeneous medium like brain tissue, analytical solution for RTE does not exist. Three numerical methods, diffusion approximation, Monte Carlo and finite element, have been applied to the calculation of light propagation in heterogeneous medium.

Diffusion approximation methods approximate the light travel path in complicated medium with the analytic solution existing for simple geometries (slab, sphere, etc.) assuming the media is homogeneous. This method is fast but with limited accuracy because of approximate geometry and boundary conditions are used. However, it is still useful in some scenarios where approximate sensitivity is enough. In Chapter 5, we validate that the analysis results using the new method has a robust performance with the forward model calculated using the approximation model or other numerical methods.

Monte Carlo methods simulate photo events using random probability distributions as follows. Sample the travel distance between scattering events and polar scattering angle from the exponential distribution in Eq. 2.4 and the Henyey-Greenstein function in Eq. 2.5. Then the azimuthal angle is generated from a uniform distribution from 0 to 2π. Light absorption is also regarded as a random event in the computation. Although Monte Carlo methods are computationally expensive, they are considered as the "gold standard" when comparing to other methods as the solutions have minimum assumptions and approximations. The Monte Carlo methods have already been implemented in several previous studies [25, 26, 27, 28].

Finite element methods (FEM) [29, 30] are also popular methods to calculate light propagation. The general idea is to discretize the heterogeneous tissue into many small mesh elements that can be treated as homogeneous medium. The light propagation in the entire tissue is obtained by connecting the light absorption, scattering, reflection, and refraction in the small mesh elements. FEM are computationally efficient comparing to Monte Carlo methods.

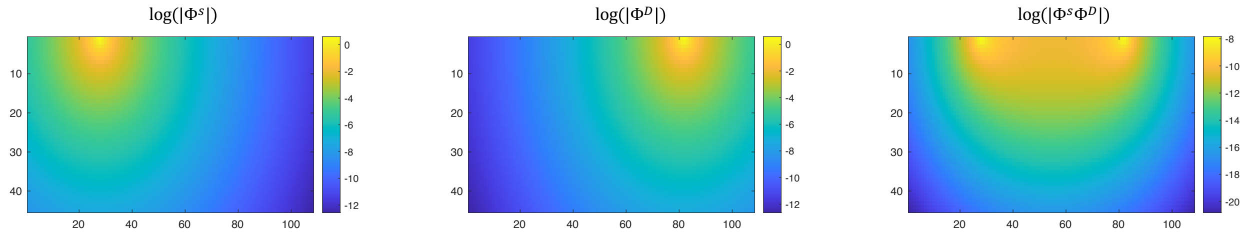

Figure 2.4: Illustration of fluence field of light source Φ^S, detector Φ^D, and joint of $\Phi^S\Phi^D$. The joint fluence field shows that the light travels via a banana-shape path in the tissue.

2.5 Optical Forward Model

With the light propagation in brain tissue calculated, we can derive the optical froward model to describe the relationship between the optical density changes recorded by light emitter-detector pairs to the hemoglobin concentration changes in the underlying tissue from MBLL, which is given by

$$\Delta\mathrm{OD}_{i,j}^{\lambda} = \mathbf{A}_{i,j}^{\lambda}\left[\varepsilon_{\mathrm{HbO}}^{\lambda}\left(\boldsymbol{\Delta}\,[\mathrm{HbO}] + \boldsymbol{\omega}_{\mathrm{HbO}}\right) + \varepsilon_{\mathrm{HbR}}^{\lambda}\left(\boldsymbol{\Delta}[\mathrm{HbR}] + \boldsymbol{\omega}_{\mathrm{HbR}}\right)\right] + \nu_{i,j}^{\lambda} \tag{2.11}$$

where $\mathbf{A}_{i,j}^{\lambda}$ is the Jacobian of the optical measurement model describes the total absorption by each voxel along the traveling path of light transmitted between the source to the detector pair (i, j). $\varepsilon_{\mathrm{HbX}}$ is the molar extinction coefficient, $\boldsymbol{\Delta}[\mathrm{HbX}]$ is the vector containing the hemoglobin changes, and $\boldsymbol{\omega}_{\mathrm{HbX}}$ is the physiological noise vector, in which HbX represents HbO or HbR for oxy- and deoxy-hemoglobin respectively. $\nu_{i,j}$ is the additive measurement space noise. Note that $\mathbf{A}_{i,j}^{\lambda}$, $\boldsymbol{\Delta}[\mathrm{HbX}]$, and $\boldsymbol{\omega}_{\mathrm{HbX}}$ are vectors with a length same as the number of voxels. For measurements between multiple channels (source-detector pair) at multiple wavelengths, the model can be written in a compact linear expression as follows

$$\mathbf{y} = \mathbf{X}\left(\boldsymbol{\beta} + \boldsymbol{\omega}\right) + \boldsymbol{\nu} \tag{2.12}$$

where $\mathbf{y}$ contains the measurements between all source-detector pairs and $\boldsymbol{\beta}$ includes oxy- and deoxy-hemoglobin concentration changes at each voxel in the brain image.

$$\mathbf{y} = \begin{bmatrix} \Delta\mathrm{OD}_{i,j}^{\lambda_1} \\ \Delta\mathrm{OD}_{i,j}^{\lambda_2} \\ \vdots \end{bmatrix} \text{ and } \boldsymbol{\beta} = \begin{bmatrix} \boldsymbol{\Delta}[\mathrm{HbO}] \\ \boldsymbol{\Delta}[\mathrm{HbR}] \end{bmatrix} \tag{2.13}$$

3.0 Background of fNIRS Data Analysis

This chapter introduces the background of fNIRS measurements in Section 3.1 and data analysis consisting of channel- and image-space analyses in Sections 3.2 and 3.3.

3.1 fNIRS Imaging

Near-infrared spectroscopy (NIRS) is a measurement technology using near-infrared because of its ability of traveling into media. A common application is the fingertip oximeter that is small device measures the oxygen saturation and heart rate via the optical density changes. Similarly, we can use NIRS to measure the brain response to specific stimulus. The brain is highly responsive to changes in blood oxygenation and blood flow. The concentrations of HbO and HbR change as the changes in blood oxygenation and blood flow, so they are significant indicators used in neuroscience. Functional NIRS (fNIRS) is a method of imaging using near-infrared spectroscopy for measuring the hemoglobin change in the cerebral cortex.

As shown in Fig. 2.1, the extinction coefficients of HbO and HbR are relatively low in the wavelength window 650 nm – 900 nm so are the absorption coefficients of other main chromophores in brain tissues. Thus, the light within this wavelength range (near-infrared) can travel into the brain cortex and the light intensity change is sensitive to the changes in HbO and HbR concentrations. At least two wavelengths are usually used for the measurement in each channel – one is more sensitive to HbO and the other one is more sensitive to HbR so that the changes in HbO and HbR concentrations can be separated in the analysis. Fig. 3.1 shows an illustration of the cap and probe used in an fNIRS experiment. The two optodes with red label are the light sources and the three with blue label are the detectors. The signal between each pair of source and detector is measured in this experiment.

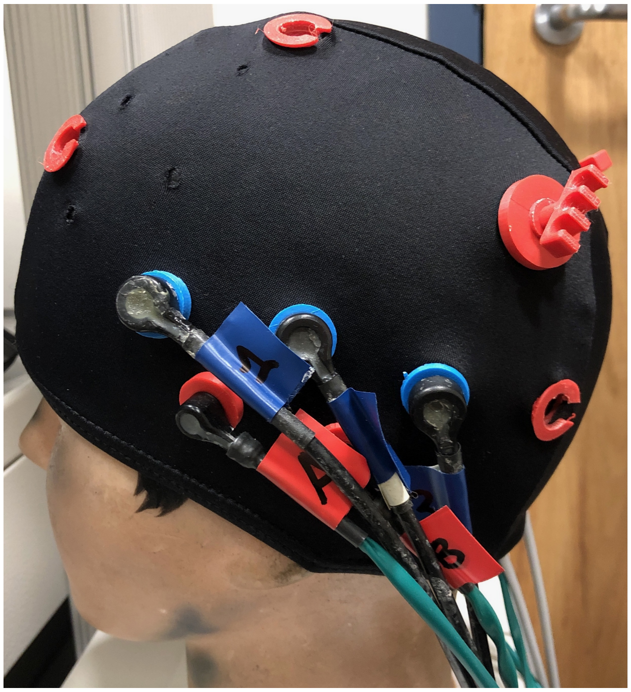

Figure 3.1: This picture shows an illustration of the cap and probe used in an fNIRS experiment. The two optodes with red label are the light sources and the three with blue label are the detectors. The signal between each pair of source and detector is measured.

3.2 Channel-space Analysis

The channel-space analyses tests the statistical significance of the association between the light intensity signal in probe channels (light emitter-detector pairs) and the expected hemodynamic response in the underlying cerebral cortex.

3.2.1 Generalized Linear Model and Basis Functions

In an evoked task, the time-series channel-space data can be modeled using a generalized linear model (GLM) as follows

$$\mathbf{y} = \mathbf{X}\boldsymbol{\beta} + \boldsymbol{\varepsilon} \tag{3.1}$$

where $\mathbf{X}$ denote the design matrix encoding the timing and duration of stimulus events, $\boldsymbol{\beta}$ contains the coefficients representing the association of the stimulus condition to each source-detector channel, and $\boldsymbol{\varepsilon}$ is the normally distributed random vector for the measurements noise that $\mathrm{E}(\boldsymbol{\varepsilon}) = \mathbf{0}$ and $\mathrm{Cov}(\boldsymbol{\varepsilon}) = \boldsymbol{\Sigma}$.

In fNIRS study, there are several popular options to create the design matrix $\mathbf{X}$. For example [31, 32],

1. Boxcar function is a lagged constant amplitude block for the duration of the stimulus event;
2. Finite impulse response (FIR) basis function is an unconstrained deconvolution and estimation of the full hemodynamic response using different number and width of bins;
3. Gamma hemodynamic response function (HRF) defined by $\frac{\beta^{\alpha}}{\Gamma(\alpha)} t^{\alpha-1} e^{\beta t}$ where β is the dispersion constant and α is the peak time;
4. Canonical HRF defined by $\frac{\beta_1^{\alpha_1}}{\Gamma(\alpha_1)} t^{\alpha_1-1} e^{\beta_1 t} - c \cdot \frac{\beta_2^{\alpha_2}}{\Gamma(\alpha_2)} t^{\alpha_2-1} e^{\beta_2 t}$ where where β_1 and β_2 are the dispersion constant of the response and undershoot, α_1 and α_2 are the peak and undershoot time, and c is the ratio between the height of the main response and undershoot.

Fig. 3.2 illustrates examples of these HRFs for the stimulus events drawn on the top row. With an appropriate basis function selected, the GLM in Eq. 3.1 can be solved using generalized least squared (GLS) as Eq. 3.2.

$$\begin{aligned} \hat{\boldsymbol{\beta}} &= \left(\mathbf{X}^{\mathrm{T}} \boldsymbol{\Sigma}^{-1} \mathbf{X}\right)^{-1} \mathbf{X}^{\mathrm{T}} \boldsymbol{\Sigma}^{-1} \mathbf{y} \\ \mathrm{Cov}(\hat{\boldsymbol{\beta}}) &= \left(\mathbf{X}^{\mathrm{T}} \boldsymbol{\Sigma}^{-1} \mathbf{X}\right)^{-1} \end{aligned} \tag{3.2}$$

Although the equations are straightforward for calculation, they cannot be directly applied to fNIRS data since the normality,independence, and homoscedasticity assumptions for measurement noise are violated. The previous paper [33] summarizes the properties of the measurement noises in fNIRS including:

- The noise within a channel is auto-correlated due to strong but slower physiological signals such as cardiac, respiratory, and blood pressure changes;

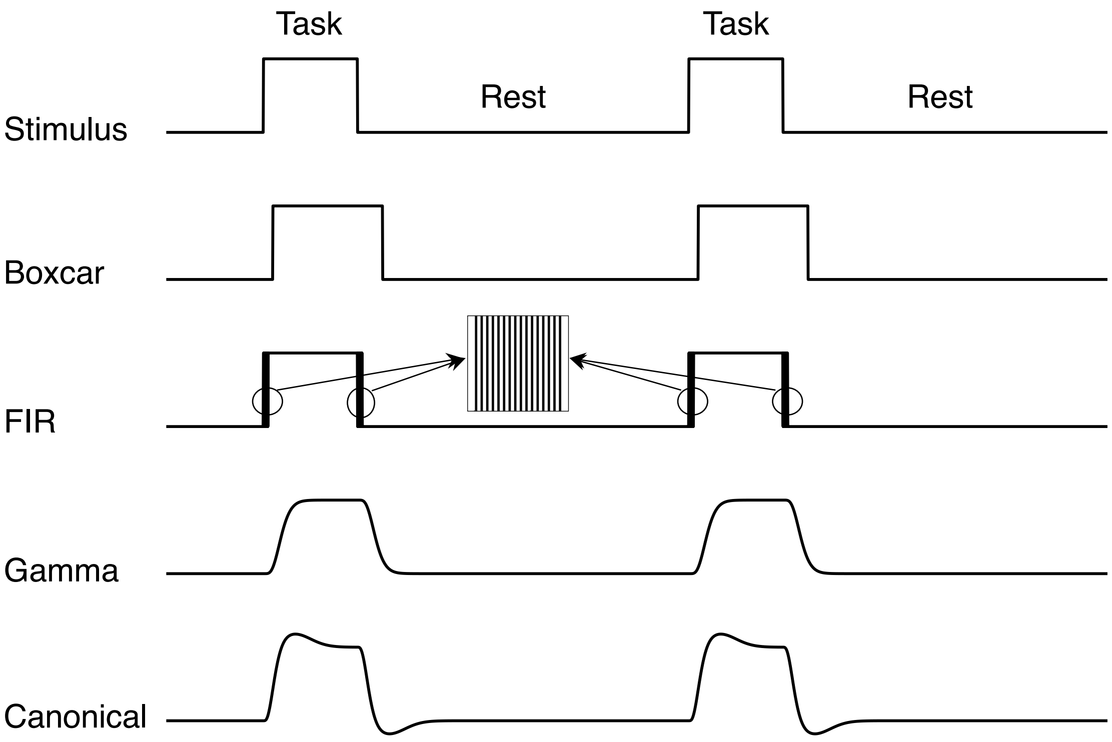

Figure 3.2: Example of commonly used HRFs for the stimulus events shown on the first row

- The noise is not independent across channels due to superficial physiological signals and the correlation between HbO and HbR changes;
- The noise shows a heteroscedastic pattern mainly because the existence of motion artifacts during tasks, which makes the noise variance nonuniform;
- The noise may be nonergodic and nonstationary in physical movement tasks that will cause changes in noise properties during tasks from baseline periods.

These problems have been address through different solutions. Preprocessing, including prewhitening and precoloring, is usually adapted to fNIRS data for noise correlation correction before the GLM analysis. For the heteroscedasticity and nonstationarity of fNIRS data, Autoregressive Iterative Reweighted Least Squares (AR-IRLS) algorithm [34] was proposed to estimate the noise covariance matrix by down-weighting outliers in the noise. When the estimates of $\boldsymbol{\beta}$ and $\mathrm{Cov}(\boldsymbol{\beta})$ are obtained, t-statistics can be used to test linear combinations of the $\boldsymbol{\beta}$ by defining the contrast vector $\mathbf{c}$ as follows.

$$t = \frac{\mathbf{c}^{\mathrm{T}}\boldsymbol{\beta}}{\sqrt{\mathbf{c}^{\mathrm{T}}\mathrm{Cov}(\boldsymbol{\beta})\mathbf{c}}} \tag{3.3}$$

For example, $\mathbf{c} = [1, 1, 0 \dots]^{\mathrm{T}}$ and $\mathbf{c} = [1, -1, 0 \dots]^{\mathrm{T}}$ can be used to test the significance of the sum of and difference between the first and second regressors, respectively. In Chapter 5, a novel tapered contrast vector will be introduced that can improve the statistical performance.

3.2.2 Group-level Analysis

Once the GLM estimates for the fNIRS dataset of each subject are obtained, a mixed-effect model can be used to test effects of group-level factors on the hemodynamic activity. The group-level mixed-effect model can be written as [31]

$$\boldsymbol{\beta} = \mathbf{A}\boldsymbol{\Gamma} + \mathbf{B}\boldsymbol{\Theta} + \boldsymbol{\nu} \tag{3.4}$$

where $\boldsymbol{\beta}$ is the vector containing the subject-level GLM estimates of all subjects, $\boldsymbol{\Gamma}$ and $\boldsymbol{\Theta}$ are the two vectors respectively consisting of the group-level fixed-effects and subject-level random effects to be estimated, and $\mathbf{A}$ and $\mathbf{B}$ are the design matrices for fixed- and random-effects, respectively.

Eq. 3.5 shows an example that there are three task conditions (L, M, H) and N subjects in the experiment. $\beta_{i,X}$ denote the subject-level estimate of subject i on condition X. If some demographic information is collected, such as age, gender, etc., the effects of these factors can also be estimated. The matrices $\mathbf{A}$ and $\boldsymbol{\Gamma}$ in model 3.5 shows how to perform the analysis on the main effects of task condition (Γ_L, Γ_M, and Γ_H) and the the interaction effects of condition and subject's age ($\Gamma_{L\times\mathrm{AGE}}$, $\Gamma_{M\times\mathrm{AGE}}$, and $\Gamma_{H\times\mathrm{AGE}}$). The vector $\boldsymbol{\Theta}$ includes the subject-level random-effects for the N subjects (subject as a random-effect in this example). This model is flexible to estimate the effects of various factors as long as design matrices are appropriately used. This model can also be solved using GLM approaches with interposing

$\mathrm{Cov}(\hat{\boldsymbol{\beta}})$ from the subject-level analysis into the group-level analysis as the noise covariance matrix.

$$
\begin{bmatrix} \beta_{1,L} \\ \beta_{1,M} \\ \beta_{1,H} \\ \vdots \\ \beta_{N,L} \\ \beta_{N,M} \\ \beta_{N,H} \end{bmatrix}
=
\begin{bmatrix}
1 & & & \mathrm{age}_1 & & \\
& 1 & & & \mathrm{age}_1 & \\
& & 1 & & & \mathrm{age}_1 \\
& \ddots & & & \ddots & \\
1 & & & \mathrm{age}_N & & \\
& 1 & & & \mathrm{age}_N & \\
& & 1 & & & \mathrm{age}_N
\end{bmatrix}
\begin{bmatrix} \Gamma_L \\ \Gamma_M \\ \Gamma_H \\ \Gamma_{L\times \mathrm{AGE}} \\ \Gamma_{M\times \mathrm{AGE}} \\ \Gamma_{H\times \mathrm{AGE}} \end{bmatrix}
+
\begin{bmatrix}
1 & & \\
1 & & \\
1 & & \\
& \ddots & \\
& & 1 \\
& & 1 \\
& & 1
\end{bmatrix}
\begin{bmatrix} \Theta_1 \\ \vdots \\ \Theta_N \end{bmatrix}
+ \boldsymbol{\nu}
\tag{3.5}
$$

As mentioned in Chapter 1, a major problem of group-level analysis is the variations in anatomy and probe registration across the subjects in a group, which can cause notable difference in the channel-space signals even if the underlying brain activity is the same. A previous study [35] investigated the effects of anatomical variations in group-level analysis. In this study, 90 segmented MRI volumes from children ages 5 to 11 years are used to calculate the DPF, and tables of DPF, sensitivity, and suggested nearest location of each Brodmann area are provided. It can be summarized from the results that there is about a 13% to 26% spatial difference going across the regions from the frontal or lateral to superior of the head and about 13% to 18% difference between genders. These conclusions show the significance of the analysis method addressing the subject-level variation in the group-level analysis, which is the main goal of the study in Chapter 5.

3.3 fNIRS Image Reconstruction Methods

fNIRS image reconstruction methods estimate the HbO and HbR concentrations changes at each voxel in the cerebral cortex by solving the model defined in Eq. 2.12. However, Eq. 2.12 is an ill-posed and under-determined problem since there are thousands of hemoglobin changes to be estimated but only tens of measurements usually available. Current existing image reconstruction methods involve regularizations or penalties to reduce the dimensionality of the problem.

3.3.1 Restricted Maximum Likelihood (ReML)

A previous study [36] solves the fNIRS image reconstruction model via the following optimization.

$$\hat{\boldsymbol{\beta}} = \underset{\{\boldsymbol{\beta},\mathbf{C_N},\mathbf{C_P}\}}{\arg\max} -\frac{1}{2}\|\mathbf{y}-\mathbf{X}\boldsymbol{\beta}\|^2_{\mathbf{C_N}} - \frac{1}{2}\|\boldsymbol{\beta}-\boldsymbol{\beta_0}\|^2_{\mathbf{C_P}} - \frac{1}{2}\log|\mathbf{C_N}| - \frac{1}{2}\log|\mathbf{C_P}| \tag{3.6}$$

where $\boldsymbol{\beta_0}$ is a prior estimate of $\boldsymbol{\beta}$, and $\mathbf{C_N}$ and $\mathbf{C_P}$ are the covariance matrices for the error term and $\boldsymbol{\beta}$ respectively. In this study, these two matrices are parameterized based on the prior information of wavelengths and hemoglobin types. Expectation-maximization (EM) algorithm is applied to solve the problem – Gaussian-Markov equation is used to calculate

$$\hat{\boldsymbol{\beta}} = \boldsymbol{\beta_0} + \left(\mathbf{X}^{\mathrm{T}}\mathbf{C_N^{-1}}\mathbf{X} + \mathbf{C_P^{-1}}\right)^{-1}\mathbf{X}^{\mathrm{T}}\mathbf{C_N^{-1}}\left(\mathbf{y}-\mathbf{X}\boldsymbol{\beta_0}\right) \tag{3.7}$$

given specific $\mathbf{C_N}$ and $\mathbf{C_P}$ in the expectation step while $\mathbf{C_N}$ and $\mathbf{C_P}$ are optimized by maximizing the likelihood function in the maximization step.

3.3.2 Maximum Entropy on the Mean

The method of maximum entropy on the mean (MEM) [37, 38, 39] is a framework of fNIRS image reconstruction based on the information theory that prior information is minimized when a distribution with maximized entropy is chosen. Thus, the model is solved by maximizing the Kullback's μ-entropy defined as follows

$$\mathcal{S}_\mu(\mathrm{d}p) = -\int \log\frac{\mathrm{d}p}{\mathrm{d}\mu}\,\mathrm{d}p = -\int f(\boldsymbol{\beta})\log f(\boldsymbol{\beta})\,\mathrm{d}\mu(\boldsymbol{\beta}) \tag{3.8}$$

where f is the μ-density and $\mathrm{d}\mu(\boldsymbol{\beta})$ is a product of mixtures of a Dirac and multivariate normal distribution. In the optimization process, the mixture fraction, mean and covariance matrix of the multivariate normal distribution are varied to maximize the μ-entropy. Finally, $\boldsymbol{\beta}$ is estimated from the optimal parameters of $\mathrm{d}\mu(\boldsymbol{\beta})$.

3.3.3 Depth Compensation

Depth compensation [40] is another approach of fNIRS image reconstruction based on regularization. Unlike ReML involving optimization for covariance matrices, this method simply solve the estimates from the common Tikhonov regularization as follows.

$$\hat{\boldsymbol{\beta}} = \left(\mathbf{X}^{\mathrm{T}}\mathbf{X} + \lambda \mathbf{I}\right)^{-1} \mathbf{X}^{\mathrm{T}}\mathbf{y} \tag{3.9}$$

where λ is the tuning parameter. Before solving the equation, $\mathbf{X}$ is transformed as $\mathbf{X} := \mathbf{XM}$. Here $\mathbf{M}$ is the depth compensation matrix containing the maximum singular value of $\mathbf{X}$ in each layer of voxels with a same depth on the diagonal as follows.

$$\mathbf{M} = \begin{bmatrix} \theta\left(\mathbf{X}_n\right) & & & \\ & \ddots & & \\ & & \theta\left(\mathbf{X}_2\right) & \\ & & & \theta\left(\mathbf{X}_1\right) \end{bmatrix}^{\gamma} \tag{3.10}$$

where the subscript of $\mathbf{X}$ denote the elements for voxels at the layer (n layers in total), and γ is the parameter to adjust the weight of depth compensation. The depth compensation transformation reweights the sensitivity matrix by layers and consequently smooths the estimates. This method was extended with ℓ_1 regularization in a later study [41].

4.0 Background of Statistics

In this chapter, we will provide an overview of the main statistical tools used in this dissertation. Section 4.1 introduces basics of ROC analysis, and Section 4.2 describes the general idea and framework of Bayesian hierarchical modeling with derivations and examples.

4.1 Receiver Operating Characteristics

ROC curve is a tool to assess the performance of a binary classifier that is widely used in medicine, radiology, biology, psychology, image detection, machine learning, etc. and also frequently utilized for the evaluation of the newly proposed methods in this dissertation. In this section, background knowledge of ROC analysis is covered including different paradigms and the statistical testing methods.

4.1.1 Different ROC-based Evaluation Paradigms

Let us explain the definitions using an example where there are in total N cases to be classified. Among these cases, N_0 and N_1 cases are target-free (negative) and target-containing (positive) in truth. A binary classifier (can be a statistical model, machine, person, etc.) is asked to label case each as positive or negative and give a rating of being positive. True positives (TP) and true negatives (TN) are defined as the positive/negative cases that are correctly labeled as positive/negative, and similarly, false positive (FP) and false negatives (FN) are the positive/negative cases that are incorrectly labeled as negative/positive. Sensitivity and specificity are defined as the fraction of TPs and TNs. The false positive rate (FPR) and true positive rate (TPR) can be calculated as follows [15, 42].

$$\begin{aligned} FPR &= \frac{N_{FP}}{N_0} = 1 - \text{specificity} \\ TPR &= \frac{N_{TP}}{N_1} = \text{sensitivity} \end{aligned} \tag{4.1}$$

where N_{FP} and N_{TP} are the number of FPs and TPs respectively. For different rating thresholds, the classifier will give different FPR and TPR pairs. The ROC curve for this classifier is defined as the curve connecting the points (FPR, TPR) by varying the rating threshold from $-\infty$ to $+\infty$. The area under the curve (AUC) is a widely used figure of merit for the assessment of the classification performance of the classifier. The statistical meaning of AUC is the probability that the classifier assigns a higher rating to a random chosen positive case than a negative case. Thus, larger AUC implies a better classification performance. In the worst case, the classifier randomly labels cases, which will result in an $AUC = 0.5$ (a classifier with an AUC smaller than 0.5 is better with the classification results inverted). On the contrary, the AUC in the perfect case is 1, in which the classifier correctly labels all the cases. Fig. 4.1 shows example ROC curves with typical AUC values. Note that ROC curves with same AUC can have different shapes. The curves in the plot are only examples.

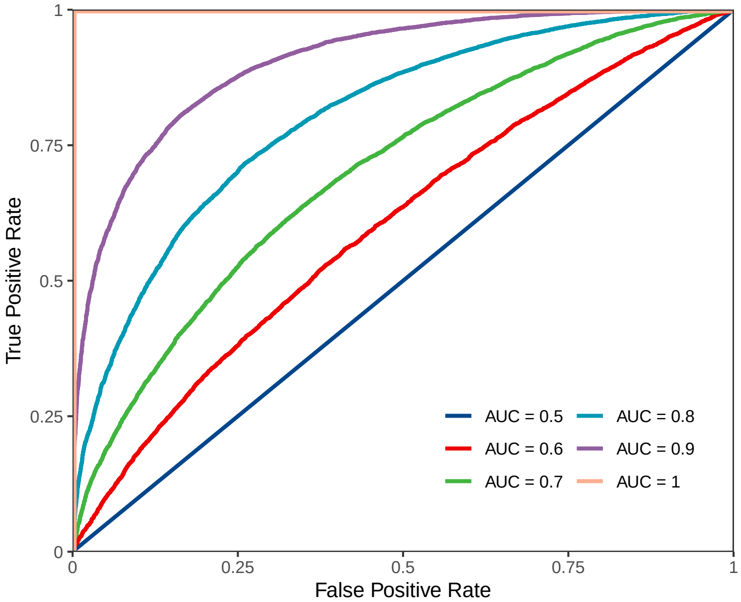

Figure 4.1: Example of ROC curves with typical AUC values. Line color is used for different AUC values indicated by the legend. A Larger AUC means a better classification performance. AUC = 0.5 is the worst while AUC = 1 is for a perfect classifier. The remaining curves are for classifiers with intermediate performances.

In some image classification tasks, each case may include multiple predefined regions of interest (ROI) due to clustering. Classifiers are required to rate each ROI independently. ROI-ROC [43, 44] is an extension of ROC to handle the classification results of this type of tasks where FPR and TPR are calculated in a similar way as in Eq. 4.1. The only difference is that N_0, N_1, N_{FP}, and N_{TP} are the number of negatives, positives, FPs, and TPs in the ROI level. With these extended definitions, the ROI-ROC curve and AUC for a classifier can be calculated.

Another more complicated but practical situation is that a positive case may contain multiple targets at various un-predefinable locations, e.g., there may be multiple lesions in a CT image of a patient but the locations of the lesions cannot be predefined by ROIs due to the anatomical difference across patients. In this type of tasks, named free-response tasks, classifiers are required to mark the lesion localization on the image and give each mark a rating representing the confidence of being positive (a $-\infty$ rating is automatically assigned to unmarked lesion loclizations). The evaluation is extended to free-response ROC (FROC) [45, 46, 47]. Similarly, the FPR and TPR in the lesion level, named non-lesion localization fraction (NLF) and lesion localization fraction (LLF), can be calculated with the lesion localization numbers. The FROC curve is defined as LLF vs. NLF [45]. However, NLFs of different classifiers are not comparable since they can provide different number of non-lesion localizations, so the FROC AUC is unmeaningful. One solution is to derive the inferred ROC (iROC) curve that can be obtained by calculating FPR and TPR using the highest NL and LL rating as the FP and TP rating of the entire image. Another approach is the alternative FROC (AROC) [45, 48, 49] curve defined by LLF vs. FPR, in which FPR is calculated in the same way of iROC. These two approaches have their own problems that iROC ignores multiple lesion localization information and the cases containing more lesions make more contribution than those containing less lesions to AFROC AUC. Weighted AFROC (wAFROC) [50] was proposed to address this problem, in which weighted LLF (wLLF) is calculated by assigning each lesion a weight. The weights of lesions in a same case is summed up to one. Thus, the contributions of positive cases containing different number of lesions are equal. The AUC of iROC, AFROC, and wAFROC curves are all commonly used as the figure of merit for classifiers in free-response tasks with different advantages.

In this dissertation, ROC and ROI-ROC are the main paradigms used for the evaluation of the new channel-space analysis model (Chapter 5) and image reconstruction method (Chapter 6) respectively.

4.1.2 Non-parametric Test for the Difference Between AUCs

Once the AUCs of classifiers are calculated, using any paradigm described in Section 4.1.1, the statistical comparison between AUCs is usually necessary. To test if there is a significant difference between two AUCs, the z-statistic is defined by

$$z = \frac{|\mathrm{AUC}_1 - \mathrm{AUC}_2|}{\mathrm{Se}(\mathrm{AUC}_1 - \mathrm{AUC}_2)} \tag{4.2}$$

where Se() is the standard error. Therefore, the key is to calculate the standard error of AUC. There existing three methods to estimate the standard error of AUC, which are Bootstrap, Jackknife, and DeLong's [51]. Fig. 4.2 is the schematic diagram of Jackknife and Bootstrap resampling, from which we can see that Jackknife resamples the original sample by taking every case out one by one and Bootstrap generates new same-size samples by randomly selecting cases with replacement. We can calculate the AUC with every new sample, then the variance of original sample AUC can be determined by calculating the variance of the bunch of new AUCs. Delong et al. [51] provided a method to estimate the variance-covariance matrix of AUCs using the method of structural components, which is equivalent to Jackknife but conceptually simpler. These three methods provides equivalent statistical inference.

A z-test can be performed to test the significance between two AUCs using the z-statistic calculated by Eq. 4.2. With the methods of estimating standard error of AUC, the effects of different factors, e.g., multiple classifiers, imaging modalities, can be tested via ANOVA using t- and/or F-test. Two main frameworks, Dorfman-Berbaum-Metz (DBM) [52, 53, 54] and Obuchowski-Rockette (OR) [53, 55] have been built for the test with different model assumptions. Hillis et al. also made significant contributions to these frameworks including correction of model degrees of freedoms [53], demonstration of the equivalency between the two models [56], statistical power estimation [57, 58], sample size calculation [57, 58], and model extensions to different conditions [59, 60, 61, 62].

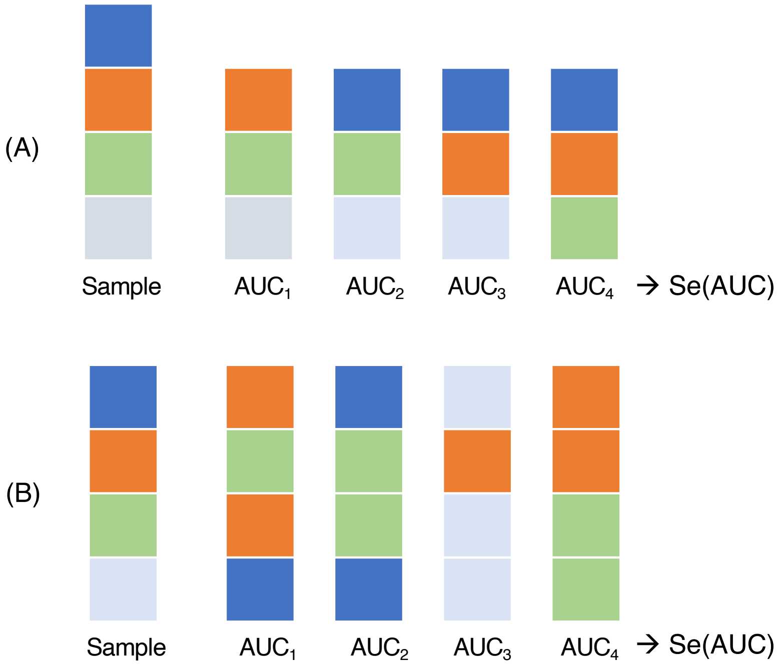

Figure 4.2: The schematic diagram of Jackknife (A) and Bootstrap (B) resampling. Each colored square represents a case. The most left column is the original data and the remaining columns are the newly generated samples. Jackknife resamples the original sample by taking every case out one by one and Bootstrap generates new same-size samples by randomly selecting cases with replacement. With each new sample set, an AUC can be calculated. The sample standard error of the AUCs calculated using the new sample sets is the standard error estimate of the original AUC.

In this dissertation, the z-test described in Eq. 4.2 is used to test the performance difference between analysis methods utilizing Delong's method for standard error estimation.

4.1.3 Parametric Models for ROC Curves

Besides the non-parametric methods for AUC testing, there are also parametric methods to model ROC curves with assumptions. The parameterizations of several commonly used models are briefly described in this section.

1. **Binormal model** [63, 64, 65, 47] assumes the ratings of negative and positive cases follows two normal distributions $\mathcal{N}(0,1)$ and $\mathcal{N}(\mu,\sigma^2)$ respectively. The FPR and TPR at a rating threshold ζ can be calculated as follows

$$\begin{aligned} FPR(\zeta) &= 1 - \Phi(\zeta) = \Phi(-\zeta) \\ TPR(\zeta) &= \Phi\left(\frac{\mu-\zeta}{\sigma}\right) \end{aligned} \tag{4.3}$$

   where $\Phi()$ denotes the cumulative distribution function (CDF) of the standard normal distribution. The AUC of the parametric curve can be calculated as $A = \int_0^1 TPR\,\mathrm{d}FPR = \Phi\left(\frac{\mu}{\sqrt{1+\sigma^2}}\right)$

2. **Contaminated binormal model (CBM)** [66, 67, 68] assumes the same distribution for the negative ratings but a mixture of $\mathcal{N}(0,1)$ and $\mathcal{N}(\mu,1)$ for ratings of positive ratings. The TPR can be calculates as follows

$$TPF(\zeta) = (1-\alpha)(1-\Phi(\zeta)) + \alpha(1-\Phi(\zeta-\mu)) = (1-\alpha)\Phi(-\zeta) + \alpha\Phi(\mu-\zeta) \tag{4.4}$$

   where α is the mixture fraction of $\mathcal{N}(0,1)$. The AUC of CBM can be derived as $A = \int_0^1 TPR\,\mathrm{d}FPR = 0.5(1-\alpha) + \Phi\left(\frac{\mu}{\sqrt{2}}\right)$

These two methods have been extended to bivariate models named CORROC2 [69, 70, 71] and CORCBM [72], which models the ratings on the same set of cases from two classifiers using bivariate normal distributions. Besides the individual parameters in the univariate models, the bivariate models also include correlations between the ratings of two classifiers. With the given classification results of a classifier, the model parameters can be estimated via MLE. The AUC and its uncertainty can be derived from the model parameter estimates, and a statistical conclusion on the difference between AUCs can then be drawn.

4.2 Bayesian Hierarchical Modeling

Unlike commonly used optimization method in frequentist's framework, such as maximum likelihood estimation (MLE), parameters are treated as random variables instead of fixed values and their posterior probabilities are maximized in the Bayesian framework. Let $\mathbf{y}$ and $\boldsymbol{\theta}$ denote the observation and parameter vectors. In Bayesian models, we estimate $\boldsymbol{\theta}$ by maximizing the posterior probability as follows [73].

$$\hat{\boldsymbol{\theta}} = \arg\max_{\boldsymbol{\theta}} \left[p(\boldsymbol{\theta} \mid \mathbf{y}) \right] \tag{4.5}$$

Using Bayes' theorem, the optimization can be rewritten as [73]

$$\hat{\boldsymbol{\theta}} = \arg\max_{\boldsymbol{\theta}} \left[p(\boldsymbol{\theta} \mid \mathbf{y}) \right] = \arg\max_{\boldsymbol{\theta}} \frac{p(\mathbf{y} \mid \boldsymbol{\theta}) p(\boldsymbol{\theta})}{p(\mathbf{y})} = \arg\max_{\boldsymbol{\theta}} \left[p(\mathbf{y} \mid \boldsymbol{\theta}) p(\boldsymbol{\theta}) \right] \tag{4.6}$$

where the denominator $p(\mathbf{y})$ is discarded because its value remains constant in the optimization. The two components in the objective function – $p(\mathbf{y} \mid \boldsymbol{\theta})$ and $p(\boldsymbol{\theta})$ – are the likelihood function and prior probability respectively. $p(\mathbf{y} \mid \boldsymbol{\theta})$ can be straightforwardly obtained based on the model assumptions, e.g., normally distributed errors in linear regression models. The calculation of the prior probability is the key step of Bayesian Modeling. As mentioned above, $\boldsymbol{\theta}$ is treated as a random variable following a prior probability distribution in Bayesian modeling, which usually defined by some hyperparameters. The hyperparameter $\boldsymbol{\phi}$ can be treated as either some fixed values or a random variable following a hyperprior distribution. Similarly, the hyperprior distribution also includes hyperparameters, and the modeling can continue infinitely. For simplicity without losing generality, a three-layer Bayesian hierarchical model is used as an illustration in the remaining of this section, which can be formulated as follows:

- Layer-I: $\mathbf{y} \mid \boldsymbol{\theta}, \boldsymbol{\phi} \sim p(\mathbf{y} \mid \boldsymbol{\theta}, \boldsymbol{\phi})$
- Layer-II: $\boldsymbol{\theta} \mid \boldsymbol{\phi} \sim p(\boldsymbol{\theta} \mid \boldsymbol{\phi})$
- Layer-III: $\boldsymbol{\phi} \sim p(\boldsymbol{\phi})$

The posterior probability distribution of the parameter of interest $\boldsymbol{\theta}$ can be calculated as follows:

$$p(\boldsymbol{\theta} \mid \mathbf{y}) = \int p(\boldsymbol{\theta}, \boldsymbol{\phi} \mid \mathbf{y}) \, \mathrm{d}\boldsymbol{\phi} \propto \int p(\mathbf{y} \mid \boldsymbol{\theta}) p(\boldsymbol{\theta} \mid \boldsymbol{\phi}) p(\boldsymbol{\phi}) \, \mathrm{d}\boldsymbol{\phi} \tag{4.7}$$

In an ideal case, the analytical solution of above integration can be obtained and is the PDF of a known probability distribution. Then we can use the mean, median, or mode of the distribution as the estimate of $\boldsymbol{\theta}$. Unfortunately, this is not the case for most practical problems. In these cases, we usually generate random samples via Markov chain Monte Carlo (MCMC) using full conditional distributions of the parameters denoted $p(\boldsymbol{\theta} \mid \text{rest})$, which can be easily obtained from the full joint PDF. Once the full conditionals of all parameters are derived, we can sample each parameter using Gibbs sampler if the full conditional is a known distribution or Metropolis-Hasting sampler otherwise. Let $\boldsymbol{\Theta}$ denote the vector containing all parameters and hyperparameters of the hierarchical model (assume there are n parameters in total and Θ_i denote the i-th element in $\boldsymbol{\Theta}$). The MCMC sampling process can be briefly described as follows [73]:

- Set initial value for each element of $\boldsymbol{\Theta}$ denoted as $\boldsymbol{\Theta}^{(0)}$
- For the t-th sampling iteration:
  1. Generate $\Theta_1^{(t)}$ from its full conditional using samples of the rest parameters from iteration $t-1$: $\Theta_1^{(t)} \sim p(\Theta_1 \mid \Theta_2^{(t-1)}, \Theta_3^{(t-1)} \ldots \Theta_n^{(t-1)})$
  2. Generate $\Theta_2^{(t)}$ from its full conditional using $\Theta_1^{(t)}$ and samples of the rest parameters from iteration $t-1$: $\Theta_2^{(t)} \sim p(\Theta_2 \mid \Theta_1^{(t)}, \Theta_3^{(t-1)} \ldots \Theta_n^{(t-1)})$
  3. $\vdots$
  4. Generate $\Theta_n^{(t)}$ from its full conditional using samples of the rest parameters from iteration t: $\Theta_n^{(t)} \sim p(\Theta_n \mid \Theta_1^{(t)}, \Theta_2^{(t)} \ldots \Theta_{n-1}^{(t)})$
  5. To next iteration
- Stop sampling when the maximum number of iterations is reached. Drop off the beginning part of the Markov chain as burn-in iterations, and use the remaining samples of the parameters of interest as the estimations.

The estimate of a Bayesian model depends on the selection of prior distributions and hyperparameters. For well-determined problems with enough observations, the estimates are not different too much if weakly informative priors (with large variance) are used. However, for ill-posed under-determined problems, different prior distributions and hyperparameters can result in very different results, in which case cross-validation is required to find appropriate prior distributions and hyperparameters.

Although solving Bayesian models is not straightforward and the sampling process is computationally costly, Bayesian modeling becomes more and more popular because of its good interpretability and the ability of incorporating prior information of the data. In this dissertation, Bayesian hierarchical modeling is the main approach for solving the fNIRS image reconstruction problem by incorporating useful prior information into the model described in Chapter 6.

5.0 Using Anatomically Defined Regions-of-interest to Adjust for Head-size and Probe Alignment in fNIRS

As mentioned in previous chapters, "blind-spots" effect is a main challenge in fNIRS. In this chapter, we will fully describe a tapered contrast vector method for fNIRS data analysis in the channel-space including the model and simulation results. This work has been published in Neurophotonics [74] and available online at https://doi.org/10.1117/1.NPh.7.3.035008.

5.1 Abstract

Significance: Functional near-infrared spectroscopy (fNIRS) uses surface-placed light sources and detectors to record underlying changes in the brain due to fluctuations in hemoglobin levels and oxygenation. Since these measurements are recorded from the surface of the scalp, the mapping from underlying regions-of-interest (ROIs) in the brain space to the fNIRS channel space measurements depends on the registration of the sensors, the anatomy of the head/brain, and the sensitivity of these diffuse measurements through the tissue. However, small displacements in the probe position can change the distribution of recorded brain activity across the fNIRS measurements.

Aim: We propose a novel approach using either individual or atlas-based brain-space anatomical information to define ROI-based statistical hypotheses to test the null-involvement of specific regions, which allows us to test the analogous ROI across subjects while adjusting for fNIRS probe placement and sensitivity differences due to head size variations without a localizer task.

Approach: We use the optical forward model to project the underlying brain-space ROI into a tapered contrast vector, which defines the relative weighting of the fNIRS channels contributing to the ROI and allows us to test the null hypothesis of no brain activity in this region during a functional task. In this paper, we demonstrate this method through simulation and compare the sensitivity-specificity of this approach to other conventional methods'.

Results: We examine the performance of this method in the scenario where head size and probe registration are both an accurately known parameter and where this is subject to unknown experimental errors. This method is compared with the performance of the conventional method using 364 different simulation parameter combinations.

Conclusion: The proposed method is always recommended in ROI-based analysis, since it significantly improves the analysis performance without a localizer task, wherever the fNIRS probe registration is known or unknown.

5.2 Introduction

Functional near-infrared spectroscopy (fNIRS) is a non-invasive neuroimaging technique that uses low levels of red to near-infrared light to measure changes in the optical absorption due to hemoglobin in the brain. Typically, light is sent into the tissue from source positions on the scalp. This light diffuses through the tissue and a small fraction of the light is detected at a discrete set of optical detector positions placed several centimeters from the originating source position. These channel-space measurements are sensitive to changes in the optical properties of the tissue along this diffuse volume between the light source and detector. During an evoked functional task, the changes in blood flow and oxygenation in the brain result in fluctuations in optical absorption due to hemoglobin in this local region and this gives rise to changes in the fNIRS measurements in the source-detector pairs (channels) crossing this region. Using a grid of these optical source and detector positions embedded in a head probe, functional brain activity can be recorded from regions of the surface of the brain's cortex. Over the last three decades, fNIRS has been used in a variety of different brain imaging studies and populations (reviewed in [3, 4, 5, 6]). In particular, the ability to noninvasively record brain activity without participant immobilization or a specialized dedicated scanner environment (cf. magnetic resonance imaging; MRI) make this technique well suited for studies in pediatric populations (reviewed in [3, 7, 8, 9]).

A challenge of fNIRS measurements, however, is group-level registration of these signal changes from these sparse surface-based measurements. Small displacements in the probe position relative to the underlying brain region can change the distribution of recorded brain activity across the fNIRS measurements. This is particularly problematic in cross-sectional or longitudinal studies of child development, where the head-size varies between sessions. Moreover, these measurements are also sensitive to inter-subject differences in head anatomy, such as skull thickness and depth of the brain relative to the skin's surface. Thus, this uncertainty increases variance across measurement sessions and reduces statistical effects sizes. This also makes studies of brain activation changes with child age and development difficult.

An alternative approach to this would be to use an individual's response to a "localizer" functional task to define consistent underlying brain regions across participants. While, this data-driven approach makes less assumptions than atlas-based models (as will be detailed in this work) to define regions-of-interest, this method requires the ability to robustly measure a specific localizer task response for a given brain-region in each subject. This is not always possible since not all brain regions can be specifically and uniquely defined by localizer tasks, which may involve multiple regions of the brain. In addition, single-subject statistics are often not reliable enough to define individualized regions for many tasks or subject populations. Thus, while the use of a localizer task is recommended when possible, more generalizable solutions are also needed.

Methods for the spatial registration of the fNIRS head cap and measurement channels with respect to the brain have been described in previous work [10, 11, 12, 13]. Although not always possible or practical, fNIRS investigators often record this information with either a three-dimensional camera and registration system (e.g. [14]) or simply by using a tape measure to record head-size and potentially the location of the fNIRS sensors relative to the international 10-20 system. Although this registration information is recorded as part of fNIRS experimental best-practices by many labs, there has been very little development of quantitative methods to actually quantitatively use this information within fNIRS analysis.

In this current work, we propose a new approach to quantitatively incorporate head-size, probe registration, and/or individual anatomical information to define regions-of-interest

(ROIs) for fNIRS analysis. In this proposed method, we make use of the optical "forward model", which describes the sensitivity of a particular fNIRS source-detector pair to the underlying brain regions based on the diffusion/transport of light in the tissue. The optical forward model is used to create a testable null hypothesis about the involvement of a particular region of the brain using a weighted average of the measurement channels. For example, based on the registration of the fNIRS probe, brain activity from a particular Brodmann area [75] region would be expected to be highest on a specific fNIRS channel with tapered responses to nearby channels. Using this tapered spatial distribution of expected signal changes allows us to create a statistical model of what the fNIRS data would be expected to look like if this region were active in the task. Likewise, this creates a testable null hypothesis – if this signal change in this region was not different from zero then a spatially weighted average over this particular set of channels would also be not differ from zero. If the weighted average over these channels was non-zero, then we can reject this null hypothesis. The rejection of this null hypothesis means that we cannot rule out that this region was active during the task, but does not actually imply that the signal definitely came from this region as opposed to a nearby or smaller region of the brain which was also sampled by this set of channels. Nonetheless, the interpretation of such a result would be that the recorded brain signals are consistent with that particular region's involvement in the task.

Since this method utilizes the optical forward model, it provides means to adjust the null hypothesis based on head-size, probe registration, and/or individual anatomy. For example, the expected projection of a region such as dorsal-lateral prefrontal cortex might be higher on more lateral fNIRS channels in a subject with a smaller head size compared to a subject with a larger head using the same fNIRS probe and spacings. In most cases, particularly in studies of children, knowledge of individual brain anatomy (e.g. via MRI) is not practical, but measurements of head-size, placement of the probe relative to 10-20 locations, or 3-D positioning cameras are often recorded and can be used in this proposed method. In addition, this approach does not require a separate localizer task condition to define the ROI. While the activation maps from a separate localizer task provides an objective way to define an ROI on an individual subject basis, this approach is not always practical. If the localizer task is not exceptionally strong/statistical, there will be uncertainty in the region definitions.

In this paper we describe the theory behind our approach to use individualized tapered weights to define the statistical contrast for regions-of-interest and compare the use of tapered and uniform weighted models. We also examine the effect of small errors in the probe registration on the model performance to examine the method under realistic conditions.

5.3 Theory

5.3.1 Analysis of fNIRS Data

Functional NIRS data is recorded as changes in the light from a source position incident on a detector position (e.g. transmitted between a source-detector pair) as a function of time. These signals are first converted to changes in optical density (optical absorption) over time as given by

$$\Delta OD(t) = -\log\left[\frac{I(t)}{I_0}\right] \tag{5.1}$$

where $\Delta OD(t)$ denotes the change in optical density, $I(t)$ is the intensity of the signal recorded, and I_0 is the reference signal intensity at baseline (usually taken as the mean of the signal over the scan). The optical density changes at wavelength λ are then transformed into estimates of oxy- and deoxy-hemoglobin (HbO/HbR) changes using the modified Beer-Lambert law [76]:

$$\Delta OD^{\lambda} = l \cdot \mathrm{DPF}^{\lambda}\left[\varepsilon^{\lambda}_{\mathrm{HbO}}(\boldsymbol{\Delta}[\mathrm{HbO}]) + \varepsilon^{\lambda}_{\mathrm{HbR}}(\boldsymbol{\Delta}[\mathrm{HbR}])\right] \tag{5.2}$$

where l is the source-detector distance and DPF is the differential pathlength. $\boldsymbol{\Delta}[\mathrm{HbX}]$ is the change in molar concentration, and $\varepsilon_{\mathrm{HbX}}$ is the molar extinction coefficient, where HbX represents either HbO or HbR for oxy- and deoxy-hemoglobin respectively. Note that the differential pathlength and molar extinction coefficient are wavelength dependent.

In most evoked fNIRS studies, a task(s) is repeatedly preformed whilst recording the fNIRS signals. A first level statistical model (subject-level statistics) is then used to examine changes in the fNIRS signals during the task [77, 78, 33]. More formally, the linear regression model is described by the equation

$$\boldsymbol{Y} = \mathbf{X}\boldsymbol{\beta} + \boldsymbol{\varepsilon} \tag{5.3}$$

where $\mathbf{X}$ is the design matrix of the modeled hemodynamic response encoding the timing of stimulus events and $\boldsymbol{\beta}$ is the coefficient (weight) of that stimulus condition for that source-detector channel. This statistical model can be either a block average, deconvolution, or canonical hemodynamic response method (see [33]), which results in an estimated statistical parameter (typically and herein termed $\boldsymbol{\beta}$) and its uncertainty across the spatial channels (herein termed $\mathrm{Cov}_{\boldsymbol{\beta}}$). Specifically, in the case of block averaging or deconvolution, $\boldsymbol{\beta}$ would be the parameter of interest (mean over a time-window, maximum, etc.) computed from the estimated response. In the case of a canonical linear model (or similar), then $\boldsymbol{\beta}$ would be the estimated coefficient for the regression model. In general, β_i, the i-th element of $\boldsymbol{\beta}$, is just a statistical parameter associated with the i-th spatial fNIRS measurement channel upon which we are basing the hypothesis test (e.g. β_i differs from zero). The spatial covariance of this parameter is denoted as $\mathrm{Cov}_{\boldsymbol{\beta}}$.

Based on the estimate of the parameters and their uncertainties over the multiple channels in a fNIRS probe, the calculation of a Students t-statistic for a region-of-interest is given by:

$$t = \frac{\mathbf{c}^{\mathrm{T}}\boldsymbol{\beta}}{\sqrt{\mathbf{c}^{\mathrm{T}}\mathrm{Cov}(\boldsymbol{\beta})\mathbf{c}}} \tag{5.4}$$

The contrast vector ($\mathbf{c}$) denotes the weights given to channels being averaged. In this expression, $\boldsymbol{\beta}$ is a vector denoting the statistical parameter for each spatial channel of the fNIRS probe. Note, this formalism allows for multiple task conditions for each channel, but for simplicity of explanation, we will assume there is only one task-associated parameter (β_i) per measurement channel. In the case of multiple task conditions, the contrast vector is the Kronecker product ($\otimes$) of the spatial contrast vector and the per-task-condition contrast vector and the $\boldsymbol{\beta}$ and $\mathrm{Cov}_{\boldsymbol{\beta}}$ terms contain all tasks and spatial channels.

The statistic defined by Eq. 5.4 can be used to test the following null hypothesis:

$$H_0 : \sum_{i=1}^{N} c_i \cdot \beta_i = \mathbf{c} \cdot \boldsymbol{\beta} = 0 \tag{5.5}$$

where N is the total number of channels. For example, $\mathbf{c} = \left[\frac{1}{3}, \frac{1}{3}, \frac{1}{3}, 0, 0, 0\right]^{\mathrm{T}}$ would be used to average the values of the first 3 (of 6) spatial channels with uniform weights. This contrast vector ($\mathbf{c}$) encodes the null hypothesis being tested, which in this example is that the mean of the first three channels is not different from zero. This is the same expression as used to compute contrast between tasks for a single spatial channel (e.g. Task A verses Task B) where the covariance described between the conditions (e.g. from linear regression analysis) (see [31]).

5.3.2 Proposed Method

A statistically significant β_i (different from 0) represents the signal in the i-th channel has a strong relationship with the modeled hemodynamic response and consequently indicates the area of the cortex efficiently covered by this channel is not inactive. The statistical significance of a linear combination of βs implies the activity of the area covered by the corresponding channels, and the coefficients (weights) of the linear combination can determine the shape of the area. In the previously (Section 5.3.1) shown example, the entire test area consists of the regions covered by the first three channels with equal weights. However, the region-of-interest in an experiment is rarely a combination of areas equally covered by several channels especially the predefined anatomical areas, e.g., Brodmann Areas [75], since the sensitivity to a given area is maximized in the nearest channel and decreases as the distancing from the channel. Thus, we propose that the contrast vector ($\mathbf{c}$) in Eq. 5.4 to control sequence can be used to test the null hypothesis of the non-involvement of specific underlying regions of the brain. Specifically, instead of using uniform weights to sum over a specific set of channels as used in the previous example, we propose to use a tapered contrast vector that peaks on the spatial channel most expected to be active in the hypothesis and lowered based on the relative sensitivity of other channels to this same region. Examining Eq. 5.4, we note that the numerator in this expression is the inner product of the $\mathbf{c}$ and $\boldsymbol{\beta}$ vectors. This inner product is maximized when the two vectors point in the same direction, which implies that the t-statistic will be largest when the spatial distribution of the $\mathbf{c}$ vector matches the expected spatial distribution of the brain activity. Ergo, if the brain activity came from a particular region such as BA-46 defined by Brodmann Areas [75], then the t-statistic will be maximized when the contrast vector has the tapered spatial distribution consistent with the fNIRS probe placement relative to this region. Comparing to the conventionally used uniform weights, the tapered weights increase the contribution of the expected region and decrease that of the noise from other areas. Thus, this is the most conservative test of the null hypothesis. This approach allows us to first pose specific null hypothesis tests about underlying regions of the brain. For example, if BA-46 were not active in the task, then the specific spatial weighing of channels would not differ from zero. While the rejection of this null hypothesis (e.g. finding that the value of the ROI average differs from zero) implies that we cannot rule out that (e.g.) BA-46 was involved in the task, this however does not mean that BA-46 specifically was involved rather than some other nearby region. Secondly, this formalism allows us to statistically test the involvement of different regions. For example, using two separate contrast vectors we can test if the brain activity was more consistent with (e.g.) BA-46 or BA-45 [75] by statistically comparing those two t-statistics.

We propose that this tapered spatial weighting of channels is based on the optical forward model, the registration of the fNIRS probe, and the underlying regional parcellations of the cortex. The optical forward model (Eq. 5.2) defines the sensitivity of the measurements in channel space to underlying changes in the brain space. This model is calculated by estimation or simulation of the diffusion of light through the tissue (e.g. [79, 80]). The optical forward model provides an estimate of the expected signal changes for the fNIRS measurement geometry given by the expression

$$\boldsymbol{Y} = \mathbf{L}\boldsymbol{\mu}_{\text{volume}} \tag{5.6}$$

where $\boldsymbol{Y}$ is the measurement for a specific fNIRS probe, $\mathbf{L}$ is the forward model relating that probe layout and registration to the underlying head/brain, and $\boldsymbol{\mu}_{\text{volume}}$ is the underlying change in optical absorption in the volume. Based on the registration of the fNIRS probe to an anatomical atlas or individual anatomy (if available), the expected relative sensitivity of each fNIRS source-to-detector channel can be estimated from the location and depth of anatomically defined regions through the optical forward model.

To test for statistical activity from specific anatomically based region-of-interest, we can use the optical forward model and Eq. 5.6 to define the hypothesis of what the activity pattern in channel-space should look like based on the location in volume (brain) space. In other words, to form the null hypothesis testing for activity in a specific region-of-interest, the contrast vector is given by

$$\mathbf{c}_{\mathrm{ROI}} = \mathbf{L} \cdot \mathrm{Mask}_{\mathrm{ROI}}(r) \tag{5.7}$$

where the mask vector for a specific region-of-interest is defined by Eq. 5.8, in which r represents each point of cerebral cortex.

$$\mathrm{Mask}_{\mathrm{ROI}}(r) = \begin{cases} 1 & \text{if } r \in ROI \\ 0 & \text{otherwise} \end{cases} \tag{5.8}$$

To generalize this method for multiple conditions comparison, the contrast vector used in Eq. 5.4 can be replaced by

$$\mathbf{c} = \mathbf{c}_{\mathrm{ROI}} \otimes \mathbf{c}_{\mathrm{COND}} \tag{5.9}$$

Here $\mathbf{c}_{\mathrm{COND}}$ is the contrast vector for the pooling of conditions. Then a t-test can be performed using the statistic define by Eq. 5.4 with the proposed contrast vector given by Eq. 5.9.

5.3.3 Example

In this section, we demonstrate the process of contrast vector calculation for a specific ROI and the analysis with the contras vector. Suppose we are interested in whether BA-45 left or BA-46 left is involved in an experiment. In this example, we would also like to test the difference between the activities of the two ROIs. Fig. 5.1 shows the two regions in Colin27 atlas [81] and an example probe registered to the 10-20 system. See Section 5.4.1.1 and Fig. 5.2 for the details of the probe.

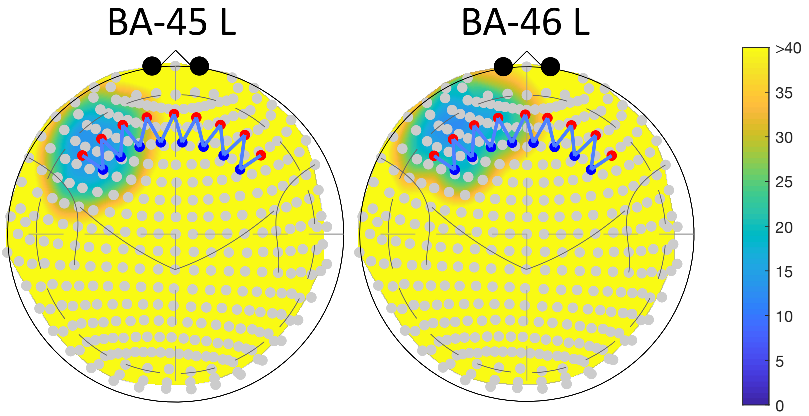

Figure 5.1: The position of the two ROIs – BA-45 L and BA-46 L in Colin27 atlas with a head circumference of 420 mm. The color map represents the depth from each node in the ROI to the head surface. Yellow area indicates a depth greater than 40 mm which is unreachable by the light.

Based on the registration of this probe and the labeled parcellations of the brain (in this case the Taliarach-deamon [82] parcellation of the Colin27 atlas [81]), we can construct a spatially tapered contrast vector using Eq. 5.6 - 5.8. Table 5.1 shows the weights of each channel in the contrast vector. The first two columns are the weights for the two ROIs – BA-45 L and BA-46 L respectively, and the third column contains the weights to test the difference between them, which are obtained by simply subtracting the second from the first column. As a comparison, the conventionally used uniform weights are also listed in the table, which are obtained by assigning equal weights to the nearest four channels to each region.

5.4 Methods

In this chapter, we compare the proposed tapered contrast vector method to the conventional analysis methods using simulation data. We compare two different approaches to

Table 5.1: Each row of the table contains the weights of the channel for the two ROIs and the difference between them. The weights are calculating using Eq. 5.6 - 5.8. It can be seen that a nearer channel has a larger weight. S and D represent source and detector respectively, whose indices can be found in Fig. 5.2. Both the proposed tapered and conventional uniform weights are listed. Note that the remaining channels are omitted from visualization in this table because of their small weights.

fNIRS Channel	**Weights of channels for ROI**					
	BA-45 L		BA-46 L		BA-45 L – BA-46 L	
	Proposed	Uniform	Proposed	Uniform	Proposed	Uniform
S 1 : D 1	0.193	0.25	0.027	0	0.166	0.25
S 2 : D 1	0.209	0.25	0.121	0	0.089	0.25
S 2 : D 2	0.314	0.25	0.224	0.25	0.09	0
S 3 : D 2	0.213	0.25	0.23	0.25	-0.017	0
S 3 : D 3	0.053	0	0.137	0.25	-0.084	-0.25
S 4 : D 3	0.014	0	0.13	0.25	-0.116	-0.25
S 4 : D 4	0.003	0	0.095	0	-0.092	0
S 5 : D 4	0.001	0	0.026	0	-0.026	0
S 5 : D 5	0	0	0.007	0	-0.007	0

computing the region-of-interest contrast: 1) in the **uniform** weighting scheme, the four channels closest to the underlying region-of-interest are selected, and these channels are given a uniform weighting in the contrast vector; 2) in the **tapered** weighting scheme, the forward model is used to compute the relative contribution of the region to each channel based on head size and probe registration. For the both weighting schemes, we additionally examined the case in which this registration information is known accurately and where it is subject to experimental measurement errors, which is described in Section 5.4.1.3. Here the weights are calculated based on the head-size and probe registration of each subject. The unknown condition was examined to mimic the realistic case of experimental error in the registration, in which the weights are calculated based on the average head-size regardless of probe registration error and individual head-size differences. In each iteration of the simulation, we generate a group set of fNIRS data containing five subjects with the same stimulus within the region of the brain and perform group-level channel-space analyses using contrast vectors containing weights of different channels using both the proposed tapered weights for all channels and uniform weights for the nearest channels with both assumptions that the probe registration is known and unknown. In total, there are four analysis conditions, tapered-known, tapered-unknown, uniform-known, and uniform unknown, in each simulation iteration. The analysis results of the two methods are investigated via receiver operating characteristic (ROC) and compared to each other.

5.4.1 Probe Configuration

In this work, two types of probe configuration: low-density and high-density probe, are used for simulations. While the low-density style of probe configuration is much more frequently used in fNIRS studies due to practical reasons, this style of probe has "blind-spots" due to regions of low-sensitivity to underlying brain activity [83]. Thus, low-density probes are more sensitive to displacements in the registration of the fNIRS probe and/or variations in subject head-size. In contrast, high-density fNIRS probes (e.g. [83]) have more uniform spatial sensitivity and less blind-spots, but are more complex to record from and only supported by a few instrument manufacturers.

5.4.1.1 Low-density Probe The low-density probe contains nine light sources and eight detectors. The distance between source and detector alignments is 25 mm. The optical density is only measured between the nearest source-detector pairs. Hence, there are 16 × 2 (two wavelengths, 16 channels for HbO and the other 16 for HbR) channels defined in the low-density probe. An equal weight, $\frac{1}{4}$, is assigned to each of the nearest four channels to construct the uniform contrast. Fig. 5.2(a) shows the 2D layout of the probe.

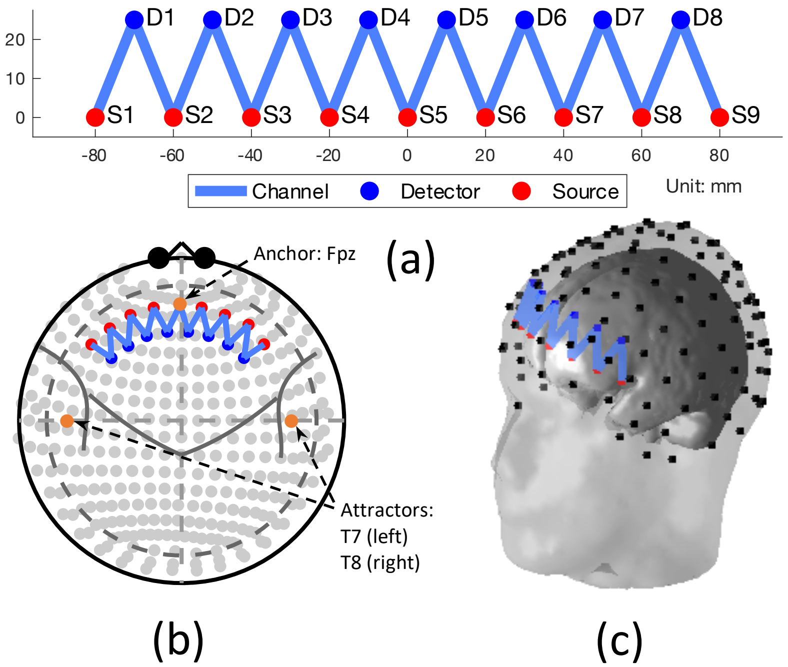

Figure 5.2: The topology of the low-density probe used in the simulation: (a) The 2D layout, (b) The registered probe with 10-20 International System, and (c) The registered 3D probe geometry. A head with 420 mm circumference is used in (b) and (c).

The registration of the probe is defined by an anchor and three attractor positions on the probe . Similar to the use of these terms in the AtlasViewer program [10], anchors and attractor positions help to register the fNIRS probe onto the 10-20 coordinate system. In the Brain AnalyzIR toolbox [31], an anchor forcibly fixes a point of the probe layout (Fig. 5.2(a)) on the 10-20 system placement. In this case, the origin of the probe (0, 0) in the two-dimensional layout is anchored to the 10-20 site Fpz. An attractor provides directional information to the probe. Here, three attractors are placed at positions (±200,

0) and (0, 100) in the two-dimensional layout are attached to T7, T8, and Cz respectively, which define three forces pulling the probe along negative/positive X-axis and positive Y-axis pointing to T7, T8, and Cz. The registration algorithm uses an iterative least-squares minimization algorithm based on the optimal source-detector pair spacings and the location of the anchor/attractor points. Attractor points are used to construct unit vectors to provide direction, which are updated with every iteration of the algorithm. The registered probe used in this example is shown in Fig. 5.2(b) and (c) using 10-20 (Mercator) projection and 3D geometry on an example head with 420 mm circumference.

5.4.1.2 High-density Probe The high-density probe used in this work is suggested by Zeff et al. [83]. Measurements are made between the first-, second-, third-, and fourth-nearest neighboring source-detector pairs, the separation of which are 13, 30, 40, and 48 mm [83] respectively. The distance between two neighboring sources or detectors can be consequently calculated as $13\sqrt{2} = 18.385$ mm. Instead of 24 sources and 28 detectors used in the previous study [83], we added six sources and detectors for covering a similar length of area with the low-density probe used in Section 5.4.1.1. Thus, our high-density probe contains 30 sources and 36 detectors, which form 460×2 channels in total. To be comparable with the low-density probe, a quarter of the channels (115/460) are used to calculate the uniform contrast vector with equal weights. The 2D layout of the high-density is shown in Fig. 5.3(a).

The anchor and attractors used in the high-density probe registration are same as those for low-density probe defined in Section 5.4.1.1. Fig 5.3(b) and (c) present the high-density probe registration in 10-20 system and 3D geometry on a head with 420 mm circumference.

5.4.1.3 Probe Registration with Head Size and Displacement Consideration In this work, in addition to examining the ideal case in which the fNIRS probe registration and head/brain size are perfectly known, we also examined the realistic case in which these parameters had unknown errors associated with them. In particular, it is conceivable that using error-prone prior (miss-)registration information could actually hurt the accuracy of the analysis methods and we wished to examine the sensitivity of the method to these errors. Fig. 5.2(b) and Fig. 5.3(b) show the ideal situation of the probe registration, in which the

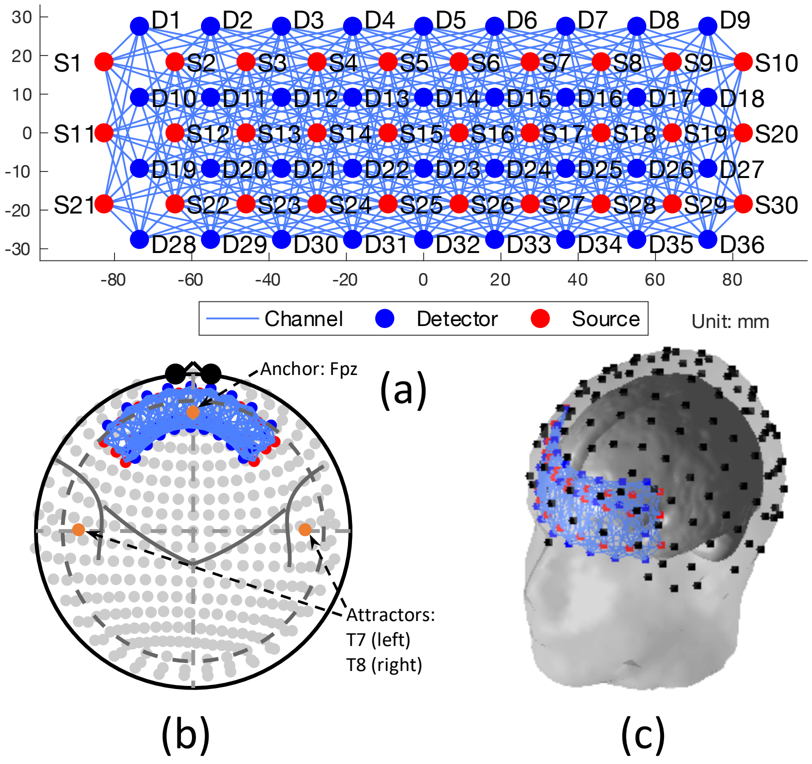

Figure 5.3: The topology of the high-density probe used in the simulation: (a) The 2D layout, (b) The registered probe with 10-20 International System, and (c) The registered 3D probe geometry. A head with 420 mm circumference is used in (b) and (c).

head size is known, and the anchor and attractors are placed without any errors. However, in most practical fNIRS experiments, the subjects' head circumferences are not recorded, and placement errors are unavoidable. We use random head-sizes and probe registration errors in this study. In our simulation, the head circumferences are generated from a normal distribution with a mean of 420 mm and a standard deviation of 50 mm. The lower and upper 2.5% quantiles of this distribution are 318.08 mm and 521.92 mm. This was chosen such that the simulated head circumference falls into the head-size range of 0 – 36 months infants [84] with a 95% probability. To simulate the registration error, the anchor and attractors are placed at a position that deviates from the original position by a random distance. The displacements along X- and Y-axis are both randomly generated from a normal distribution with a zero mean and a standard deviation of 10 mm. Since the upper 2.5% quantile of this distribution is 19.60 mm, Fpz falls into a square with a center at (0, 0) of the probe layout and an edge of 39.20 mm with a probability of 1 − 5% × 5% = 99.75%. Similarly, in 95% cases, The X- and Y-axis of the probe are pulled to T7/T8 and Cz with angle errors in the ranges of ±5.60° (arctan(19.60/200)) and ±11.01° (arctan(19.60/100)) respectively.

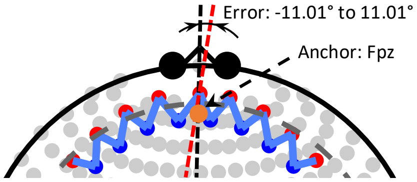

Figure 5.4: An example of probe registration with displacement error. Comparing to Fig. 5.2(b), the registered probe is asymmetric. The red dashed line is the centerline of the probe, which is not coincide with the brain centerline (the vertical black dashed line). As explained above, the middle light source, S5 at (0, 0), deviates from the anchor point Fpz, and the angle between the two centerlines is in the range of (-11.01°, 11.01°). The left and right part of the probe may independently rotate around the probe centerline (red dashed line) by an angle between -5.60° and 5.60°

Fig. 5.4 is an example of probe registration with a larger head circumference (485 mm) and random error. Comparing to Fig. 5.2(b), the middle light source of the probe is not placed exactly on the anchor point, which is caused by the placement error. It can also be seen that there is an angle between the two centerlines in a range of ± 11.01°. The left and right part of the probe may independently rotate around the centerline of the rotated probe by an angle within ± 5.60°. Therefore, even in the worst case, each of the left and right part is unlikely to deviate from the ideal position more than 16.61° (the probability exceeding this value is 5% × 2.5% = 0.125%).

5.4.2 Region-of-Interest Selection

As mentioned in Section 5.3.2, two types of analysis are performed in this work – the involvement of a specific ROI and the difference between the activities of two ROIs, which can be described as two statistical tests: (1) test if the hemodynamic response within a specific ROI is significantly different from zero, and (2) test if there is a statistically significant difference between the hemodynamic responses in two nearby ROIs. For the single ROI analysis, the size of the region is considered as a factor in the simulation. Besides, the distance between the two nearby ROIs is taken into account as another factor in the ROI difference analysis. The selection of ROIs for these two types of analyses is described in the following two subsections.

5.4.2.1 Single ROI Analysis The ROI used in this work is created using a spherical surface with a center at a node (brain coordinate) from Colin27 atlas [81] and a specified radius. All nodes included within the sphere define the ROI. Because of the symmetry in cerebral cortex, we only select ROIs and generate stimulation in the left cerebral hemisphere while the mirrored ROIs in the right hemisphere are used as the null regions (containing noise only) to evaluate the false positive rate (FPR) of the analysis. Fig. 5.5 is an example of ROI selection.

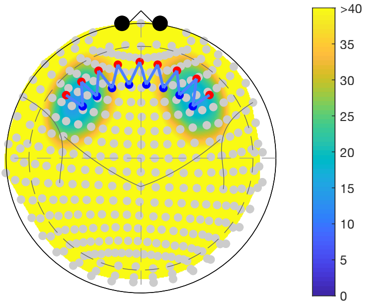

Figure 5.5: An example of ROI selection. The color map represents the depth from each node in the ROI to the head surface. Yellow area indicates a depth greater than 40 mm which is unreachable by the light. The stimulation is generated within the ROI in the left hemisphere while the right one is used as the null region.

Note that the distance between the center node of each ROI and the nearest optode must not exceed the specified radius of the ROI, so the ROI can be reasonably covered by the probe. Another consideration for ROI selection is the head size. To perform a reasonable group-level analysis, the relative size of each ROI to the entire cerebral cortex must be comparable between subjects. In this study, the nodes included in an ROI are selected using the standard Colin27 atlas, then the coordinates of the nodes are scaled according to the head circumference ratio.

5.4.2.2 Statistical Testing between Two ROIs The selection process for ROI difference analysis is similar to that for single ROI analysis but involving the distance between two ROIs as a new factor. Fig. 5.6 is an example of ROI selection for difference analysis. For the same reason, which is described in Section 5.3.1, we only generate stimulation within one of the two ROIs in the left hemisphere and calculate the difference. The two mirrored ROIs in the right hemisphere are considered as null region, the difference which is used to evaluate the FPR.

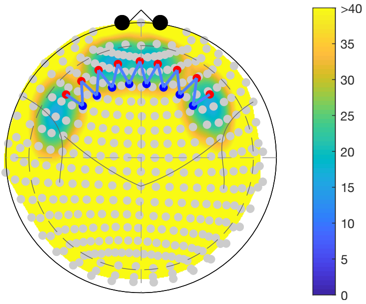

Figure 5.6: An example of ROI selection for region difference analysis. The legend is same as that in Fig. 5.5. Note that it looks like the ROIs in left and right hemispheres overlap to each other, but they do not actually because of the existence of cerebral fissure.

One more factor, the distance between the two ROIs, is taken into consideration besides head size and ROI radius. We firstly select an ROI using the method described in Section 5.3.1 and generate stimulation within it, then find out all nodes that deviate the center of the ROI by a specified distance, from which the second ROI used to calculate the hemodynamic difference is randomly selected.

5.4.3 Stimulus Generation

The fNIRS data is simulated by adding stimulation on autoregressive noise. The time difference between two neighboring stimuli is exponentially distributed. The hemodynamic response to the stimulus is simulated using canonical hemodynamic response function. In brief, simulated "brain" activity within the ROI (true positive) is computed and projected to fNIRS channel/measurement space via the optical forward model. The contralateral ROI is used to define the true negative region for ROC analysis. Additive autoregressive noise is added to all channels at an SNR level of 1. The details are described in Ref. [31].

5.4.4 ROC Analysis

With the p-value reported from the t-test (Eq.5.4), we calculate the FPR and true positive rate (TPR) using (1 - p-value) as the threshold, since smaller p-value indicates more significant HbO and HbR changes. The ROC curve can then be constructed, and the area under the curve (AUC) is the probability that the hemodynamic responses within the stimulus-containing ROIs are more significant (with a smaller p-value) than that in the null ROIs. Thus, AUC is utilized as the indicator for analysis performance evaluation. To determine whether a method is significantly better than another, the null hypothesis that their AUCs are equal is tested. The z-statistic is defined as

$$z = \frac{|\mathrm{AUC}_1 - \mathrm{AUC}_2|}{\mathrm{Se}(\mathrm{AUC}_1 - \mathrm{AUC}_2)} \tag{5.10}$$

where Se() is the standard error. The standard error of the AUC difference is estimated using DeLong's method [51]. The p-value for the abovementioned null hypothesis can finally be reported.

An appropriate statistical model should give evenly distributed p-values when the null hypothesis is true, i.e., p-values smaller than a threshold (commonly called type-I error control, α) will be considered as false positives, and the FPR is the empirical type-I error rate. Thus, we check the relationship between empirical FPR and the model-reported p-value. In an ideal situation, they are equal and the plot of FPR vs. p-value is the diagonal of the plotting square. Otherwise, the type-I error rate is over- or under-estimated.

5.4.5 Summary of Simulation

The probe registration, noise and stimulus generation, and data analysis are implemented using Brain AnalyzIR toolbox [31]. A total of 20 individual ROIs were selected. For each ROI, the radius of the region was examined from 10 mm to 36 mm by 2 mm steps (14 values total). This yielded a total of 280 regions which were used to generate simulated activity for the five subjects for the group analysis with randomly selected head sizes. In the case of simulations with additional registration error, uncertainty was added between the probe registration and forward model used to generate the data and the one used in the analysis. Each group simulation for each ROI was repeated 100 times, for a total of 28,000 simulations. For examining the statistical test between two ROIs, a second ROI of the same radius was added at a distance between 20 mm and 80 mm at 5 mm steps (13 values in total) for each of the simulations (364,000 total simulations for each of the two probe types). For each simulation parameter combination, the analyses are respectively performed with two assumptions: (1) head-size and probe registration error are known, where the contrast vectors are calculated based on the actual registered probe, (2) head-size and probe registration error are unknown, where the contrast vectors are calculated based on the probe registered to the average head size (420 mm circumference) without registration error.

5.4.6 Implementation in the Brain AnalyzIR (nirs-toolbox)

The calculation of the contrast vector for a given ROI has already been implemented in the Brain AnalyzIR toolbox [31]. This is an open-source analysis toolbox written in MATLAB for fNIRS. The main components in the implementation are described in this section.

5.4.6.1 Forward Model The AnalyzIR toolbox includes interfaces to several third-party optical forward model solvers including NIRFAST [79, 85], Mesh-based Monte Carlo (MMC; [86, 87]) and Monte Carlo Extreme (MCX; [25, 88]). This code allows construction and import of individual head models from anatomical MRI volumes to generate subject-specific optical forward models and registration. These solvers can be used with either atlas-based or individual head models to generate this optical forward model. However, since the computation of multiple optical forward models is often time consuming and furthermore this level of anatomical modeling is often not available for all subjects (e.g. pediatric fNIRS studies), the default options in the AnalyzIR toolbox make use of a pre-segmented head model derived from the Colin-27 atlas [81]. Furthermore, to achieve fast computation of the sensitivity of a particular fNIRS channel to the underlying brain region, a simplified optical forward model is approximated using the closed-form solution for the semi-infinite homogenous slab geometry [89] to compute a particular two-point Green's function solution to the diffusion model (e.g. the relationship light traveling from a point on the surface to a point in the volume). The sensitivity of a source-detector pair is then computed as the three-point Green's function combining two obliquely oriented slab-based two-point functions. This approximation of the optical forward model (termed the ApproxSlab forward model in the toolbox) was found to give a reasonable approximation compared to formal solutions using finite element or Monte Carlo methods, particularly given the existing approximations and errors associated with the use of the Colin-27 atlas. We note also that the Brain AnalyzIR toolbox does support the use of these proper finite element or Monte Carlo solvers to compute a more accurate forward solution, but as mentioned due to the computational time involved (several minutes per contrast vector compared to a few hundred milliseconds for the ApproxSlab model), the default in the toolbox is to use this approximate solution. All results in this work used this approximate solution.

In addition, to avoid the complexities of multi-variate statistical testing between oxy- and deoxy-hemoglobin and multiple optical wavelengths inherent to the Beer-Lambert law, we approximate the forward model using only a single wavelength (default at 808 nm), which allows us to compute the spatially tapered contrast weight that can be applied to the statistical parameters ($\boldsymbol{\beta}$) defined in oxy- or deoxy-hemoglobin. Note that the tapered contrast vector used in the ROI definitions is normalized such that the value of the extinction coefficient for oxy- or deoxy-hemoglobin at that wavelength is irrelevant to the calculation.

5.4.6.2 Labeling of Regions As mentioned previously, Colin27 atlas is used as the default anatomical model for probe registration in this work. To identify the voxels contained in a specific ROI, a parcellation of the anatomical model is required. Considering the generality, random self-defined ROIs are used in this study rather than the predefined Brodmann Areas [75]. Thus, instead of the Broadmann labeling [75], here the Talairach daemon [90] defines the ROIs, which gives a high-resolution parcellation of the brain and allows us to define high-resolution ROI.

5.4.6.3 Resizing of Colin27 Atlas Since the effect of the head size is investigated in this study, the anatomical model needs to be scaled for different head circumference and dimensions. In the AnalyzIR toolbox, the atlas head size can be rescaled based on the experimental measurements of the head circumference, nasion-inion (Nasion – Cz – Inion) and left/right periocular point (LPA – Cz – RPA) distances over the top of the head where the head circumference is computed 10% above the contour of nasion – right preauricular point (RPA) – inion – left preauricular point (LPA) – nasion. These three measurements uniquely define the resizing of the head as an ovoid shape to match each subject. Alternatively, when only one of these three measurements is available (e.g. head circumference only) the head can be resized proportionately keeping the ratios of the major and minor axis of ovoid fixed. In this case, for a given head size, we calculate the ratio of the given head circumference to the standard model's, then resize the atlas by multiplying the Talairach coordinates [91, 92] of every point by the ratio of their head circumferences. As a result, the portion of a specific ROI will be the same in the scaled atlas. In the Brain AnalyzIR toolbox, registration of a fNIRS head cap to a brain model is done in two steps to i) first register the cap to the ovoid (spherical) 10-20 coordinate system and then ii) register and resize the head/brain model into the same ovoid 10-20 space.

5.5 Results

The results of ROC analysis and statistical testing of the simulations are shown in this section. To be concise, we use "known" and "unknown" registration to respectively denote the analysis conditions that the contrast vectors are calculated based the actual probe registration (known head size and registration error) and average registration (unknown head size and registration error) in the following context. For the same purpose, ROI radius and separation are used to denote the radius of the spherical surfaces defining the ROIs and the distance between the center nodes of them.

5.5.1 Single ROI Analysis

In this section, we examined the performance of the uniform and proposed tapered contrast vector methods to infer changes about a single region of interest in the brain. The size of the region-of-interest was varied from 10 – 36 mm. The methods were examined in the case of both ideally known and unknown (errors) in the probe registration model.

Fig. 5.7 is an example of ROC curves of the two analysis methods. The images in panel (a) demonstrate the full ROC plots for the case of the 14 mm ROI radius. In the case where the probe registration information is known, the area-under-the-curve (AUC) for the uniform and tapered contrast vectors, for HbO/HbR, are 0.910/0.868 and 0.937/0.897 respectively for the 14 mm radius. When additional registration error is introduced and unknown as described in Section 5.4.1.3, the AUC values are 0.897/0.850, and 0.913/0.865. In both the known and unknown cases, the AUCs are statistically smaller ($p < 10^{-5}$) for the uniform compared to the tapered contrast vector. Panel (b) shows the AUC as a function of the ROI radius, in which the AUC values were fairly consistent across the tested ROI radius sizes. The tapered contrast vector performs consistently better under all conditions than those with the uniform contrast vector. We also observed that the method using the uniform contrast vector demonstrates more fluctuation when the ROI radius is greater than 28 mm. We believed that this is caused by the gyrus and sulcus since this size is close to the thickness of gyrus and depth of sulcus. In this case, the ROI would include multiple gyrus, the space between which may reduce the statistical power of the analyses. Since the contrast vector for weighted-channel is calculated based on the forward model, it already takes the anatomy into consideration and consequently reduces the AUC fluctuation for large ROIs. Statistical tests for the AUC difference between the analyses using the two types of contrast vector are performed for each simulation ROI radius, i.e., 56 tests (14 radius values

× known/unknown conditions × HbO/HBR) are conducted in total. The p-values of the tests for the 28 AUC differences knowing the registration error are all less than 10^{-6}, which implies that the proposed method performs significantly better than the uniform contrast vector method under this condition. For the unknown condition, although the AUCs of the tapered contrast vector method decrease comparing to that when registration information is known, most of the 28 p-values of the tests for the difference between the two methods are smaller than 0.05. The only exception is the AUC for HbR analysis with a ROI radius of 20 mm, the p-value for which is 0.109. It exceeds the commonly used significance level 0.05, however, just slightly larger than 0.1. It can still be concluded that the proposed method performs significantly better than the conventional uniform contrast vector method no matter the head size and probe registration error is known or not.

In addition to examining the performance of the ROC analysis with the AUC, we examined the control of the type-I error by comparing the empirically determined false-positive rates (FPR) with the theoretical values (denoted as $\hat{p}$ [p-hat]). Mismatch between the FPR and $\hat{p}$ indicates either over- or under-estimation of the true significance of the results. Fig. 5.8 (a) shows the results of the plot of the FPR vs. $\hat{p}$ for the simulation with ROI radius of 14 mm. It can be seen from Fig. 5.8 (a) that the empirical curves are both below the ideal one at the beginning part where FPR and $\hat{p}$ are small. However, they do not remarkably deviate from the ideal curve, so we do not think it is a serious problem. Fig. 5.8 (b) shows the empirical FPR for the two analysis methods calculated from simulations with different ROI size under the commonly used type-I error control, a.k.a., significance level α, of 0.05. All data points lay below the dotted line, which indicates that these two methods both underestimate the type-I error with a similar performance. Although type-I error is underestimated by both methods for all ROI radii, we also checked every the empirical curves to make sure the p-values are still generally evenly distributed (similar to Fig. 5.8 (a)). One usually worries about the underestimation of type-I error because it may result in an overestimated type-II error and consequently affect the ROC performance. However, the large AUCs demonstrate the good performances of both methods under all conditions. Thus, we believe the concern for the underestimation of type-I error at small $\hat{p}$ is unnecessary.

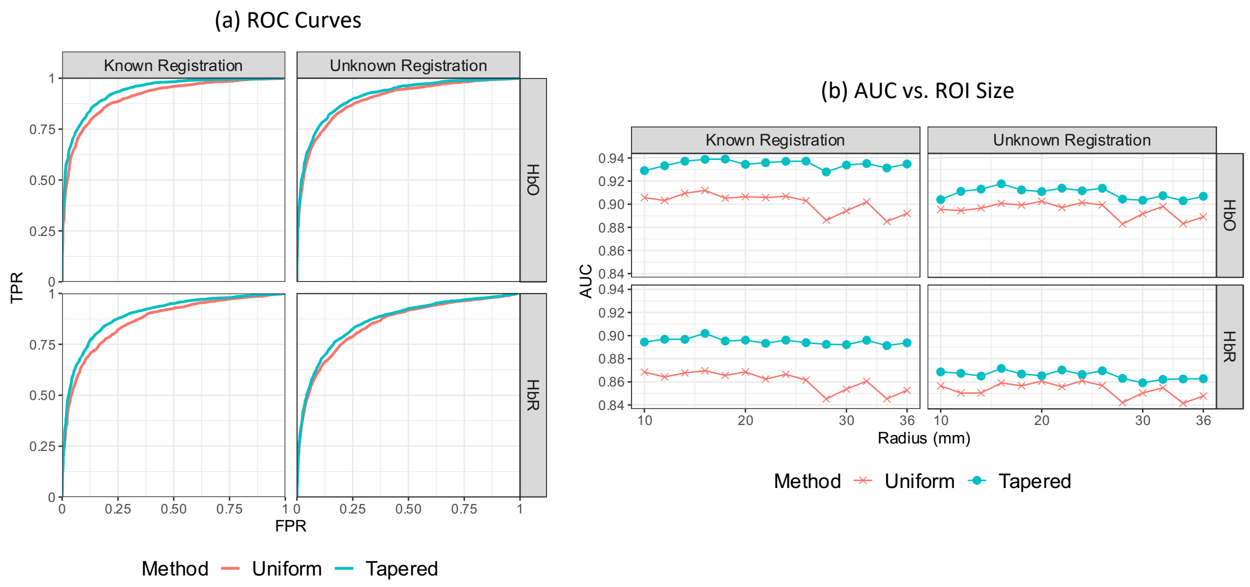

Figure 5.7: Comparison of analysis methods with uniform and tapered contrast vector using receiver operating characteristic (ROC). (a) Each subplot shows the ROC curves of recognizing the hemoglobin activity within a single ROI using the two type of contrast vector (indicated by color) for data with ROI radius = 14 mm from 2000 iterations of simulation under the conditions where the probe registration information (including head size and registration error) is known or not (indicated by column). The two rows indicate oxy-/deoxy-hemoglobin respectively. (b) Each subplot shows the ROC AUC as a function of ROI radius. Every data point represents the AUC calculated from 2000 simulation iterations against the corresponding ROI radius (in mm) used in the simulation.

5.5.2 Comparison of Two ROIs

In addition to testing the null involvement of a specific region-of-interest, our proposed approach can be used to compare multiple regions-of-interest to each other. In order to examine this, we performed a series of simulations as previously outlined. In addition to varying the location, ROI radius, and probe type, to compare two regions, we also varied the distance between the two regions to examine the limits of this approach. Similar to the

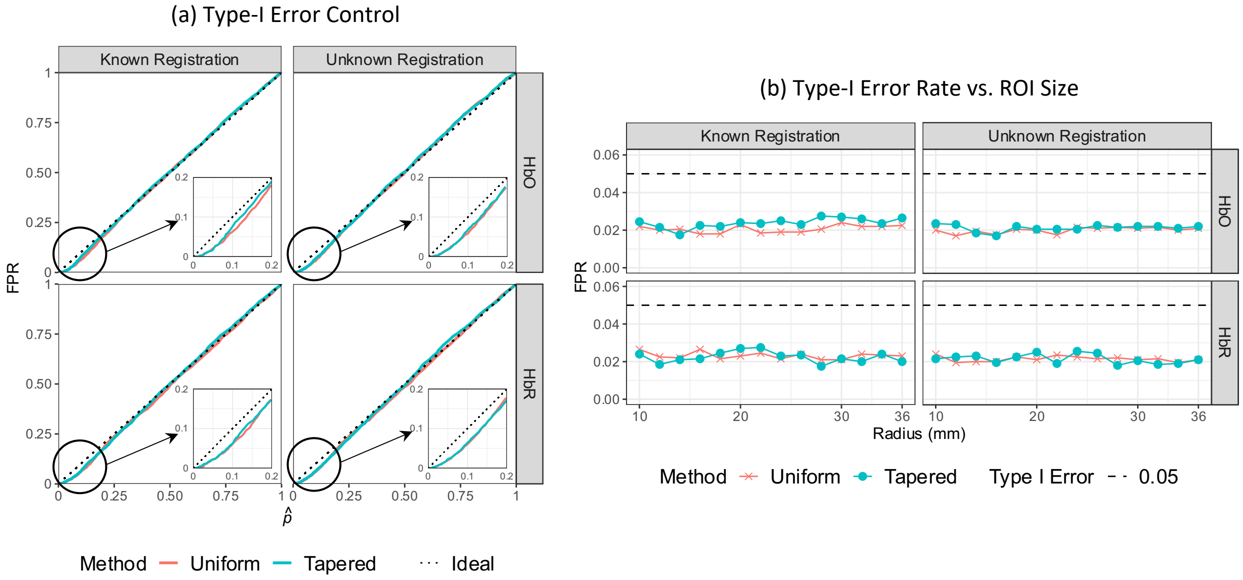
(a) Type-I Error Control

(b) Type-I Error Rate vs. ROI Size

Figure 5.8: Comparison of analysis methods with uniform and tapered contrast vector using type-I error control. (a) Each subplot shows the empirical FPR vs. reported p-value curves of recognizing the hemoglobin activity within a single ROI using the two type of contrast vector (indicated by color) for data with ROI radius = 14 mm from 2000 iteration of simulations under the conditions where the probe registration information (including head size and registration error) is known or not (indicated by column). The two rows indicate oxy-/deoxy-hemoglobin respectively. In an ideal situation, the empirical FPR equals to the model-reported p-value, which is represented by the dotted diagonal of each plot. Both methods underestimate the FPR at smaller p-values (zoomed in and embedded at the corner) (b) Each subplot shows the ROC AUC as a function of ROI radius. Every data point represents the AUC calculated from 2000 simulation iterations against the corresponding ROI radius (in mm) used in the simulation. Every data point represents the empirical FPR calculated from 2000 simulation iterations against the corresponding ROI radius (in mm) used in the simulation. Here 0.05 is used as the type-I error control (threshold) that is indicated by the dashed line.

characterization of the single ROIs, we preformed simulations to quantify the sensitivity and specificity of the approach in comparison to the use of a fixed and uninform ROI.

Fig. 5.9 is an example of ROC curves of the two analysis methods for both the low-density and high-density probes, in which 10 mm and 80 mm are used as the ROI radius and separation respectively. For the low-density probe, the AUCs of the two methods, uniform and proposed tapered contrast vector for HbO/HbR when the probe registration information is known are 0.622/0.605 and 0.696/0.673 respectively, and the values when the probe registration information is unknown are 0.576/0.570 and 0.684/0.671. For the high-density probe, these values were 0.550/0.529 and 0.724/0.685 for the known probe registration case and are 0.531/0.530 and 0.691/0.654 for the unknown case. In all comparisons, the tapered contrast vector approach preformed statistically better ($p < 10^{-5}$) than the uniform weighing approach.

Fig. 5.10 shows the AUC of the two methods for the ROI difference analysis by varying the ROI size and separation in the simulation, from which we can see that the analysis using the spatially tapered contrast vector performs consistently better than that using uniform contrast vector under all conditions since its AUCs are in a higher color range. By performing statistical tests for the AUC differences between the two methods for the simulations using low-density probe, i.e., comparing each pair of small colored rectangles at a corresponding position in the lattices of panels (a) and (b), we obtained significant p-value (smaller than 0.05) for each pair of AUCs using tapered and uniform contrast vector across all ROI radius, separation distance, and analysis conditions. The maximum p-values is 0.0257 for the AUCs comparing the HbR changes within two ROIs with 16 mm radius separated by 25 mm knowing the probe registration error. Similar tests are conducted for the high-density probe simulations, i.e., panels (c) and (d), as well, in which the all obtained p-values are smaller than 0.05. uniform contrast vector across all ROI radius, separation distance, and analysis conditions. The maximum p-values is 0.0250 for the AUCs comparing the HbO changes within two ROIs with 36 mm radius separated by 80 mm without knowing the probe registration error. We can conclude that the proposed method performs significantly better than the conventional methods for ROI difference test using both low- and high-density probes.

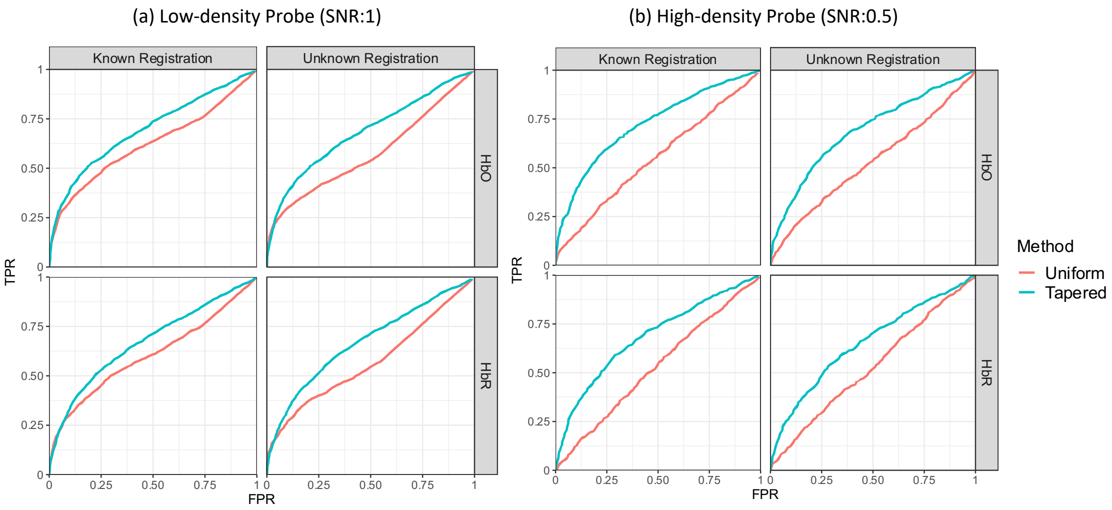

Figure 5.9: Each subplot shows the ROC curves of recognizing the hemoglobin activity difference between two ROIs using the two types of contrast vector (indicated by color) for data from 2000 iterations of simulation under the conditions where the probe registration information (including head size and registration error) is known or not. The simulated activities are generated within one of the two 10 mm (radius) ROIs separated by 80 mm, and two types of probe, low-density (panel a) and high-density (panel b), are used in the simulation. The column and row of each subplot indicate known/unknown probe registration and oxy-/deoxy-hemoglobin respectively.

Finally, we examined the type-I error control for the comparison of two ROIs using the tapered and uniform approaches. In Fig. 5.11, we demonstrate these results for simulations using ROI radius of 10 mm and separation of 80 mm. In comparison to the single ROI analysis (shown in Fig. 5.8), we found that using uniform contrast vector consistently underestimates the FPR in the case of the low-density probe. It can be seen from the panel (a) that the $\hat{p}$ reach 1 where the FPRs using uniform contrast vector are only 0.55 and 0.74 when the probe registration is known and unknown respectively. This means that in 45% and 26% of cases, this method is not able to distinguish between the two ROIs anyway. The reason is that the uniform contrast vectors for the two ROIs can be exactly the same when the

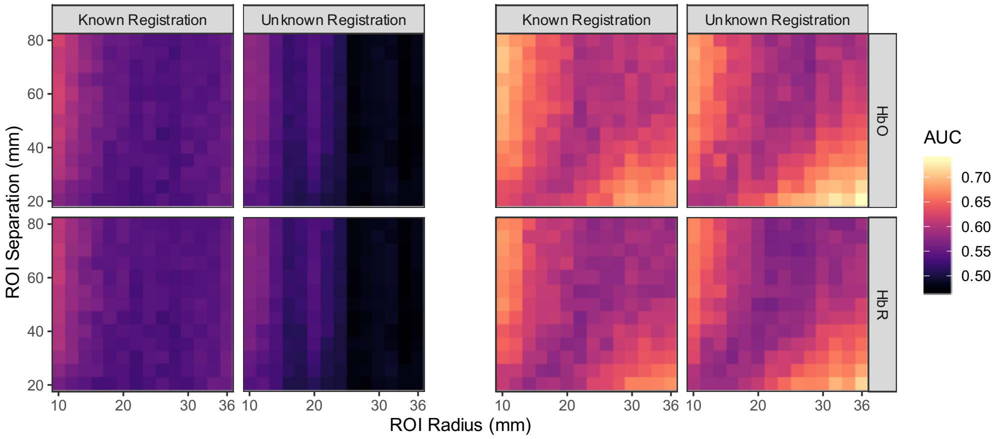
(a) Uniform w/ Low-density (SNR:1)

(b) Tapered w/ Low-density (SNR:1)

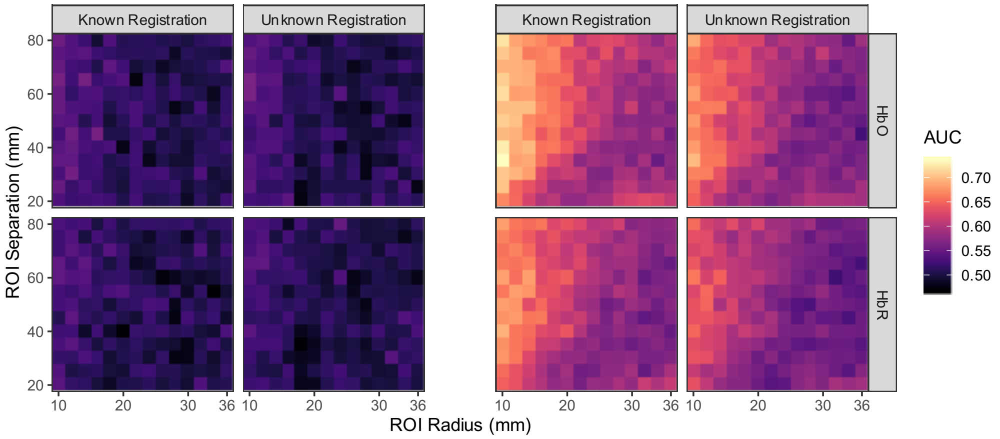
(c) Uniform w/ High-density (SNR:0.5)

(d) Tapered w/ High-density (SNR:0.5)

Figure 5.10: The heatmap showing the AUCs of recognizing the hemoglobin activity difference between two ROIs for simulation data under the conditions where the probe registration information is known or not. The color of each small rectangle in the lattices, whose scale is indicated by the legend, represents the AUC calculated from 2000 simulation iterations using its abscissa and ordinate as the ROI radius and separation respectively. Two types of probe, low-density (panels a and b) and high-density (panels c and d), are used in the simulations, and the left (a and c) and right (b and d) two panels contain the results using uniform contrast vector and tapered contrast vector respectively. Within each panel, the column and row of each subplot indicate known/unknown probe registration and oxy-/deoxy-hemoglobin respectively.

two ROIs are close enough to each other, which results in an all-zero contrast vector for the ROI difference test and consequently a zero t-statistic giving a unity p-value. In the case of using tapered contrast vector, the two contrast vectors will never be the same no matter how close they are as long as not completely overlapping to each other. Therefore, the $\hat{p}$ reported by the tapered contrast vector method appropriately estimate the empirical FPR, which demonstrates this method has a higher spatial resolution than the other two. This also explains why ROC curves of uniform contrast vector-based method achieve the diagonal at 0.55 and 0.74 in Fig. 5.9 (a). This is the motivation we investigated this problem again using high-density probe who has a higher spatial resolution and is expeted to improve the type-I error rate with the uniform contrast vector. For the high-density probe (Fig. 5.11 (b)), the type-I error is slightly underestimated for the uniformly weighted model which results in increased false-positives. However, the two ROIs are more distinguishable. In both probes, the proposed tapered contrast vector appropriately estimates the FPR.

In Fig. 5.12, the FPR at $\hat{p} = 0.05$ is shown for various ROI radii and separation distances. The four panels represent same analyses as those in Fig. 5.10. The colors in the heatmap of the tapered contrast vector method, i.e., panels (b) and (d), fall into the range around 0.05 with both low-and high-density probes, which indicates the FPR estimation is generally appropriate. For the uniform contrast vector method, i.e., panels (a) and (c), the colors are completely out of the appropriate range when low-density probe is used. For a given ROI separation distance, the FPRs reported by the uniform contrast vector method decrease and deviate further from the type-I error control $\hat{p} = 0.05$ because the enlarging overlap of the two ROIs makes it more difficult to distinguish between the two ROIs. For the case of using high-density probe, although most of the colors are in an appropriate range, it can still be seen that the type-I error rate is overestimated for small ROIs with large separation (note that darker color represents a larger value in panel (c) and (d)). However, the plots of the worst case (10 mm radius and 80 mm separation) have been shown in Fig. 5.11(b), from which we can see that the empirical curves do not significantly deviate from the ideal curve.

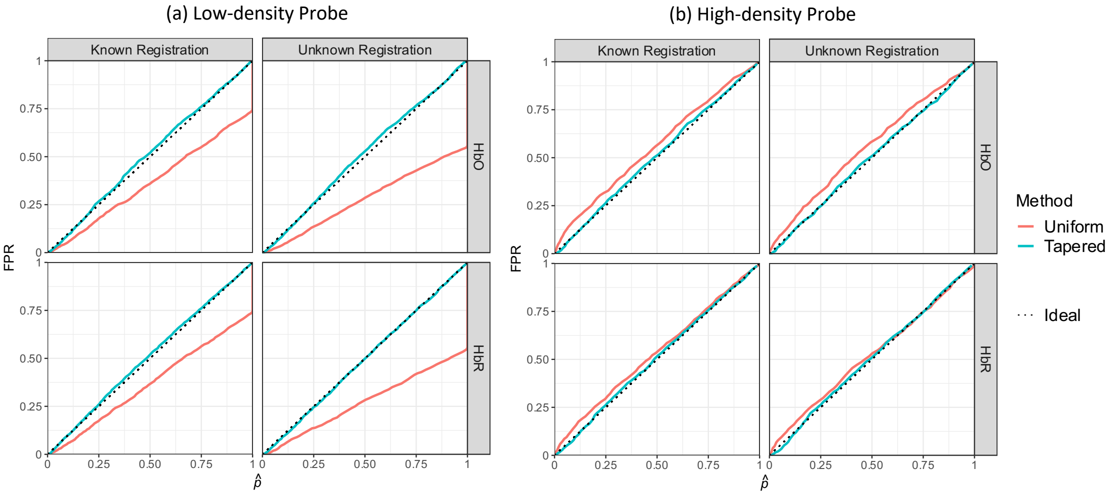

Figure 5.11: Each subplot shows the empirical FPR vs. reported p-value curves of recognizing the hemoglobin activity difference between two ROIs using the two types of contrast vector (indicated by color) for simulation data analyses under the conditions where the probe registration information is known or not. The simulated activities are generated within one of the two 10 mm (radius) ROIs separated by 80 mm, and two types of probe, low-density (panel a) and high-density (panel b), are used in the simulation. The column and row of each subplot indicate known/unknown probe registration and oxy-/deoxy-hemoglobin respectively. For a single curve, the abscissa of each data point is the FPR using its ordinate as the threshold. In an ideal situation, the empirical FPR equals to the model-reported p-value, which is represented by the dotted diagonal of each plot.

5.6 Discussion and Conclusions

In this paper, we show the analysis results of thousands of simulations using 2 (probe layouts) × 14 (radius lengths) × 13 (separation distances) = 364 parameter combinations. Here we discuss the findings and draw conclusions in the following aspects.

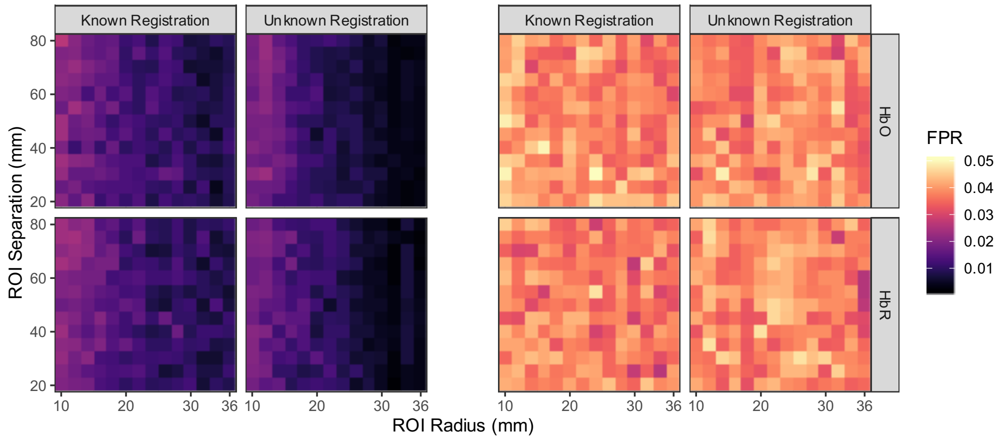
(a) Uniform w/ Low-density

(b) Tapered w/ Low-density

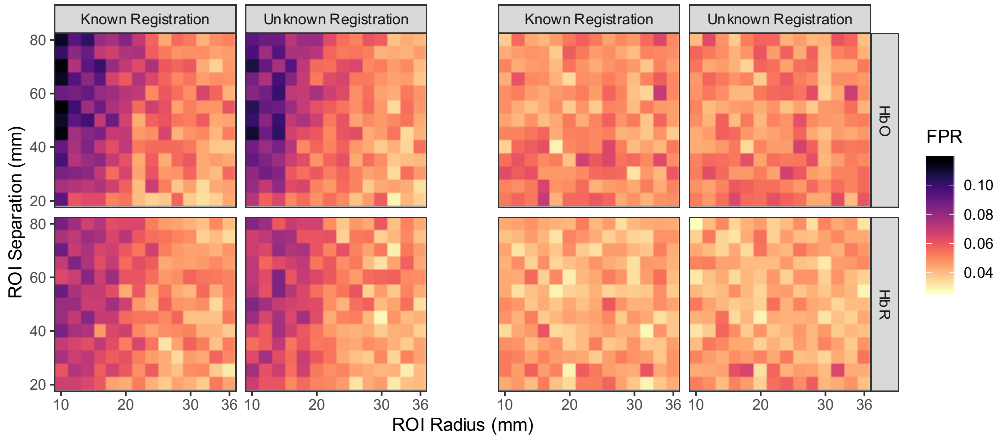
(c) Uniform w/ High-density

(d) Tapered w/ High-density

Figure 5.12: The heatmap showing the empirical FPRs of recognizing the hemoglobin activity difference between two ROIs using the two types of contrast vector for simulation data analyses under the conditions where the probe registration information is known or not. The color of each small rectangle in the lattices, whose scale is indicated by the legend, represents the FPR calculated from 2000 simulation iterations using its abscissa and ordinate as the ROI radius and separation respectively. Two types of probe, low-density (panels a and b) and high-density (panels c and d), are used in the simulations, and the left (a and c) and right (b and d) two panels contain the results using uniform contrast vector and tapered contrast vector respectively. Within each panel, the column and row of each subplot indicate known/unknown probe registration and oxy-/deoxy-hemoglobin respectively. Here 0.05 is used as the type-I error control (threshold) that is indicated by the bright color. Within each panel, the column and row of each subplot indicate known/unknown probe registration and oxy-/deoxy-hemoglobin respectively.

5.6.1 Comparison of Multiple ROIs

It can be seen from Fig. 5.10 that the two factor – ROI radius and separation jointly affect the results. The effects of channel selection, uncovered area, and blind-spot can be different with different ROI radius and separation. Generally, the channels selected for calculating contrast vectors of the two ROIs tend to be same as the two ROIs getting larger and closer, larger ROIs with a further separation are more possible to have a larger portion exceeding the probe coverage, and smaller ROIs are easier to fall into the blind-spot of the probe. The statistical power and AUC will reduce under these three conditions. We will explain the AUC changes in terms of these three effects here. Let's first look at the heatmaps of the analysis using uniform contrast vector with known registration information in the left column of panel (a). With this analysis method, the AUC increases as the two ROIs are separated by a further distance given a specific ROI radius and decreases as the radius of ROIs increases given a specific ROI separation when the registration is known. This pattern is not difficult to understand. Since the nearest four channels are used with equal weights, the contrast vectors of smaller ROIs with larger separation will have fewer shared channels and the contrast vector for their difference is further from 0 resulting in a more significant t-statistic/p-value, and vice versa. Another negative effect of large ROI is that ROIs with larger radius are easier to partially fall out of probe coverage area, especially for further separated ROIs, as they are more likely to be close to the edge of the probe, which reduces the statistical power when stimulus exists within the ROI. These are the reasons that the AUCs are larger for the small-radius-large-separation condition. For the condition using uniform contrast vector without knowing the registration in the right column of panel (a), the AUC still increases as ROI separation increases given a specific ROI radius for the same reason, while the decreasing pattern of AUC along ROI radius does not always hold. There is an increase in AUC when the ROI radius is around 20 mm. Unlike the analysis given the registration error, here the four channels used for contrast vector generation are selected based on the Colin27 atlas with an average head-size and no registration error. The selected channels can be different from the nearest four channels in truth if there is a large enough difference in the head-size or probe registration between the subject probe and the average probe. Thus, the channel selection error is another factor affecting the analysis using this method. For a fixed probe registration difference including both effects of head-size difference and registration error, the relative registration difference for a smaller ROI will be larger than that for a larger one, which means that the possibility using wrong channels for contrast vector calculation of smaller ROIs is higher. Although the contrast vector of the difference between two larger ROIs has a negative effect in AUC (as explained for known registration condition), the possibility using wrong channels for larger ROIs is reduced. Hence, the AUC change against ROI radius for a specific ROI separation is nonmonotonic. This is the reason we see a sudden increase in AUC around ROI radius = 20 mm. The change of AUCs using tapered contrast vector is more complicated. We can see that the increasing/decreasing pattern found for uniform contrast vector analysis is only true in the upper triangle whereas an opposite pattern appears in the lower triangle of subplot (b). The effects of factors affecting the AUCs using uniform contrast vector analysis still hold for the analysis with tapered contrast vector. However, the difference between two tapered contrast vectors is further from 0 than that of the uniform contrast vectors, especially for closer and larger ROIs that are more likely to result in two exactly same uniformly weighted contrast vectors. This implies that the AUC decrease caused by contrast vector decrease is smaller than the uniform method for closer and larger ROIs (the lower triangle area). Specifically, i) larger ROIs with a given separation are more possible to have uncovered area by the probe, so the effect of decreasing this possibility dominates that of smaller contrast vector, as explained before, with the decrease in ROI separation; ii) closer ROIs with a fixed size are expected to have smaller uncovered areas by the probe, and smaller ROIs are more possible to fall into the "blind-spots", so the effect of decreasing this possibility dominates that of the uncovered and smaller contrast vector with the increase in ROI size. The increase in AUC can be consequently seen as ROI separation decrease and ROI radius increases for large ROIs with smaller separation. These are the reasons that we see an opposite pattern in the lower triangle area of the plot.

5.6.2 Effect of Probe Registration Errors

To evaluate the effect of using probe registration errors in the analysis, we compared the results of analyses with known or unknown registration errors for all simulation parameters and conditions. In the single ROI analysis, we can see from Fig. 5.7 (b) that the AUCs of both tapered and uniform methods are improved with the registration errors provided (left two subplots) comparing to the analysis without knowing the errors (right two subplots). It can also be found that the improvements of tapered contrast method are larger. We also conducted statistical tests on the significance of these improvements, from which significant p-values (smaller than 0.05) are reported for all of the improvements using tapered contrast vector but the p-values are only significant for small ROIs (radius < 30) using the uniform contrast vector. This means that no significant improvements are found for large ROIs when uniform contrast vector is used. As explained in Section 5.6.1, there is a possibility that the four channels identified without registrations are different from the nearest four channels in the truth. In the single ROI analysis, the information of registration errors can help with determining the correct four channels when using uniform contrast vector. However, the possibility of choosing wrong channels to larger ROIs is smaller comparing to smaller ROIs. This explains why the improvements for large ROIs are insignificant. For the tapered contrast vector, the registration errors can correct the calculation of the weights in the contrast vector. The contrast vectors calculated with and without registration errors can never be the same regardless the size of the ROI. Thus, the using the registration errors always significantly improves the ROC performance of the tapered contrast vector. In the comparison of two ROIs, the analyses using the registration errors also improve the AUCs comparing to those without the errors. We performed similar statistical testing between the AUCs with and without knowing the registration errors. However, only about 30% of the tests report significant p-values for both uniform and tapered contrast vectors, and the appearance of these p-values shows a random pattern, which does not make too much sense to discuss. In summary, utilizing the information of registration errors can improve the analysis performance especially cooperating with the tapered contrast vector in single ROI analysis.

5.6.3 Probe Comparison

The effects of factors affecting the AUCs of low-density probe, as explained in Section 5.6.1, still hold for the high-density probe (Fig. 5.10 (c) and (d)). For the analyses using uniform contrast vector, although we can see a similar changing pattern to the one shown in Fig. 5.10 (a), the AUCs do not that notably change as the change in ROI radius. The reason for this is that the possibility of obtaining an all-zero contrast vector high-density is rare unless the two ROIs are close enough, since much more channels are used to construct the uniform contrast vector comparing to the low-density probe. Hence, the detrimental effect of large ROIs on the contrast vector is reduced. For the tapered contrast vector, the AUC changing pattern is also similar to Fig. 5.10 (b) except that the AUC rise for large-size-small-separated ROIs is smaller. It is because the high-density probe also reduces the number and size of "blind-spots" and the possibility of small ROIs falling into "blind-spots" is smaller than that with low-density probe, i.e., the negative effect of "blind-spots" is reduced. Thus, although increasing the radius for short-separated ROIs can get rid of the effect of "blind-spots," this effect itself is smaller and so is the AUC rise.

It might be noted that the AUCs using high-density probe do not show a remarkable improvement comparing to that using low-density probe. It is because a different signal-to-noise ratio is used for high-density probe, which is indicated in the title of each panel. The signal-to-noise ratios used in the ROC simulations were chosen to generate non-trivial comparisons of the methods being tested (e.g. too high SNR and all methods converge on AUC = 1 while too low SNR and all methods approach chance levels). In practice, one is expected to see an improvement when switching to high-density probe from low-density probe for same experiments. Due to the same reason, it is impossible to conduct direct statistical testing between the performances of the two probes.

5.6.4 Robustness of the Analysis

The analyses conducted in this study demonstrate that the proposed method constructs a channel-space statistic that can be used to statistically test the non-involvement of a specific ROI and the activity difference between two ROIs during a functional task utilizing the optical forward model as the channel weights without solving the underdetermined ill-posed image reconstruction inverse model. Although the computation of the tapered contrast vector depends on many factors including the forward model approximation, wavelength, brain anatomy, etc., the differences in these factors do not remarkably change the tapered shape of the contrast vector. Moreover, we also check the difference between different forward models as well as the contrast vectors calculated using various wavelengths. The computation shows the correlations between the forward models generated via the slab approximation and using NIRFAST is 0.921, the error between which is around $1-0.921^2 = 15\%$, and the change in wavelengths between 660 nm to 890 nm only makes a 4.6% difference in the contrast vector magnitude. Thus, the computation precision using ApproxSlab forward model and 808 nm wavelength is acceptable. Introducing the complexity of forward model approximation and wavelength will not notably change the analysis results.

5.6.5 Comparison of Uniform and Tapered Weighting Methods and Overall Recommendations

Going through all the results shown above, we can conclude that the proposed tapered contrast vector performs better than the conventional uniform one. In terms of ROC performance, its AUC is significantly larger than conventional method for both single ROI analysis and two-ROI comparison regardless of ROI size, separation distance, and probe layout selection. The p-values for the difference between the AUCs are smaller than 0.05 with only one exception slight larger 0.1. For the type-I error control, both methods are generally appropriate with low-density probe in single ROI analysis, although the type-I error rates are underestimated at the commonly used threshold 0.05. However, in the comparison of two ROIs, the proposed tapered contrast vector method always appropriately estimates the type-I error while the conventional method always underestimates and sometimes overestimates the type-I error rate when the low- and high-density probe is respectively used. In conclusion, the novelly proposed tapered contrast vector is always recommended for ROI-based analysis.

5.6.6 Limitations and Future Plan

Although this work demonstrates that the proposed method is significantly better than the conventionally used method, it still has several limitations. First, in the single ROI analysis, type-I error rate is underestimated at the widely used significance level, i.e., 0.05. Although using high-density probe could be able to solve this problem, considering the small improvement space in AUC and the time and cost consumption of high-density probe, we do not think it is worth to use high-density probe in this problem. Second, the performance for the comparison of two ROIs is not good enough. There is still a large space for ROC AUC improvement. Third, the model is still based on a mis-registered probe when the registration information is unknown, and the anatomical difference between subjects is not involved.

Therefore, the next step of this work will include introducing anatomy variation and optimizing probe based on image reconstruction model considering the probe is a random factor that deviates from an optimal average probe position. It is reasonable to believe that the tapered contrast vector calculated based on the optimal probe would provide a better analysis.

6.0 Brain Space Image Reconstruction of fNIRS Using a Novel Adaptive Fused Sparse Overlapping Group Lasso Model

6.1 Introduction

Functional near-infrared spectroscopy (fNIRS) is a non-invasive brain imaging technique, which uses scalp-placed optical sensors to record changes in the optical absorption of the underlying tissue and to infer changes in blood flow and oxygenation in the brain during cognitive tasks [1]. A limited spatial localization of these changes can be made by image reconstruction using the discrete set of measurements made between optical sources and detectors. However, this is a greatly under-determined problem with typically hundreds of unknown parameters in the brain (image) space compared to the dozens of actual measurements. This problem is also ill-poised; having multiple solutions of the underlying image that would generate indistinguishable channel-space measurements [93]. Thus, the reconstruction of fNIRS data into brain-space images requires additional constraints through mathematical regularization and/or additional prior information.

There are existing and active studies on the fNIRS image reconstruction problem, which is reviewed in Section 3.3. Most of them applies the constraints using statistical models, but the anatomical prior information is rarely used.

In this work, we describe an adaptive fused sparse overlapping group lasso (a-FSOGL) regularization approach for fNIRS image reconstruction. The a-FSOGL model uses brain-space voxel grouping priors, for example from atlas-based regions-of-interest, to regularize the image reconstruction process. To make a better use of the prior information, we develop a Bayesian framework to solve this model by incorporating the prior information with appropriate statistical distributions. The framework is built based on previous studies [94, 95, 96, 97, 98] of Bayesian lasso model and its extensions. Our model extend the Bayesian lasso models a step further by combining existing models and involving more prior parameters. In this paper, we will first briefly review the principals of the optical forward and inverse models. We will then derive the a-FSOGL model and its associated statistical properties before demonstrating the approach using simulated fNIRS measurements and data. In this work, we focus on the example of a nearest-neighbor bilateral fNIRS probe over the forehead and examine the ability to infer changes in frontal and dorsolateral brain regions as defined by atlas-based Brodmann area parcellations, however, this approach is applicable to any brain space parcellation model as prior information.

6.2 Theory

6.2.1 The Optical Forward Model

The optical forward model has been described in detail in previous literature [1]. Here we only depict it briefly. In an experiment using fNIRS, a set of light sources and detectors is placed on the scalp surface. The light is emitted from each source and transmitted through the tissue at two or more wavelengths. The light spreads after it is sent into the brain due to the scattering property of the tissue. The propagation path of light through brain tissue depends on its anatomical structure, including scalp, skull, cerebral spinal fluid (CSF), gray/white matter, etc., which can be approximated by a diffusion-based random walk of the photons of light and modeled through Monte Carlo, finite difference, finite element, or boundary element methods. During brain activity, the fluctuation of the blood flow in the cerebral cortex leads to the alteration of the hemoglobin concentration and consequently changes the light absorption ability of the brain tissue. The optical forward model describes the relationship between the optical density changes recorded by light source-detector pairs on the surface and the hemoglobin concentration changes in the underlying tissue. For a typical amount of hemoglobin concentration change, the change in the optical density at a given wavelength l can be modeled by the modified Beer-Lambert law as Eq. 6.1.

$$\Delta OD_{i,j}^{l} = \mathbf{X}_{i,j}^{l}\left[\varepsilon_{\mathrm{HbO}}^{l}\left(\boldsymbol{\Delta}[\mathrm{HbO}] + \boldsymbol{\xi}_{\mathrm{HbO}}\right) + \varepsilon_{\mathrm{HbR}}^{l}\left(\boldsymbol{\Delta}[\mathrm{HbR}] + \boldsymbol{\xi}_{\mathrm{HbR}}\right)\right] + \nu_{i,j}^{l} \tag{6.1}$$

where $\mathbf{X}_{i,j}$ is the Jacobian of the optical measurement model describes the total absorption by each voxel along the traveling path of light transmitted between the source to the detector pair (i, j). ε_{HbX} is the molar extinction coefficient, $\boldsymbol{\Delta}[\text{HbX}]$ is the vector containing the hemoglobin changes, and $\boldsymbol{\xi}_{\text{HbX}}$ is the physiological noise vector, in which HbX represents HbO or HbR for oxy- and deoxy-hemoglobin respectively. $\nu_{i,j}$ is the additive measurement space noise. Note that $\mathbf{X}_{i,j}$, $\boldsymbol{\Delta}[\text{HbX}]$, and $\boldsymbol{\xi}_{\text{HbX}}$ are vectors with a length same as the number of voxels. For measurements between multiple channels (source-detector pair) at multiple wavelengths, the model can be written in a compact linear expression

$$\mathbf{y} = \mathbf{X}\left(\boldsymbol{\beta} + \boldsymbol{\xi}\right) + \boldsymbol{\nu} \tag{6.2}$$

where $\mathbf{y}$ contains the measurements between all source-detector pairs and $\boldsymbol{\beta}$ includes oxy- and deoxy-hemoglobin concentration changes at each voxel in the brain image.

$$\mathbf{y} = \begin{bmatrix} \Delta OD_{i,j}^{l_1} \\ \Delta OD_{i,j}^{l_2} \\ \vdots \end{bmatrix} \text{ and } \boldsymbol{\beta} = \begin{bmatrix} \boldsymbol{\Delta}[\text{HbO}] \\ \boldsymbol{\Delta}[\text{HbO}] \end{bmatrix} \tag{6.3}$$

Thus, $\mathbf{y}$ and $\boldsymbol{\nu}$ are the measurement and measurement-space noise vector, respectively, having a length of N, which equals to the number of source-detector pairs times the number of wavelengths. $\boldsymbol{\beta}$ and $\boldsymbol{\xi}$ are two vectors containing the parameters of interest – the hemoglobin concentration changes – and the physiological noise at each voxel, respectively, so both of them have a length of P, which equals to the double of the total number of voxels (HbO and HbR for each voxel). $\mathbf{X}$ is a $N \times P$ matrix whose each row contains the Jacobian for a channel.

6.2.2 The Inverse Problem of fNIRS Image Reconstruction

The fNIRS brain image is obtained by solving Eq. 6.2, which is a high-dimensional, underdetermined, and ill-posed ($P \gg N$) inverse problem since we usually have hemoglobin changes at thousands of voxels to estimate but only tens of measurements available, i.e., the number of unkonwns is extremely greater than that of the knowns, and there exist multiple equivalent solutions. Regularization approaches are commonly used for stabilizing the solution of the inverse problem by minimizing an objective function including an additional penalty terms to the least-squares cost function, which can be represented by Eq. 6.4.

$$\widehat{\boldsymbol{\beta}} = \arg\min_{\boldsymbol{\beta}} \|\mathbf{y} - \mathbf{X}\boldsymbol{\beta}\|^2_{\mathbf{C}_{\boldsymbol{\nu}}^{-1}} + \lambda \mathcal{J}(\boldsymbol{\beta}) \tag{6.4}$$

where $\lambda \geq 0$ is a tuning parameter adjusting the weight of the regularization. $\|\mathbf{y} - \mathbf{X}\boldsymbol{\beta}\|^2_{\mathbf{C}_{\boldsymbol{\nu}}^{-1}}$ is the least-squares cost function, in which $\mathbf{C}_{\boldsymbol{\nu}}$ is the covariance matrix of the channel space error $\boldsymbol{\nu}$ and $\|\mathbf{A}\|_{\mathbf{B}} = \sqrt{\mathbf{A}^{\mathrm{T}}\mathbf{B}\mathbf{A}}$ denotes the weighted ℓ_2 norm calculation. $\mathcal{J}(\boldsymbol{\beta})$ is the penalty term applying the constraints on the sparsity and/or structure to the estimation of $\boldsymbol{\beta}$, which allows to incorporate prior information about the elements in $\boldsymbol{\beta}$. Some commonly used penalties terms are shown in Table 6.1.

6.2.3 Prior Information on Cerebral Anatomy and Hemodynamics

In an evoked-task study, the observable brain activity usually only appears within a certain area. The location of the active region depends on the type of the task, e.g., Broca's area is evoked in most speech- or language-related tasks [105, 106, 107], and voluntary movement- or control-involved tasks often activate the motor cortex area [108, 109]. Thus, for a specific task, one can have the prior information on the potential areas-of-interest and the anatomical divisions, for example, the movement of different parts of the body can be mapped to the motor cortex according to the motor homunculus [110, 111].

Brain activity leads to a growth in blood flow and oxygen consumption. The growth in blood flow increases the blood volume, brings more HbO, and moves more HbR away, while the growth in oxygen consumption results in an increase in the concentration of HbR and a decrease in that of HbO. The two effects jointly increase the concentration of HbO and decrease that of HbR during the brain activity. It is also known that the change in the HbR concentration is smaller than that in the HbO concentration.

Table 6.1: Summary of commonly used penalties terms for regularization approaches and their properties

Penalty	$\mathcal{J}(\boldsymbol{\beta})$	Property
Lasso [99]	$\|\boldsymbol{\beta}\|_1$ where $\|\boldsymbol{\beta}\|_1 = \sum_{p=1}^{P} \left|\beta_p\right|$ denoting the ℓ_1 norm $\beta_p \in \boldsymbol{\beta}$	Shrink some parameters to exact 0; proper for sparse solution space; no analytical solution
Tikhonov [100]	$\|\boldsymbol{\beta}\|^2_{\mathbf{C}_{\boldsymbol{\beta}}^{-1}}$ where $\mathbf{C}_{\boldsymbol{\beta}}$ is the covariance matrix of $\boldsymbol{\beta}$ coefficients	Cannot shrink parameters to exact 0; have a unique analytical solution for a given tuning parameter; easy to interpose covariance of $\boldsymbol{\beta}$
Elastic net [101]	$\gamma\|\boldsymbol{\beta}\|_1 + (1-\gamma)\|\boldsymbol{\beta}\|^2_{\mathbf{C}_{\boldsymbol{\beta}}^{-1}}$ where $\gamma \in [0,1]$	A weighted combination of lasso and Tikhonov regularization
Fused lasso [102]	$\gamma\|\boldsymbol{\beta}\|_1 + (1-\gamma)\|\mathbf{D}\boldsymbol{\beta}\|_1$ where $\mathbf{D}$ encodes the spatial structure	Shrink the difference between neighboring elements in $\boldsymbol{\beta}$ to 0, i.e., constraining them to be equal, in addition to the lasso penalty
Group lasso [103]	$\sum_{g=1}^{G} \sqrt{p_g} \left\|\boldsymbol{\beta}_g\right\|_{\mathbf{C}_{\boldsymbol{\beta}_g}^{-1}}$ where $\boldsymbol{\beta}$ is split into G groups, $\boldsymbol{\beta}_g$ contains the elements in the g-th group, and $\mathbf{C}_{\boldsymbol{\beta}_g}$ is the covariance matrx of $\boldsymbol{\beta}_g$	The penalty is intermediate between lasso and Thkhonov; perform variable selection at the group level
Sparse group lasso [104]	$\gamma\|\boldsymbol{\beta}\|_1 + (1-\gamma)\sum_{g=1}^{G} \sqrt{p_g} \left\|\boldsymbol{\beta}_g\right\|_{\mathbf{C}_{\boldsymbol{\beta}_g}^{-1}}$	A weighted combination of lasso and group lasso; perform variable selection at both individual and group level

6.3 Methods

In this paper, we apply an adaptive fused sparse overlapping group lasso (a-FSOGL) regularization to the inverse problem of fNIRS image reconstruction and validate the model via numerical simulations. This section describes the model and the Bayesian algorithm to solve the model in detail followed by the procedures of the simulation and evaluation.

6.3.1 Adaptive Fused Sparse Overlapping Group Lasso Model

The a-FSOGL model is an extension of the combination of fused and sparse group lasso, which can handle overlapping groups of $\boldsymbol{\beta}$ and allows different tuning parameters for each group. As shown in Table 1, the sparse group penalty can perform variable selection at both individual and group level. Thus, this penalty term incorporates the prior information on the potential areas-of-interest and the anatomical divisions by splitting $\boldsymbol{\beta}$ into groups, which includes/excludes each area entirely and allows some individual voxels to be excluded/included. The elements of a group of $\boldsymbol{\beta}$ correspond to the HbO and HbR concentration changes at the voxels in a division of the potential area. The covariance matrix of $\boldsymbol{\beta}$ can be used to apply the hemodynamics prior to constraining the HbO and HbR concentration changes at the same voxel to be anti-correlated. In addition, since the hemoglobin concentration changes within a group are not independent, the fused lasso penalty term is added to minimize the hemoglobin concentration changes at neighboring voxels. Previous study [112] shows that the variable selection exhibited by the lasso model is inconsistent except for a specific non-trivial condition and develops the adaptive lasso model to reach consistent variable selection by using different tuning parameter for each coefficient. For the same reason, adaptive fused lasso [113] and adaptive groups [114] have also been proposed. Similarly, here we also use the adaptive version of regularization.

It is difficult to precisely split the cortex into regions-of-interest (ROI) at the voxel level, since some voxels can potentially belong to multiple groups depending on how the atlas is defined. For example, we found the specific parcellation of Brodmann Areas for which came from the Talriarch Daemon atlas [90], which is used in the simulation study of this paper, assigns some voxels into multiple groups, especially those around and on the border between two areas, i.e., the neighboring two groups overlap to each other. Previous studies [115, 116] demonstrated that the overlapping group lasso is equivalent to a regular group lasso by duplicating the covariates belonging to multiple groups as shown in Fig. 6.1.

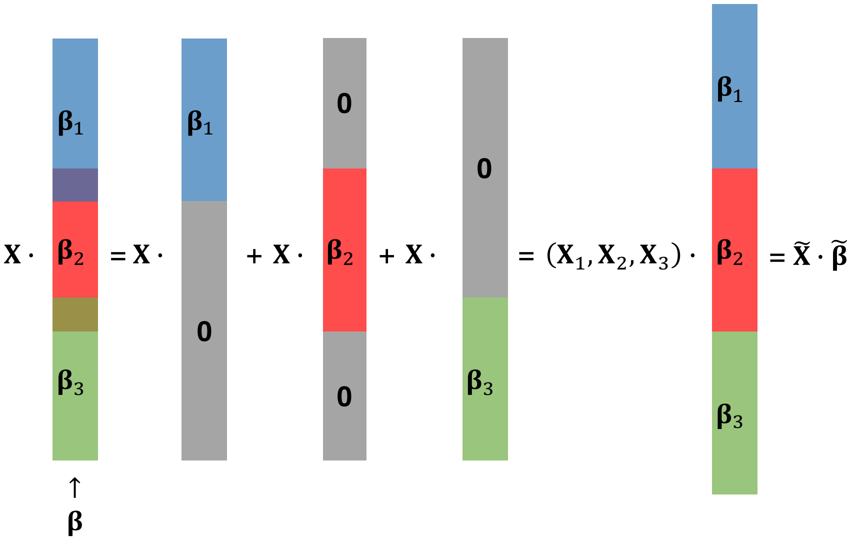

Figure 6.1: An example demonstrating the equivalence between an overlapping group lasso and a regular group lasso with duplicated covariates. $\boldsymbol{\beta}_1$, $\boldsymbol{\beta}_2$, and $\boldsymbol{\beta}_3$ are the three groups of $\boldsymbol{\beta}$ where there exist overlaps between $\boldsymbol{\beta}_1$, $\boldsymbol{\beta}_2$ and $\boldsymbol{\beta}_2$, $\boldsymbol{\beta}_3$. $\mathbf{X}_1$, $\mathbf{X}_2$ and $\mathbf{X}_3$ are the submatrix of X corresponding to $\boldsymbol{\beta}_1$, $\boldsymbol{\beta}_2$, and $\boldsymbol{\beta}_2$ respectively. $\widetilde{\mathbf{X}}$ and $\widetilde{\boldsymbol{\beta}}$ are the constructed by concatenating $\mathbf{X}_1$, $\mathbf{X}_2$, $\mathbf{X}_3$ and $\boldsymbol{\beta}_1$, $\boldsymbol{\beta}_2$, $\boldsymbol{\beta}_3$ with duplicating the overlapping parts, respectively.

From previous studies [34, 33], we can obtain the covariance matrix of the measurements error, $\mathbf{C}_{\boldsymbol{\nu}}$, from the channel space analysis of the given fNIRS dataset. To reduce the number of optimization parameters in the model, the correlation of the error term can be removed through whitening transformation. Let $\mathbf{W}$ denote the Cholesky decomposition of $\mathbf{C}_{\boldsymbol{\nu}}^{-1}$, i.e., $\mathbf{W}^{\mathrm{T}}\mathbf{W} = \mathbf{C}_{\boldsymbol{\nu}}^{-1}$. $\mathbf{X}$ and $\mathbf{y}$ can be transformed via $\mathbf{X}^{*} = \mathbf{W}\mathbf{X}$ and $\mathbf{y}^{*} = \mathbf{W}\mathbf{y}$. The optimization problem using the transformed variables is equivalent to the original one involving the covariance matrix. To maintain conciseness of the notation, $\mathbf{X}$, $\mathbf{y}$, and $\boldsymbol{\beta}$ will represent the expanded and decorrelated variables, $\widetilde{\mathbf{X}}^{*}$, $\mathbf{y}^{*}$, and $\widetilde{\boldsymbol{\beta}}$ in the remaining part of this paper.

The a-FSOGL is proposed to estimate $\boldsymbol{\beta}$ by minimizing the cost function shown in Eq. 6.5.

$$\widehat{\boldsymbol{\beta}} = \arg\min_{\boldsymbol{\beta}} \left\{ \|\mathbf{y} - \mathbf{X}\boldsymbol{\beta}\|^2 + \sum_{g=1}^{G} \lambda_g \left[\theta\gamma \left\|\boldsymbol{\beta}_g\right\|_1 + (1-\gamma)\left\|\mathbf{D}_g\boldsymbol{\beta}_g\right\|_1 + (1-\theta)\gamma \left\|\boldsymbol{\beta}_g\right\|_{\mathbf{C}^{-1}_{\boldsymbol{\beta}_g}} \right] \right\} \tag{6.5}$$

Here $\lambda_g \geq 0$ is the tuning parameter for the g-th group controlling the overall level of regularization, and $\theta, \gamma \in [0,1]$ are the two parameters jointly define the weights of the three penalty terms [117]. When θ or $\gamma = 0$ or 1 , some penalty terms are dropped and the minimization degenerates into a subset of a-FSOGL. For example, when $\theta = 1$ and $\gamma = 1$, the model reduces to a standard adaptive lasso, etc. Let m_g denote the number of elements in $\boldsymbol{\beta}_g$ and q_g denote the number of connected voxel pairs in $\boldsymbol{\beta}_g$. Note that m_g equals double of the number of voxels (HbO and HbR for each voxel in the group, and $\sum_{g=1}^{G} m_g = P$. Then $\mathbf{D}_g$ is a $q_g \times m_g$ matrix encoding the spatial structure of $\boldsymbol{\beta}_g$. A simple example of $\mathbf{D}_g$ is shown in Fig. 6.2.

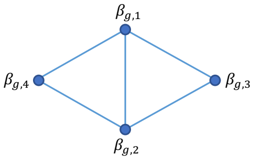

$$\longrightarrow \mathbf{D}_g = \begin{bmatrix} 1 & -1 & 0 & 0 \\ 1 & 0 & -1 & 0 \\ 1 & 0 & 0 & -1 \\ 0 & 1 & -1 & 0 \\ 0 & 1 & 0 & -1 \end{bmatrix} \longrightarrow \begin{cases} \mathbf{D}_g\boldsymbol{\beta}_g = [\beta_{g,1}-\beta_{g,2} \quad \beta_{g,1}-\beta_{g,3} \quad \beta_{g,1}-\beta_{g,4} \quad \beta_{g,2}-\beta_{g,3} \quad \beta_{g,2}-\beta_{g,4}]^{\mathrm{T}} \\ \|\mathbf{D}_g\boldsymbol{\beta}_g\|_1 = |\beta_{g,1}-\beta_{g,2}| + |\beta_{g,1}-\beta_{g,3}| + |\beta_{g,1}-\beta_{g,4}| + |\beta_{g,2}-\beta_{g,3}| + |\beta_{g,2}-\beta_{g,4}| \end{cases}$$

Figure 6.2: A simple example of $\mathbf{D}_g$. The left diagram shows the structure of $\boldsymbol{\beta}_g$ where there are four elements (represented by the solid circles) and five connected pairs (connections represented by the solid lines). Thus, $\mathbf{D}_g$ is a 5×4 matrix, in which each row represents a connected pair by assigning 1 and -1 to the columns corresponding to the indices of the two elements of the pair and 0 to the remaining columns. Finally, $\left\|\mathbf{D}\boldsymbol{\beta}_g\right\|_1$ provides the summation of the absolute differences between βs of each paired connection in the spatial structure.

Note that in this paper we arrange the HbO changes as the first $\frac{m_g}{2}$ elements of $\boldsymbol{\beta}_g$ and the HbR changes as the second half elements. $\mathbf{D}_g$ can be decomposed into four $\frac{q_g}{2} \times \frac{m_g}{2}$ submatices. The two submatrices on the diagonal are identical, and each of them represents the spatial structure of the voxels. The two off-diagonal submatrices are both zero matrix as HbO and HbR changes are not expected to be equal.

6.3.1.1 Bayesian Hierarchical Modeling and Prior Distributions

The number of parameters need to be optimized in a-FSOGL is usually more than 1,000 including $\boldsymbol{\beta}_g$ and its covariance matrix. Searching in such a high-dimensional solution space and maintaining the semipositive definiteness of the covariance matrix are challenging using the conventional gradient-based minimization algorithms. In this subsection, we propose the hierarchical Bayesian a-FSOGL (Ba-FSOGL) based on the contributions of previous studies [94, 95, 97, 98] and extend it to handle correlated coefficients by involving the covariance matrix.

Similar to previous studies [94], the conditional prior of $\boldsymbol{\beta}$ for the model in Eq.6.5 can be written as Eq. 6.6.

$$\pi\left(\boldsymbol{\beta} \mid \sigma^2, \mathbf{C}_{\boldsymbol{\beta}_g}, \mathbf{D}_g\right) \propto \exp\left\{-\frac{1}{\sigma}\sum_{g=1}^{G}\lambda_g\left[\theta\gamma\left\|\boldsymbol{\beta}_g\right\|_1 + (1-\gamma)\left\|\mathbf{D}_g\boldsymbol{\beta}_g\right\|_1 + (1-\theta)\gamma\left\|\boldsymbol{\beta}_g\right\|_{\mathbf{C}^{-1}_{\boldsymbol{\beta}_g}}\right]\right\} \tag{6.6}$$

We introduce the hierarchical model with the latent parameters:

$$\mathbf{y} \mid \mathbf{X}, \boldsymbol{\beta}, \sigma^2 \sim \mathcal{N}_N\left(\mathbf{X}\boldsymbol{\beta}, \sigma^2\mathbf{I}\right) \tag{6.7}$$

where $\mathcal{N}_n(\boldsymbol{\mu}, \boldsymbol{\Sigma})$ denotes a n-dimensional multivariate normal distribution with a mean vector $\boldsymbol{\mu}$ and a covariance matrix Σ, and σ^2 is the noise variance in the measurement space. For the g-th group, we introduce the prior distribution of $\boldsymbol{\beta}_g$ as follows.

$$\boldsymbol{\beta}_g \mid \mathbf{X}, \boldsymbol{\Sigma}_g, \sigma^2 \sim \mathcal{N}_{m_g}\left(\mathbf{0}, \sigma^2\boldsymbol{\Sigma}_g\right) \tag{6.8}$$

The inverse of the covariance matrix $\boldsymbol{\Sigma}_g$ should have the following structure reflecting the constrains from the three penalty terms in the model from Eq. 6.5.

$$\boldsymbol{\Sigma}_g = \left[\boldsymbol{\Psi}_g^{-1} + \mathbf{D}_g^{\mathrm{T}}\boldsymbol{\Phi}_g^{-1}\mathbf{D}_g + \left(\tau_g^2\mathbf{C}_{\boldsymbol{\beta}_g}\right)^{-1}\right]^{-1} \tag{6.9}$$

The $\mathbf{\Psi}_g$ matrix defines the variance of each element of $\boldsymbol{\beta}_g$, which allows variable selection at individual level with the following structure.

$$\mathbf{\Psi}_g = \begin{bmatrix} \psi_{g,1}^2 & 0 & \cdots & 0 \\ 0 & \psi_{g,2}^2 & \ddots & 0 \\ \vdots & \ddots & \ddots & \vdots \\ 0 & 0 & \cdots & \psi_{g,m_g}^2 \end{bmatrix} \tag{6.10}$$

The matrix $\mathbf{D}_g^{\mathrm{T}}\mathbf{\Phi}_g^{-1}\mathbf{D}_g$ incorporates the effect of fused lasso into the model where

$$\mathbf{\Phi}_g = \begin{bmatrix} \phi_{g,1}^2 & 0 & \cdots & 0 \\ 0 & \phi_{g,2}^2 & \ddots & 0 \\ \vdots & \ddots & \ddots & \vdots \\ 0 & 0 & \cdots & \phi_{g,q_g}^2 \end{bmatrix} \tag{6.11}$$

The matrix $\tau_g^2\mathbf{C}_{\boldsymbol{\beta}_g}$ holds the group level variable selection where τ_g^2 is the common variance term of $\boldsymbol{\beta}_g$ and $\mathbf{C}_{\boldsymbol{\beta}_g}$ is a semi-positive definite matrix constraining the relationship between the elements among $\boldsymbol{\beta}_g$. In the case of fNIRS image reconstruction, the first half elements of $\boldsymbol{\beta}_g$ represents the HbO and the other half represents the HbR changes within a region. Hence, considering the common variance has been determined by τ_g^2, $\mathbf{C}_{\boldsymbol{\beta}_g}$ only needs to reflect the anti-correlation between HbO and HbR changes as well as the fraction of HbR changes to HbO changes. Thus, we define $\mathbf{C}_{\boldsymbol{\beta}_g}$ as a $m_g \times m_g$ matrix.

$$\begin{gathered} \mathbf{C}_{\boldsymbol{\beta} g} = \begin{bmatrix} 1 & \rho_g\zeta_g \\ \rho_g\zeta_g & \zeta_g^2 \end{bmatrix} \otimes \mathbf{I}_{m_g/2} \\ \rho_g \sim \mathcal{U}(-1,0) \text{ and } \zeta_g \sim \mathcal{U}(0,1) \end{gathered} \tag{6.12}$$

where $\otimes$ stands for Kronecker product and $\mathcal{U}(a,b)$ denotes a uniform distribution between $[a,b]$. The $-1 \leq \rho_g \leq 0$ ensures the negative correlation between HbO and HbR changes, and $0 \leq \zeta_g \leq 1$ maintains the amplitude of the HbR change is smaller than that of HbO change at the same voxel.

We place the following multivariate prior in Eq. 6.13 on $\mathbf{\Sigma}_g$ $(\psi_{g,1}^2, \cdots \psi_{g,m_g}^2, \phi_{g,1}^2, \cdots \phi_{g,q_g}^2 \tau_g^2)$ to achieve the expected form of marginal posterior $\pi\left(\boldsymbol{\beta} \mid \sigma^2, \mathbf{C}_{\boldsymbol{\beta}_g}, \mathbf{D}_g\right)$.

$$
\begin{aligned}
\pi\left(\boldsymbol{\Sigma}_g\right) =& \pi\left(\psi_{g,1}^2, \cdots \psi_{g,m_g}^2, \phi_{g,1}^2, \cdots \phi_{g,q_g}^2 \tau_g^2\right)\\
=& \,\text{constant} \cdot \det\left(\boldsymbol{\Sigma}_g\right)^{\frac{1}{2}}\\
& \cdot \prod_{p=1}^{m_g}\left[\left(\psi_{g,p}^2\right)^{-\frac{1}{2}} \frac{\left(\lambda_g\theta\gamma\right)^2}{2} \exp\left(-\frac{\left(\lambda_g\theta\gamma\right)^2 \psi_{g,p}^2}{2}\right)\right]\\
& \cdot \prod_{k=1}^{q_g}\left[\left(\phi_{g,k}^2\right)^{-\frac{1}{2}\frac{\left(\lambda_g(1-\gamma)\right)^2}{2}} \exp\left(-\frac{\left(\lambda_g(1-\gamma)\right)^2 \phi_{g,k}^2}{2}\right)\right]\\
& \cdot \left(\tau_g^2\right)^{-\frac{1}{2}} \frac{\left(\lambda_g(1-\theta)\gamma\right)^2}{2} \exp\left(-\frac{\left(\lambda_g(1-\theta)\gamma\right)^2 \tau_g^2}{2}\right) \qquad (6.13)
\end{aligned}
$$

For each $g = 1, \ldots, G$, similar to Eq. (16) in [94], the marginal distribution of $\boldsymbol{\beta}_g$ can be derived by Eq. 6.14 . The number below the ellipsis in Eq. 6.14 denotes the number of integral operators omitted.

$$
\begin{aligned}
& \int_0^{+\infty} \underbrace{\cdots\cdots}_{m_g-1} \int_0^{+\infty} \underbrace{\cdots\cdots}_{q_g-1} \int_0^{+\infty} \pi\left(\boldsymbol{\beta}_g \mid \mathbf{X}, \boldsymbol{\Sigma}_g, \sigma^2\right) \pi\left(\boldsymbol{\Sigma}_g\right) \cdot \prod_{p=1}^{m_g} \mathrm{d}\psi_{g,p}^2 \prod_{k=1}^{q_g} \mathrm{d}\phi_{g,k}^2 \, \mathrm{d}\tau_g^2\\
\propto & \int_0^{+\infty} \underbrace{\cdots\cdots}_{m_g-1} \int_0^{+\infty} \underbrace{\cdots\cdots}_{q_g-1} \int_0^{+\infty} \left\{\begin{array}{l}
\det\left(\boldsymbol{\Sigma}_g\right)^{\frac{1}{2}} \prod_{p=1}^{m_g}\left[\left(\psi_{g,p}^2\right)^{-\frac{1}{2}} \frac{\left(\lambda_g\theta\gamma\right)^2}{2} \exp\left(-\frac{\left(\lambda_g\theta\gamma\right)^2 \psi_{g,p}^2}{2}\right)\right]\\
\cdot \prod_{k=1}^{q_g}\left[\left(\phi_{g,k}^2\right)^{-\frac{1}{2}} \frac{\left(\lambda_g(1-\gamma)\right)^2}{2} \exp\left(-\frac{\left(\lambda_g(1-\gamma)\right)^2 \phi_{g,k}^2}{2}\right)\right]\\
\cdot \left(\tau_g^2\right)^{-\frac{1}{2}\frac{\left(\lambda_g(1-\theta)\gamma\right)^2}{2}} \exp\left(-\frac{\left(\lambda_g(1-\theta)\gamma\right)^2 \tau_g^2}{2}\right)\\
\cdot \prod_{p=1}^{m_g} \mathrm{d}\psi_{g,p}^2 \prod_{k=1}^{q_g} \mathrm{d}\phi_{g,k}^2 \mathrm{d}\tau_g^2
\end{array}\right\}\\
\propto & \int_0^{+\infty} \underbrace{\cdots\cdots}_{m_g-2} \int_0^{+\infty} \exp\left(-\frac{\boldsymbol{\beta}_g^{\mathrm{T}} \boldsymbol{\Psi}_g^{-1} \boldsymbol{\beta}_g}{2\sigma^2}\right) \prod_{p=1}^{m_g}\left(\psi_{g,p}^2\right)^{-\frac{1}{2}} \frac{\left(\lambda_g\theta\gamma\right)^2}{2} \exp\left(-\frac{\left(\lambda_g\theta\gamma\right)^2 \psi_{g,p}^2}{2}\right) \mathrm{d}\psi_{g,p}^2\\
& \cdot \int_0^{+\infty} \underbrace{\cdots\cdots}_{q_g-2} \int_0^{+\infty} \exp\left(-\frac{\boldsymbol{\beta}_g^{\mathrm{T}} \mathbf{D}_g^{\mathrm{T}} \boldsymbol{\Phi}_g^{-1} \mathbf{D}_g \boldsymbol{\beta}_g}{2\sigma^2}\right) \prod_{k=1}^{q_g}\left\{\begin{array}{l}
\left(\phi_{g,k}^2\right)^{-\frac{1}{2}} \frac{\left(\lambda_g(1-\gamma)\right)^2}{2}\\
\cdot \exp\left(-\frac{\left(\lambda_g(1-\gamma)\right)^2 \phi_{g,k}^2}{2}\right) \mathrm{d}\phi_{g,k}^2
\end{array}\right\}\\
& \cdot \int_0^{+\infty} \exp\left(-\frac{\boldsymbol{\beta}_g^{\mathrm{T}} \mathbf{C}_{\boldsymbol{\beta}}^{-1} \boldsymbol{\beta}_g}{2\sigma^2\tau_g^2}\right) \left(\tau_g^2\right)^{-\frac{1}{2}} \frac{\left(\lambda_g(1-\theta)\gamma\right)^2}{2} \exp\left(-\frac{\left(\lambda_g(1-\theta)\gamma\right)^2 \tau_g^2}{2}\right) \mathrm{d}\tau_g^2
\end{aligned}
$$

$$\propto \exp\left\{-\frac{\lambda_g}{\sigma}\left[\theta\gamma\left\|\boldsymbol{\beta}_g\right\|_1+(1-\gamma)\left\|\mathbf{D}_g\boldsymbol{\beta}_g\right\|_1+(1-\theta)\gamma\left\|\boldsymbol{\beta}_g\right\|_{\mathbf{C}^{-1}_{\boldsymbol{\beta}_g}}\right]\right\} \tag{6.14}$$

where $\pi\left(\boldsymbol{\beta}_g \mid \mathbf{X}, \boldsymbol{\Sigma}_g, \sigma^2\right)$ is the probability density function of the prior distribution of $\boldsymbol{\beta}_g$ defined by Eq. 6.8. The last step of Eq. 6.14 is based on Eq. 6.15, which demonstrates the double-exponential (Laplace) distribution is a scale mixture of a Gaussian distribution with an exponential density.

$$\frac{a}{2}\exp(-a|z|)=\int_0^\infty \frac{1}{\sqrt{2\pi t}}\exp\left(-\frac{z^2}{2t}\right)\frac{a^2}{2}\exp\left(-\frac{a^2}{2}t\right)\mathrm{d}t \tag{6.15}$$

The conditional prior can be calculated by the product of Eq. 6.14 for $g = 1$ through G given by Eq. 6.16, which satisfies the conditional prior of $\boldsymbol{\beta}_g$ anticipated in Eq. 6.6.

$$\begin{aligned}&\prod_{g=1}^{G}\text{constant }\cdot\exp\left\{\frac{\lambda_g}{\sigma}\left[\theta\gamma\left\|\boldsymbol{\beta}_g\right\|_1+(1-\gamma)\left\|\mathbf{D}_g\boldsymbol{\beta}_g\right\|_1+(1-\theta)\gamma\left\|\boldsymbol{\beta}_g\right\|_{\mathbf{C}^{-1}_{\boldsymbol{\beta}}}\right]\right\}\\ &=\text{constant }\cdot\exp\left\{\frac{1}{\sigma}\sum_{g=1}^{G}\lambda_g\left[\theta\gamma\left\|\boldsymbol{\beta}_g\right\|_1+(1-\gamma)\left\|\mathbf{D}_g\boldsymbol{\beta}_g\right\|_1+(1-\theta)\gamma\left\|\boldsymbol{\beta}_g\right\|_{\mathbf{C}^{-1}_{\boldsymbol{\beta}}}\right]\right\}\end{aligned} \tag{6.16}$$

6.3.1.2 Gibbs Sampling from Full Conditional Distributions With the hierarchical model described in Section 6.3.1.1, $\boldsymbol{\beta}_g$ can be estimated using its empirical posterior distribution obtained by Gibbs sampling, which requires the full conditional distribution – the posterior distribution depending on all remaining parameters – of every model parameter. This section will show the steps for calculating the full conditional distributions.

Similar to previous studies, we can interpose an inverse gamma (ig) hyperprior for σ^2 in addition to the prior distributions given in Section 6.3.1.1 defined in Eq. 6.17.

$$\sigma^2 \sim \mathit{ig}(r, s) \tag{6.17}$$

where r and s are the shape and scale hyperparameter of inverse gamma distribution. The joint posterior probability density function (PDF) of $\boldsymbol{\beta}$, $\boldsymbol{\Psi}^2$, $\boldsymbol{\Phi}^2$, τ^2, ρ, ζ given $\mathbf{X}$, $\mathbf{y}$ is shown in Eq. 6.18.

$$
\begin{aligned}
&\pi\left(\boldsymbol{\beta}, \psi^2, \phi^2, \tau^2, \rho, \zeta \mid \mathbf{X}, \mathbf{y}\right) \\
\propto &\pi\left(\mathbf{y} \mid \mathbf{X}, \boldsymbol{\beta}, \sigma^2\right) \pi\left(\sigma^2\right) \\
&\cdot \prod_{g=1}^{G}\left[\pi\left(\boldsymbol{\beta}_g \mid \mathbf{X}, \boldsymbol{\Sigma}_g, \sigma^2\right) \pi\left(\psi_{g,1}^2 \cdots \psi_{g,m_g}^2, \phi_{g,1}^2, \cdots \phi_{g,q_g}^2 \tau_g^2\right) \pi\left(\zeta_g\right) \pi\left(\rho_g\right)\right] \\
\propto &\left(2\pi\sigma^2\right)^{-\frac{N}{2}} \exp\left[-\frac{(\mathbf{y}-\mathbf{X}\boldsymbol{\beta})^{\mathrm{T}}(\mathbf{y}-\mathbf{X}\boldsymbol{\beta})}{2\sigma^2}\right] \cdot \frac{s^r\left(\sigma^2\right)^{-r-1}}{\Gamma(r)} \exp\left(-\frac{s}{\sigma^2}\right) \\
&\cdot \prod_{g=1}^{G}\Bigg\{\left(2\pi\sigma^2\right)^{\frac{m_g}{2}} \det\left(\boldsymbol{\Sigma}_g\right)^{-\frac{1}{2}} \cdot \exp\left[-\frac{1}{2\sigma^2}\boldsymbol{\beta}_g^{\mathrm{T}}\boldsymbol{\Sigma}_g^{-1}\boldsymbol{\beta}_g\right] \cdot \det\left(\boldsymbol{\Sigma}_g\right)^{\frac{1}{2}} \\
&\cdot \prod_{p=1}^{m_g}\left[\left(\psi_{g,p}^2\right)^{-\frac{1}{2}} \frac{\left(\lambda_g\theta\gamma\right)^2}{2} \exp\left(-\frac{\left(\lambda_g\theta\gamma\right)^2 \psi_{g,p}^2}{2}\right)\right] \\
&\cdot \prod_{k=1}^{q_g}\left[\left(\phi_{g,k}^2\right)^{-\frac{1}{2}} \frac{\left(\lambda_g(1-\gamma)\right)^2}{2} \exp\left(-\frac{\left(\lambda_g(1-\gamma)\right)^2 \phi_{g,k}^2}{2}\right)\right] \\
&\cdot \left(\tau_g^2\right)^{-\frac{1}{2}} \frac{\left(\lambda_g(1-\theta)\gamma\right)^2}{2} \exp\left(-\frac{\left(\lambda_g(1-\theta)\gamma\right)^2 \tau_g^2}{2}\right) \cdot 1 \cdot 1 \Bigg\}
\end{aligned}
\tag{6.18}
$$

Let $\mathbf{A}_g = \mathbf{X}_g^{\mathrm{T}}\mathbf{X}_g + \boldsymbol{\Sigma}_g^{-1}$ where $\mathbf{X}_g$ is a submatrix of $\mathbf{X}$ containing the columns corresponding to $\boldsymbol{\beta}_g$. The terms involving $\boldsymbol{\beta}_g$ can be written as Eq. 6.19, which is proportional to the PDF of a multivariate normal distribution.

$$
\exp\left\{-\frac{1}{2\sigma^2}\left[\boldsymbol{\beta}_g - \mathbf{A}_g^{-1}\mathbf{X}_g^{\mathrm{T}}\left(\mathbf{y} - \sum_{g'\neq g}\mathbf{X}_{g'}\boldsymbol{\beta}_{g'}\right)\right]^{\mathrm{T}} \mathbf{A}_g \left[\boldsymbol{\beta}_g - \mathbf{A}_g^{-1}\mathbf{X}_g^{\mathrm{T}}\left(\mathbf{y} - \sum_{g'\neq g}\mathbf{X}_{g'}\boldsymbol{\beta}_{g'}\right)\right]\right\}
\tag{6.19}
$$

The full conditional posterior of $\boldsymbol{\beta}_g$ is therefore

$$
\boldsymbol{\beta}_g \mid \text{rest} \sim \mathcal{N}_{m_g}\left(\mathbf{A}_g^{-1}\mathbf{X}_g^{\mathrm{T}}\left(\mathbf{y} - \sum_{g'\neq g}\mathbf{X}_{g'}\boldsymbol{\beta}_{g'}\right), \sigma^2\mathbf{A}_g^{-1}\right)
\tag{6.20}
$$

where rest represents all the remaining parameters. Following similar steps, we can derive the full conditional posterior of the other parameters shown as follows.

$$\frac{1}{\psi_{g,p}^{2}} \mid \text{rest} \overset{\text{ind.}}{\sim} \boldsymbol{i\mathcal{G}} \left(\sqrt{\frac{\left(\lambda_g \theta \gamma\right)^2 \sigma^{2}{}^{2}}{\beta_{g,p}}}, \left(\lambda_g \theta \gamma\right)^2 \right) \quad \text{for } g = 1 \ldots G; p = 1 \ldots m_g \tag{6.21}$$

$$\frac{1}{\phi_{g,k}^{2}} \mid \text{rest} \overset{\text{ind.}}{\sim} \boldsymbol{i\mathcal{G}} \left(\sqrt{\frac{\left(\lambda_g (1-\gamma)\right)^2 \sigma^2}{\left(\mathbf{D}_g \boldsymbol{\beta}_g\right)_k^2}}, \left(\lambda_g (1-\gamma)\right)^2 \right) \quad \text{for } g = 1 \ldots G; k = 1 \ldots q_g \tag{6.22}$$

$$\frac{1}{\tau_g^2} \mid \text{rest} \overset{\text{ind.}}{\sim} \boldsymbol{i\mathcal{G}} \left(\sqrt{\frac{\left(\lambda_g (1-\theta)\gamma\right)^2 \sigma^2}{\left\|\boldsymbol{\beta}_g\right\|_{\mathbf{C}_{\boldsymbol{\beta}_g}^{-1}}^2}}, \left(\lambda_g (1-\theta)\gamma\right)^2 \right) \quad \text{for } g = 1 \ldots G \tag{6.23}$$

$$\sigma^2 \mid \text{rest} \sim \boldsymbol{ig} \left(\frac{N-1+P}{2} + r, \frac{1}{2}\|\mathbf{y} - \mathbf{X}\boldsymbol{\beta}\|^2 + \frac{1}{2}\sum_{g=1}^{G} \left\|\boldsymbol{\beta}_g\right\|_{\boldsymbol{\Sigma}_g^{-1}}^2 + s \right) \tag{6.24}$$

where $\boldsymbol{i\mathcal{G}}(\mu, \upsilon)$ denotes an inverse Gaussian distribution with mean μ and scale parameters υ.

Let $\beta_{g,1}^{\text{HbO}} \ldots \beta_{g,\frac{m_g}{2}}^{\text{HbO}}$ and $\beta_{g,1}^{\text{HbR}} \ldots \beta_{g,\frac{m_g}{2}}^{\text{HbR}}$ respectively denote the HbO and HbR changes at the $\frac{m_g}{2}$ positions in the g-th group. The term involving $\mathbf{C}_{\boldsymbol{\beta}_g}$ can be expanded as Eq. 6.25

$$\begin{aligned} &\exp\left[-\frac{1}{2}\boldsymbol{\beta}_g^{\mathrm{T}} \left(\sigma^2 \tau_g^2 \mathbf{C}_{\boldsymbol{\beta}_g}\right)^{-1} \boldsymbol{\beta}_g\right] \\ =&\exp\left\{-\frac{1}{2\left(1-\rho_g^2\right)\sigma^2\tau_g^2}\left[\sum_{p=1}^{m_g/2}\left(\left(\beta_{g,p}^{\text{Hb0}}\right)^2 - \frac{2\rho_g \beta_{g,p}^{\text{Hbo}} \beta_{g,p}^{\text{HbR}}}{\zeta_g} + \frac{\left(\beta_{g,p}^{\text{HbR}}\right)^2}{\zeta_g^2}\right)\right]\right\} \end{aligned} \tag{6.25}$$

The full conditionals for ζ_g and ρ_g are respectively proportional to Eq. 6.26

$$\begin{aligned}
\pi(\zeta_g) &\propto \exp\left\{-\tfrac{1}{2\left(1-\rho_g^2\right)\sigma^2\tau_g^2}\left[\sum_{p=1}^{m_g/2}\left(-\tfrac{2\rho_g\beta_{g,m}^{\mathrm{HbO}}\beta_{g,m}^{\mathrm{HbR}}}{\zeta_g}+\tfrac{\left(\beta_{g,m}^{\mathrm{HbR}}\right)^2}{\zeta_g^2}\right)\right]\right\} \\
\pi(\rho_g) &\propto \exp\left\{-\tfrac{1}{2\left(1-\rho_g^2\right)\sigma^2\tau_g^2}\left[\sum_{p=1}^{m_g/2}\left(\left(\beta_{g,m}^{\mathrm{Hb0}}\right)^2-\tfrac{2\rho_g\beta_{g,m}^{\mathrm{Hb0}}\beta_{g,m}^{\mathrm{HbR}}}{\zeta_g}+\tfrac{\left(\beta_{g,m}^{\mathrm{HbR}}\right)^2}{\zeta_g^2}\right)\right]\right\}
\end{aligned} \tag{6.26}$$

With the full conditional distributions of the parameters in the model, one can estimate the marginal distribution of $\boldsymbol{\beta}$ using a Markov chain Monte Carlo (MCMC) method – Gibbs sampler. In each sampling iteration, every parameter is sampled from its full conditional distribution using the values of the remaining parameters sampled from the previous iteration. Note that full conditionals of ρ, ζ are not known distributions, which cannot be sampled directly. We plug in Metropolis-Hastings sampler within each Gibbs sampling iteration to obtain the samples of ρ, ζ [73]. After the sampling chain converges, $\boldsymbol{\beta}$ can be estimated by the mean or median of its samples.

6.3.1.3 Choosing the Tuning Parameters

The tuning parameter λ_g determines the level of regularization. In this study, we choose the tuning parameter using a stochastic approximation-based single-step approach proposed by previous studies [95, 118] for a given dataset $\mathbf{X}$, $\mathbf{y}$, which is a computationally economical single-step approach.

In the i-th sampling iteration of our framework, transforming the tuning parameter by $\delta_g = \log\lambda_g$, we update δ_g following the rule $\delta_g^{(i)} = \delta_g^{(i-1)} + u_j \cdot \left(\frac{\partial\mathcal{L}L}{\partial\delta_g}\right)$ where $\mathcal{LL}$ is the log-likelihood function of λ_g and $\{u_i\}$ is a positive sequence satisfying the following conditions:

1. u_i monotonically decreases and converges to 0 as i increases;
2. $\sum_{i=1}^{+\infty} u_i = \infty$;
3. $\sum_{i=1}^{+\infty} u_i^2 < \infty$

In the simulation study of this paper, u_i is set to be the terms of a scaled harmonic series $u_i = \frac{10^{-3}}{i}$. The scaling factor, 10^{-3}, determines the optimization step size selected by preliminary trials. We need to find a moderate value, with which the algorithm coverges within reasonable iterations time without diverging.

6.3.1.4 Statistical Inference In frequentist framework, statistical inference of lasso-based model is usually unnecessary since insignificant variables are forced to be zero. However, the probability to exactly hit any specific number from a continuous distribution is zero. The samples from Gibbs sampler cannot give exact zero estimates no matter how small they are. Statistical inference is required to determine the significance of variables in Bayesian framework.

Two interval-based approaches [96] are used for the inference on every individual variable, β_p, in this study. First, β_p is statistically significant if its credible interval (CI) excludes 0 and insignificant otherwise. Second, we calculate the posterior probability that β_p is within the scaled neighborhood interval $\left[-\sqrt{\operatorname{Var}\left(\beta_p \mid \mathbf{X}, \mathbf{y}\right)}, \sqrt{\operatorname{Var}\left(\beta_p \mid \mathbf{X}, \mathbf{y}\right)}\right]$. β_p is considered to be insignificant if this probability exceeds a certain threshold and significant otherwise. In addition to the inference on individual variables, we also perform statistical inference on the significance of the variables in a group, $\boldsymbol{\beta}_g$, as an entirety. The CIs of the random variable $\boldsymbol{\beta}_g^{\mathrm{T}} \boldsymbol{\Sigma}_g^{-1} \boldsymbol{\beta}_g$ for all groups are compared. If the two intervals overlap to each other, the two groups are not significantly different and vice versa.

Let α denote the level of the CI and η denote the probability threshold described above. The selection of α and η affects the statistical inference. Previous studies show 95% ($\alpha = 0.05$) CIs are usually too wide. Setting large values for α and η – narrow CI and difficult threshold – would lead to high sensitivity but low specificity, and vice versa. The previous study [96] suggests moderate values $\alpha = 0.05$ and $\eta = 0.05$ in practice, which are used in this paper.

6.3.2 Simulation Study

In this paper, we validate the proposed model by applying Ba-FSOGL to simulated fNIRS datasets and comparing the reconstructed images with the simulated truth images. The fNIRS datasets are simulated using the Brain AnalyzIR toolbox [31]. In each iteration of simulation, brain activities are simulated within a specific Brodmann area (BA). The BA membership of each voxel of the atlas is used as the anatomical prior information for the image reconstruction.

6.3.2.1 Probe Configuration The probe used in the simulation study is the same as the one used in a previous publication. It contains nine light sources and eight detectors. Sources and detectors are respectively aligned, and the distances between neighboring sources/detectors are 20 mm. The source alignment is placed 25 mm apart from the detector alignment. The optical density is only measured between the nearest source-detector pairs. Hence, there are 32 (two wavelengths, 16 for HbO and the other 16 for HbR) channels defined in this probe. Fig. 6.3(a) shows the 2D layout of the probe in Cartesian coordinate system. The registration of the probe is constrained by an anchor and three attractors. Similar to the use of these terms in the AtlasViewer program [10], in the Brain AnalyzIR toolbox [31] , an anchor forcibly places a point of the probe layout (Fig. 6.3(a)) on the 10-20 system, and an attractor defines the direction to pull the probe. In this case, the origin of the probe (0, 0) in the 2D layout is anchored to the site Fpz. Three attractors are placed at positions (±200, 0) and (0, 100) in the 2D layout and attached to T7, T8, and Cz respectively, which define three forces pulling the probe along negative/positive horizontal axis and positive vertical axis to T7, T8, and Cz. An iterative least-squares minimization algorithm is used to register the probe based on the optimal source-detector pair spacings and the location of the anchor/attractor. Unit vectors are constructed using attractors to provide direction, which are updated with every iteration of the algorithm. The registered probe is shown in Fig. 6.3(b) and (c) using 10-20 (Mercator) projection and 3D geometry on an example head.

6.3.2.2 Pre-selection on Regions-of-interest The probe used in this study has a low-density style configuration that is frequently used in fNIRS studies due to the ease and economicalness of use. This style of probe has "blind-spots" because of regions of low-sensitivity to underlying brain activity [83]. The brain activity within the areas falling into blind-spots cannot be detected by the probe. Thus, we need to determine the detectable regions-of-interest before the simulation study.

Fig. 6.4 is a bar chart for the relative sensitivity to each Brodmann area (BA) using the probe. Due to the symmetry of the probe and the two brain hemispheres, we only simulate activities within the Brodmann areas on the left hemisphere. Thus, the Brodmann areas on the right side are omitted in Fig. 6.4. The values in the plot are calculated by summing

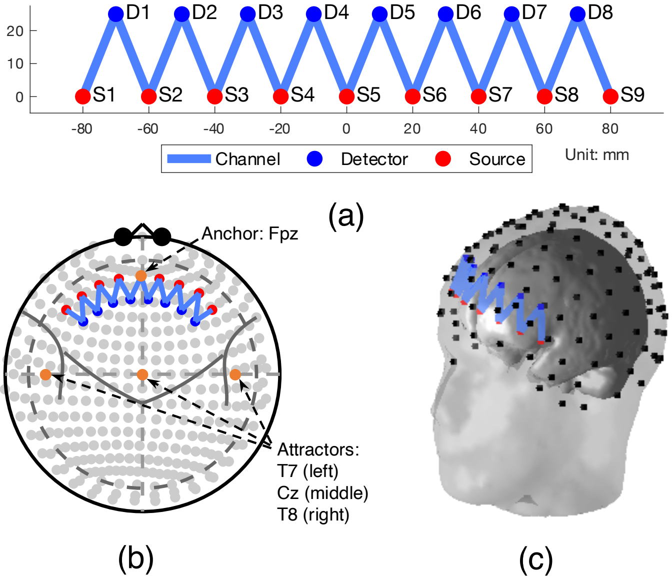

(a)

(b)

(c)

Figure 6.3: The topology of the probe used in the simulation: (a) The 2D layout in Cartesian coordinate system, (b) The registered probe with 10-20 system, and (c) The 3D geometry of the probe registered on an example head.

up the forward model of all voxels within each area, then scaling the values by the largest sensitivity among all areas. From the figure, we can see that the probe is most sensitive to BA-10 followed by BA-46, BA-45, and BA-11. For the remaining regions, considering the sensitivities are less than $\frac{1}{30}$ of BA-10, which means the brain activity in any one of these regions cannot survive from the physiological noise in BA-10 unless the signal-to-noise (SNR) is impractically greater than 900, a reasonable brain activity in these regions is not observable using this probe, so we will not generate brain activity in these regions. BA-11 is located at the bottom of the frontal lobe of brain, i.e., right beneath BA-10. The two regions are covered by the same source-detector pairs of the probe used in this study, and the light sent from those sources goes through both regions. A brain activity in BA-11 consequently always results in a smaller false positive (FP) in BA-10, since it is closer to the probe and regularization-based approaches tend to select variables with smaller values. Therefore, BA-11 is another region that will not be used in the simulation.

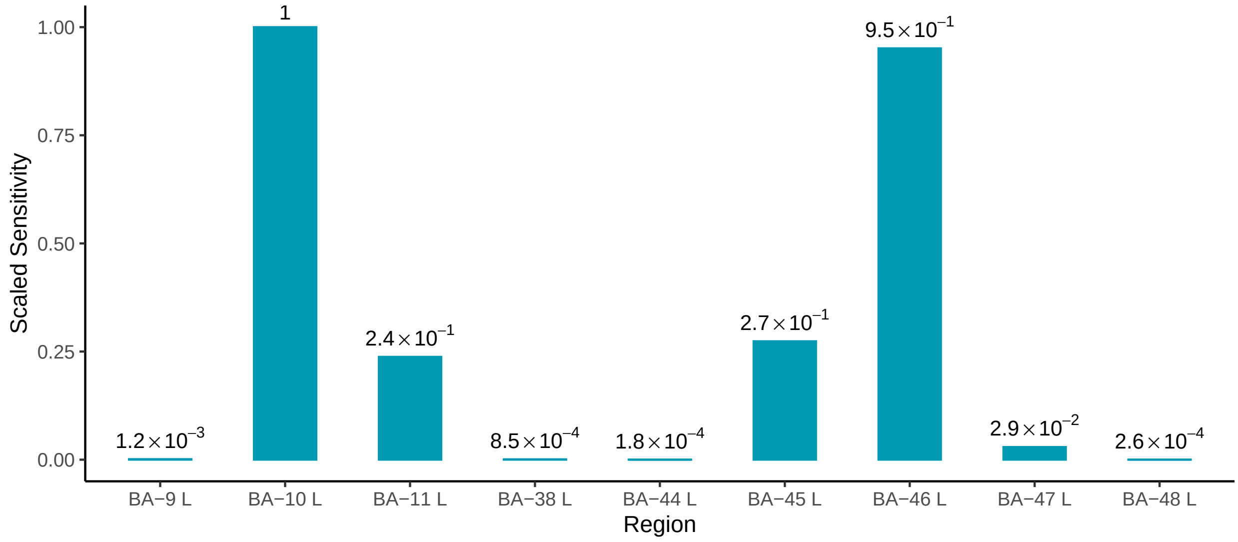

Figure 6.4: Scaled sensitivity of each Brodmann area to the probe. The values in the plot are calculated by summing up the forward model of all voxels within each area, then scaling the values by the largest sensitivity among all areas. Due to the symmetry of the brain, only the left regions are shown here. Note that 1) the scaled sensitivities in this plot are calculated based on the specific probe in this study; 2) voxels apart from the nearest channel further than 5 cm are excluded, so the entirely excluded regions are not shown in this plot (e.g., BA-39, etc.)

Brain activities in BA-10, BA-45, and BA-46, both left and right side, will be considered as the regions-of-interest using the probe. Fig. 6.5 (a) – (c) show the locations of the three left regions on the cortex as well as their relative positions to the probe. Fig. 6.5 (d) demonstrates the most sensitive area from each channel where we can see the middle four channels are more sensitive to BA-10 while the lateral two channels are more sensitive to BA-46. There is no channel most sensitive to BA-45 because it is further from all channels of the probe than BA-10 and BA-46.

6.3.2.3 Stimulus Generation The fNIRS data is simulated by adding stimulation on autoregressive noise. The time difference between two neighboring stimuli is exponentially

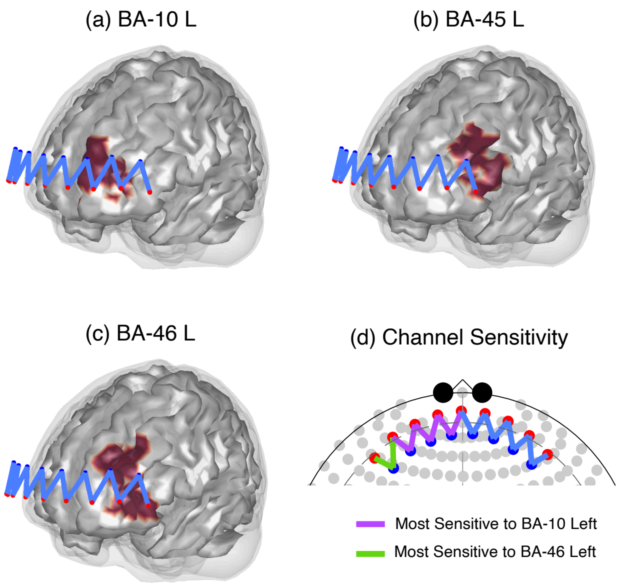

Figure 6.5: (a) – (c) The locations of left BA-10, BA-45, and BA-46 on the cortex as well as their relative positions to the probe. (d) The most sensitive area from each channel. Note that the right side is omitted due to the symmetry.

distributed. The hemodynamic response to the stimulus is simulated using canonical hemodynamic response function. The peaks of HbO and HbR concentration changes are 7 and -2 μM (micromolar, a.k.a., μmol/L) respectively. In brief, simulated "brain" activity within the ROI (true positive) is computed and projected to fNIRS channel/measurement space via the optical forward model. The details are described in Ref. [31]. In each iteration of simulations, we simulate the stimulus in only one ROIs, and both stimulus added data and the corresponding noise data will be reconstructed using Ba-FSOGL. Since the left and right three ROIs are mirrored correspondingly, only the left three regions are used to generate stimulus to avoid complexity. For each of the three regions, BA-10 left, BA-45 left, and BA-46 left, we simulate 100 datasets by adding stimulus in the corresponding regions to noise data using Brain AnalyzIR toolbox, and the 100 noise-only datasets are also retained for estimating false positive rate (FPR). To sum up, 600 datasets – 300 activity-present and 300 noise-only – are simulated in this study.

6.3.2.4 Image Reconstruction Evaluation We will evaluate the reconstructed images using conventional indicators and receiver operating characteristics (ROC) performance. The two conventional indicators are mean squared error (MSE) and contrast-to-noise (CNR) defined as follows:

$$\mathrm{MSE}_{\mathrm{HbX}} = \frac{1}{P/2} \left\| \boldsymbol{\beta}_{\mathrm{HbX}} - \widehat{\boldsymbol{\beta}}_{\mathrm{HbX}} \right\|_2^2 \tag{6.27}$$

$$\mathrm{CNR}_{\mathrm{HbX}} = 10 \times \log_{10} \left(\frac{\left\| \widehat{\boldsymbol{\beta}}_{\mathrm{HbX}} \right\|_2^2}{\left\| \boldsymbol{\beta}_{\mathrm{HbX}} - \widehat{\boldsymbol{\beta}}_{\mathrm{HbX}} \right\|_2^2} \right) \tag{6.28}$$

where $\boldsymbol{\beta}_{\mathrm{HbX}}$ and $\widehat{\boldsymbol{\beta}}_{\mathrm{HbX}}$ are the ground truth and estimates for HbO/HbR changes from a given dataset. Note that the averaging factor of MSE is $\frac{P}{2}$ because $\boldsymbol{\beta}_{\mathrm{HbO}}$ and $\boldsymbol{\beta}_{\mathrm{HbR}}$ are the two halves of $\boldsymbol{\beta}$ with an equal length. MSE measures the average of the difference between the truth and the reconstructed images and CNR shows the ability to distinguish brain activities from the background noise.

The ROC used in this study is called ROI-ROC [43, 44]. Note that the term “ROI” used in this paragraph has a different definition from that in the remaining sections of this paper. Here the ROI refers to any area with a rating. In the evaluation of the image reconstruction results, two levels of ROI are used – voxel and BA level. The ROC performance of the model is evaluated per the active region. For brain activity in each of the three BAs, the estimated HbO and HbR changes at each voxel of the 200 datasets (100 activity-present and 100 noise-only) are respectively concatenated, in which the hemoglobin changes for the voxels in an active region will be considered as true positives (TP) and FPs otherwise. The values of $\boldsymbol{\beta}_g^{\mathrm{T}} \boldsymbol{\Sigma}_g^{-1} \boldsymbol{\beta}_g$ for the six BAs are concatenated with the same definitions of TP and FP from the 200 datasets. Thus, we can draw three ROC curves – two at the voxel level (HbO and HbR) and one at the BA level, in which the estimated HbO change, the negative estimated HbR change (as the HbR change in an active region is negative), and $\boldsymbol{\beta}_g^{\mathrm{T}} \boldsymbol{\Sigma}_g^{-1} \boldsymbol{\beta}_g$ are respectively used as the ROI-ROC rating to construct the ROI-ROC curve.

6.3.2.5 Choosing Hyperparameters and Initial Values

Bayesian approach requires a reasonable selection on the hyperparameters and initial values, especially for high-dimensional problems. We will discuss how to determine these values in this section.

First, the hyperparameters r and s for the hyperprior distribution of σ^2, given in Eq. 6.17, are determined by preliminary trials. In this study, we find that the magnitude of the samples of σ^2 should be around 0.005 so that the samples of $\boldsymbol{\beta}$ can fluctuate from zero but not be too large to break the Gibbs sampler. To limit σ^2 within a reasonable range, we set $r = 2500$ and $s = 0$. Then it is found that the initial value of the tuning parameter λ_g can affect the image reconstruction result, although the algorithm optimizes it during the Gibbs sampling process, which is a common problem that different start points may lead an optimization process to different local optimass. In this study, we perform channel-space ROI analysis for all ROIs before the image reconstruction following the method described in a previous study [74]. The channel-space analysis can provide the prior information on which ROI has the most significant activity by comparing their channel-space ROI statistics. Then we apply Ba-FSOGL to the dataset to reconstruct images with multiple initial λ_g. Note that λ_g starts from the same value for all ROIs in each time of image reconstruction. After obtaining the reconstructed images using multiple initial values, we can determine which is the best estimation based on the channel-space analysis. If no significant activity is found from any ROI (no p-value ¡ 0.05), this dataset will be considered as a noise-only dataset, for which we know the ground truth is all zeros. The initial λ_g generating the minimum MSE will be selected as the final result of the image reconstruction. If significant activities are found in at least one ROI, the most significant (with the smallest p-value) ROI will be considered to contain the brain activity. Although the values of HbO and HbR changes are unknown, we can construct an ROC curve for the reconstructed image using each initial λ_g. In addition, the MSE for the remaining ROIs can be calculated since we know there is no activity in these ROIs and the HbO and HbR changes are expected to be zero. The optimal initial value of λ_g can be selected based on the area under the ROC curve (AUC) and the MSE. Fig. 6.6 is an example of image reconstruction for a simulation dataset containing brain activity within BA-46 left area. The channel-space analysis demonstrates that BA-46 left area is the most active one among the six Brodmann ROIs. The left panel of the figure shows the image reconstruction on HbO while the right panel is for HbR. The bottom two heatmaps concludes the image reconstruction results using 50 initial λ_g values from 0.05 to 2.5. Each column represents a reconstructed image using the initial λ_g indicated on the horizontal axis. The image is split into six parts along the vertical axis whose ROI membership is indicated on the axis. The color of the heatmap represents the value of the HbO/HbR change. The truth values are annotated on the legends. The four line plots show the ROC AUC and MSE described above. From this figures, we can see that image reconstructions with initial $\lambda_g < 0.3$ are completely off the target where a brain activity stronger (brighter color) than the simulated ground truth is estimated at a different ROI (BA-45 left instead of BA-46 left), so it is not surprised that the ROC AUCs are lower and the MSEs are higher in this range of initial λ_g. It is widely known that the solution for an underdetermined inverse problem is not unique. As the level of regularization increases, the optimization tends to select variables with smaller coefficients. This nature of regularization methods can be seen from this figure. Since BA-45 left is further from the probe than BA-46 left, a same measurement vector y can be obtained with a larger brain activity in BA-45 left or a smaller one in BA-46 left with different noise. Thus, the larger activity in BA-45 left is preferred by small initial λ_g while the smaller on in BA-46 left is preferred by larger initial λ_g. To select the best initial λ_g, we can compare their AUCs and MSEs. As we can see from the line plots of Fig. 6.6, the AUCs are stable around a high level for initial $\lambda_g > 0.5$ while the MSE continues decreasing until 2.4. Thus, the optimal initial value of λ_g for this dataset is about 2.4.

A question may be raised about the search range of the initial λ_g. From this study, we find that the results for initial $\lambda_g > 2.5$ are stable and similar until it is over-regularized around initial $\lambda_g = 10$ and gives an all-zero estimation. Thus, we will omit the results for initial $\lambda_g > 2.5$ and only select initial λ_g from the range shown in Fig. 6.6.

Two more hyperparameters need to be determined are θ and γ controlling the weights of the three penalty terms. These two hyperparameters can be selected based on prior knowledge and preliminary trials. For example, simulation datasets are used in this study, in which the brain activities are uniform within the active region and anti-correlation between HbO and HbR changes are properly simulated. Thus, we need a large weight for the fused and group lasso penalty terms but a small weight for the sparse penalty term. After some

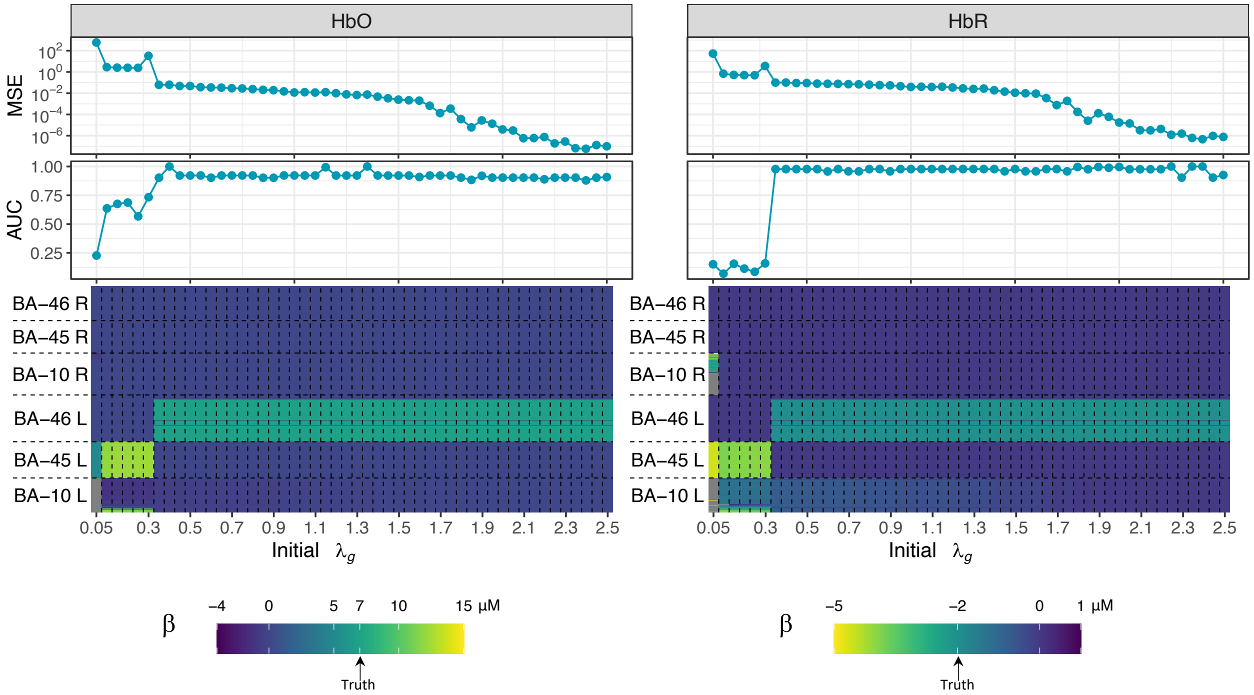

Figure 6.6: An example of image reconstruction for a simulation dataset containing brain activity within BA-46 left area. The left panel of the figure shows the image reconstruction on HbO while the right panel is for HbR. The bottom two heatmaps conclude the image reconstruction results using 50 initial λ_g values from 0.05 to 2.5. Each column represents a reconstructed image using the initial λ_g indicated on the horizontal axis. The image is split into six parts along the vertical axis whose ROI membership is indicated on the axis. The color of the heatmap represents the value of the HbO/HbR change. The truth values are annotated on the legends. The two line plots shows the ROC AUC and MSE.

preliminary trials, we select $\theta = 0.125$ and $\gamma = 0.4$, which assigns 0.05, 0.6, and 0.35 as the weight of the sparse, fused, and group lasso penalty term respectively. This combination of weights results in fairly uniform brain activity and anti-correlated HbO and HbR changes. If there is little prior information on the penalty weights is known, we can still use the approach described in this section for selecting λ_g to determine θ and γ.

6.3.3 Implementation of fNIRS Data Simulation and Gibbs Sampler

The simulation of fNIRS brain image data has already been implemented in the Brain AnalyzIR toolbox – an open-source MATLAB-based analysis toolbox for fNIRS data. This section describes the main components of fNIRS data simulation in the toolbox as well as the Gibbs sampler implementation.

6.3.3.1 Forward Model The AnalyzIR toolbox provides accesses to third-party optical forward model solvers including NIRFAST [79, 85], Mesh-based Monte Carlo (MMC; [86, 87]) and Monte Carlo Extreme (MCX; [25, 88]), which allow construction and import of individual head models from anatomical MRI volumes. We can use these solvers to generate the optical forward model with either atlas-based or individual MRI head models. However, since the computation of optical forward models is usually time consuming and furthermore the individual-level anatomical modeling is not always available for all subjects (e.g. pediatric fNIRS studies), the default options in the AnalyzIR toolbox, which are also used in this study, utilize a pre-segmented head model derived from the Colin-27 atlas [81].

6.3.3.2 Brodmann Area Parcellation The fNIRS AnalyzIR toolbox contains atlas-based parcellations of the Colin-27 atlas brain [81] based on several packages including the automatic-anatomical labeling model (AAL2) [119], the Freesurfer Desikan-Killiany atla [120], Human-Connectome Project MSM atlas [121], and Broadmann area labels from both the Talairach Daemon [90] and the MRIcron provided atlas [122]. In this work, the Talairach Daemon labeling of the Brodmann areas was used.

6.3.3.3 Gibbs Sampler Implementation For each of the 600 datasets, we apply the proposed Ba-FSOGL model with 50 different initial λ_g for image reconstruction and select the optimal estimated images following the method described in Section 6.3.1.3. The Gibbs sampler for the Ba-FSOGL model is implemented in MATLAB using its built-in random number generators for sampling from multivariate normal, inverse gamma, and inverse Gaussian distributions. For a specific fNIRS dataset with a given value of initial λ_g, the Gibbs sampler runs 100,000 sampling iterations, in which the first 10,000 iterations are abandoned as the burn-in period and the samples are extracted every 9 iterations in the remaining 90,000 iterations to maintain the independence among the output samples as nearby samples in a Markov chain are not independent. Finally, 10,000 samples are finally retained from the Gibbs sampling process for estimating $\boldsymbol{\beta}$.

6.4 Results

In this study, we run the image reconstruction model 600 (simulation datasets) × 50 (initial values for λ_g) = 30,000 times in total. Each time the model costs approximately an hour to return the final result using MATLAB R2020a on macOS 10.15.6, Intel Core i7 2.6 GHz 6-core CPU, and 16 GByte memory. The entire 30,000-hour task was parallelly completed on a large-scale computer cluster. The results of the image reconstruction, statistical inference, and image evaluation are summarized in this section.

6.4.1 Reconstructed Image

Fig. 6.6 – Fig. 6.10 show the truth and averaged reconstructed images for the datasets with BA-10 left, BA-45 left, BA-46 left, and no area (noise-only) active respectively, which provide a visual comparison of the image reconstruction to the ground truth. In each figure, the two rows contain the images for HbO and HbR, respectively. The left column displays the two ground truth images whose colors are annotated on the color bar. The images in the remaining column(s) are the averaged reconstructed images where true and false positives are listed separately. Note that the color for the ground truth is preserved on the same color scale, i.e., 0, 7, and -2 are colored the same across the four figures while the color scales for other values are different (see the color bar). The fraction under the column title of true/false positive indicates the proportion of successful/failed image reconstructions that are obtained to generate the averaged images. From Fig. 6.7 – Fig. 6.9, we can see that most of the datasets containing brain activity – 100%, 81%, and 96% for activity within

BA-10 left, BA-45 left, and BA-46 left respectively – are successfully reconstructed as TPs, although the reconstructed activities are slightly smaller (lighter color) than the simulated truth. However, a small fraction of FPs can still be seen in Fig. 6.8 – Fig. 6.10. Since BA-45 left and BA-46 left are at the side of the probe and BA-45 left is further to the probe, the optical measurements for the activity within BA-45 left are sometimes similar to those for a smaller activity within BA-46 left, and vice versa, as explained in Section 6.3.1.3. Therefore, smaller activity (lighter color) in BA-46 left is reconstructed as FPs from 19% of the datasets containing activity within BA-45 left, and 4% FPs are obtained from BA-46 left active datasets with larger brain activity (darker color) in BA-45 left. In addition, slight FPs are shown in BA-10 left in 1% of the noise datasets.

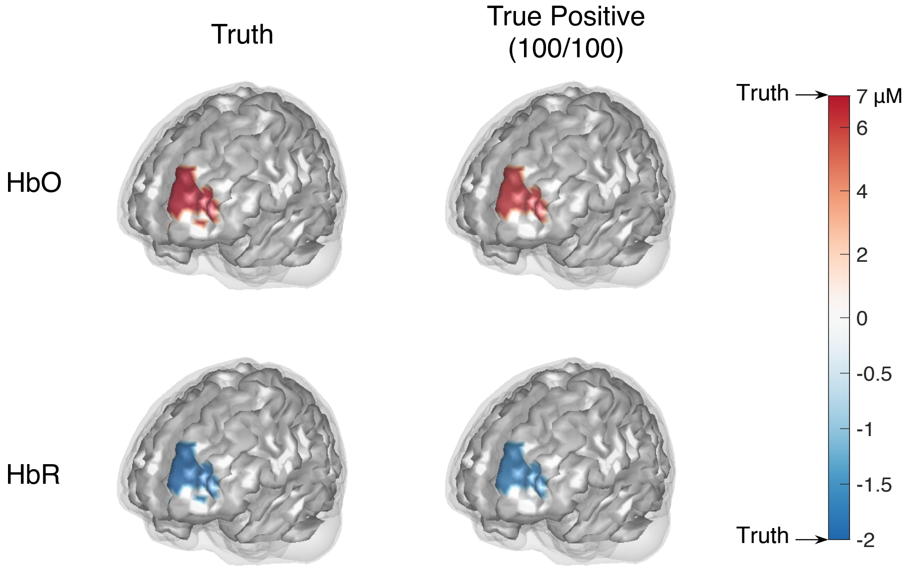

Figure 6.7: The ground truth and averaged reconstructed image for the datasets with activity in BA-10 left. The two rows indicate the images for HbO and HbR respectively. The left column displays the two ground truth images whose colors are annotated on the color bar. The two images in the right column are the averaged images that successfully recover a brain activity in BA-10 left (true positives). In this case, all 100 datasets are successfully recovered with a slightly smaller activity.

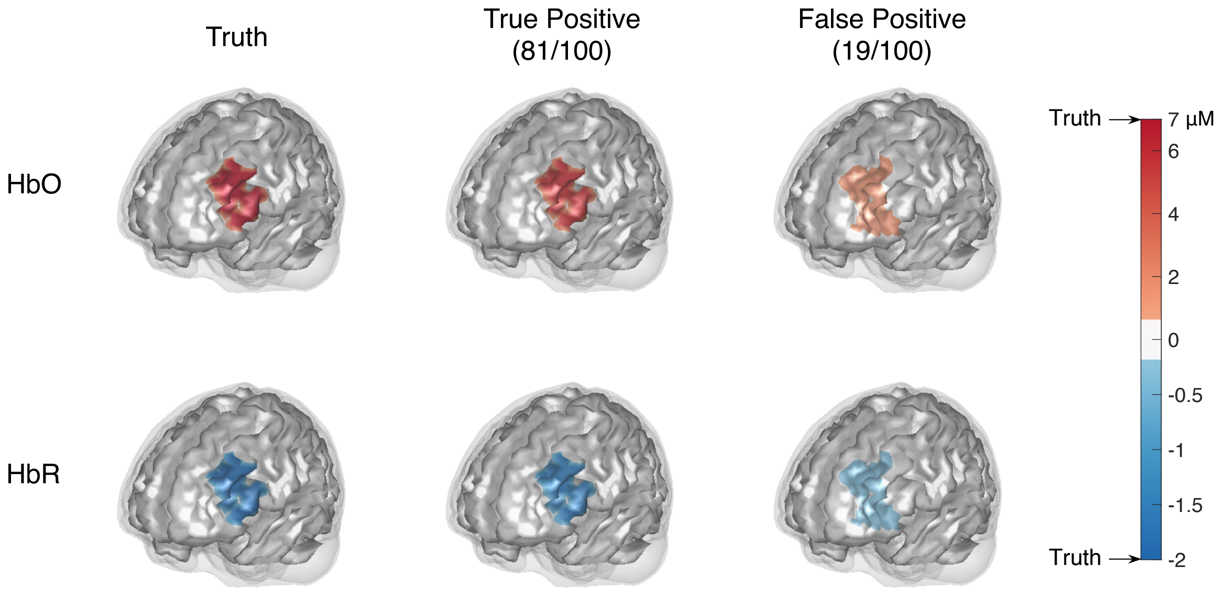

Figure 6.8: The ground truth and averaged reconstructed images for the datasets with activity in BA-45 left. The two rows indicate the images for HbO and HbR respectively. The left column displays the two ground truth images whose colors are annotated on the color bar. The two images in the middle column are the averaged images that successfully recover a brain activity in BA-45 left (true positives). The two images in the right column are the averaged images that recover a brain activity in regions other than BA-45 left (false positives). In this case, 81 TPs and 19 FPs are obtained.

6.4.2 Statistical Inference

Fig. 6.11 – Fig. 6.14 show the statistical inference results for the image reconstruction of datasets with brain activity simulated in BA-10 left, BA-45 left, BA-46 left, and no area (noise-only) active respectively. Each of the four figures consists of four subplots. Subplots in panels (a) are line plots showing a clear comparison between the ground truth and the median of the estimates where we can see the absolute estimates for the voxels contained in active regions are slightly lower than the ground truths from Fig. 6.11 (a) – Fig. 6.13 (a) and the estimates for the noise data fluctuate around the truths within a small range in Fig. 6.14

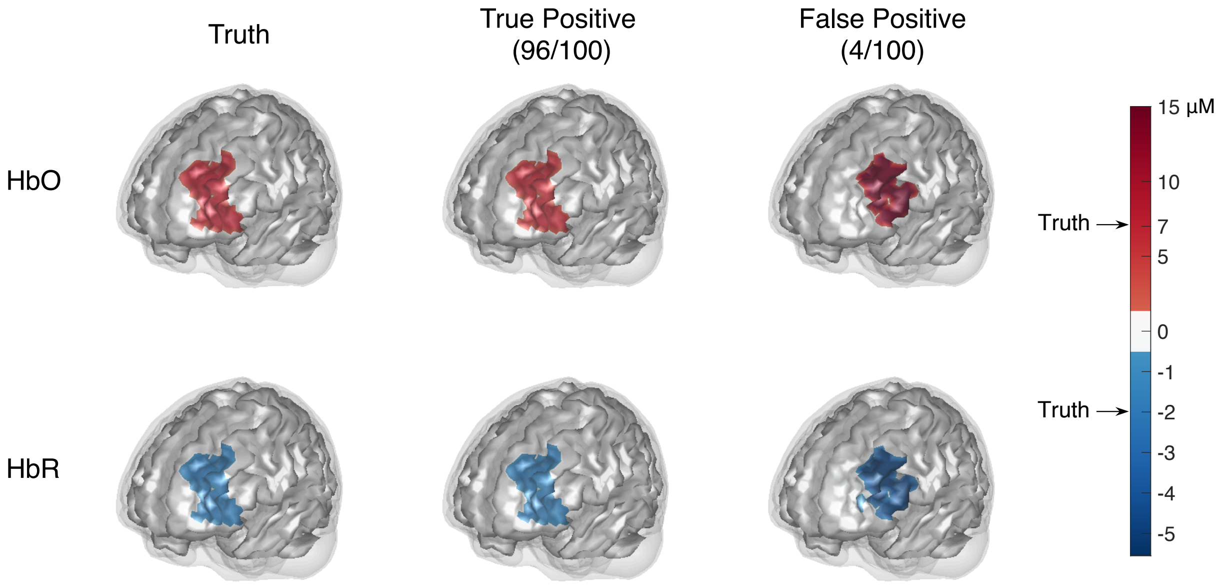

Figure 6.9: The ground truth and averaged reconstructed images for the datasets with activity in BA-46 left. The two rows indicate the images for HbO and HbR respectively. The left column displays the two ground truth images whose colors are annotated on the color bar. The two images in the middle column are the averaged images that successfully recover a brain activity in BA-46 left (true positives). The two images in the right column are the averaged images that recover a brain activity in regions other than BA-46 left (false positives). In this case, 96 TPs and 4 FPs are obtained.

(a). Subplots (b) – (d) summarize the inference using the three methods described in Section 6.3.1.4 respectively. Note that each point on the lines of the truth, estimate, CI limit, and posterior probability in subplots (a) – (c) is calculated from the one million samples (10,000 samples/dataset × 100 datasets) for a specific HbO/HbR change at the voxel belonging to the area distinguished by the white/grey color and indicated at the x-axis, i.e., every point of the estimate line (dark blue in subplots (a) and (b)) represents the median, that of the lower/upper limit line (red/green line in subplot (b)) represents the lower/upper 50% quantile, and that of the posterior probability line (light blue line in subplot(c)) represents the fraction of samples with in the scaled neighborhood interval. The boxplots in subplots

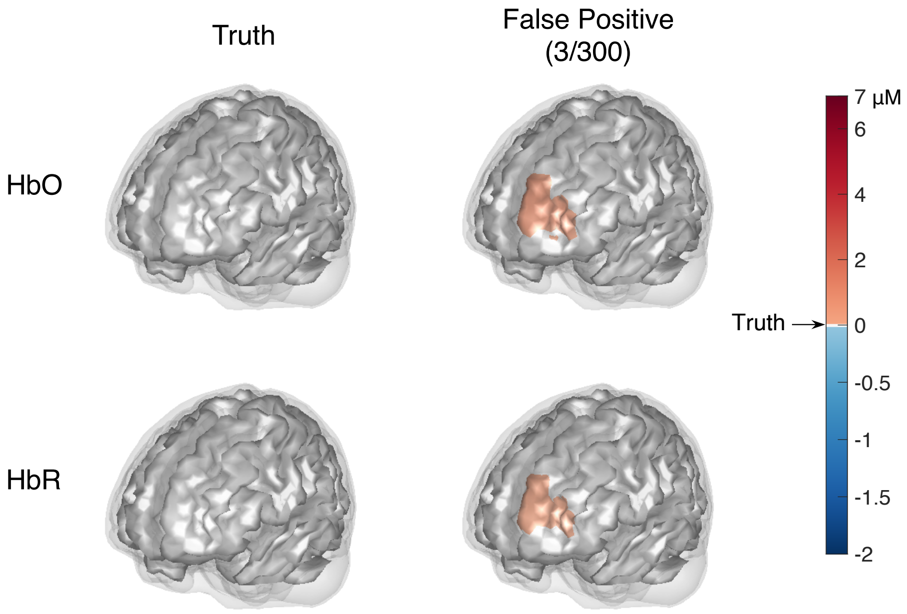

Figure 6.10: The ground truth and averaged reconstructed images for the datasets without brain activities. The two rows indicate the images for HbO and HbR respectively. The left column displays the two ground truth images whose colors are annotated on the color bar. The two images in the right column are the averaged images that recover a brain activity in any region (false positives). In this case, three FPs out of 300 datasets are obtained.

(d) are calculated from the one million samples of $\boldsymbol{\beta}_g^{\mathrm{T}}\boldsymbol{\Sigma}_g^{-1}\boldsymbol{\beta}_g$ for the six regions. Note that the number of samples used for generating Fig. 6.14 (a) – (d) is three million instead of one million used in Fig. 6.11 – Fig. 6.13, since there are 300 noise-only datasets.

From the four subplots in Fig. 6.11 – Fig. 6.14, we can see the three approaches for statistical inference described in Section 6.3.1.4 provide a consistent conclusion. It can be seen from subplots (b) that only the CI of the active areas exclude 0. In subplots (c), the posterior probability of the Gibbs samples within the scaled neighborhood interval is only below the 50% threshold for the active areas. Subplots (d) show that only the active areas have a non-overlapping CI with the remaining areas. That is to say that statistical significance only appears in the truly active regions. Although there are a few exceptional

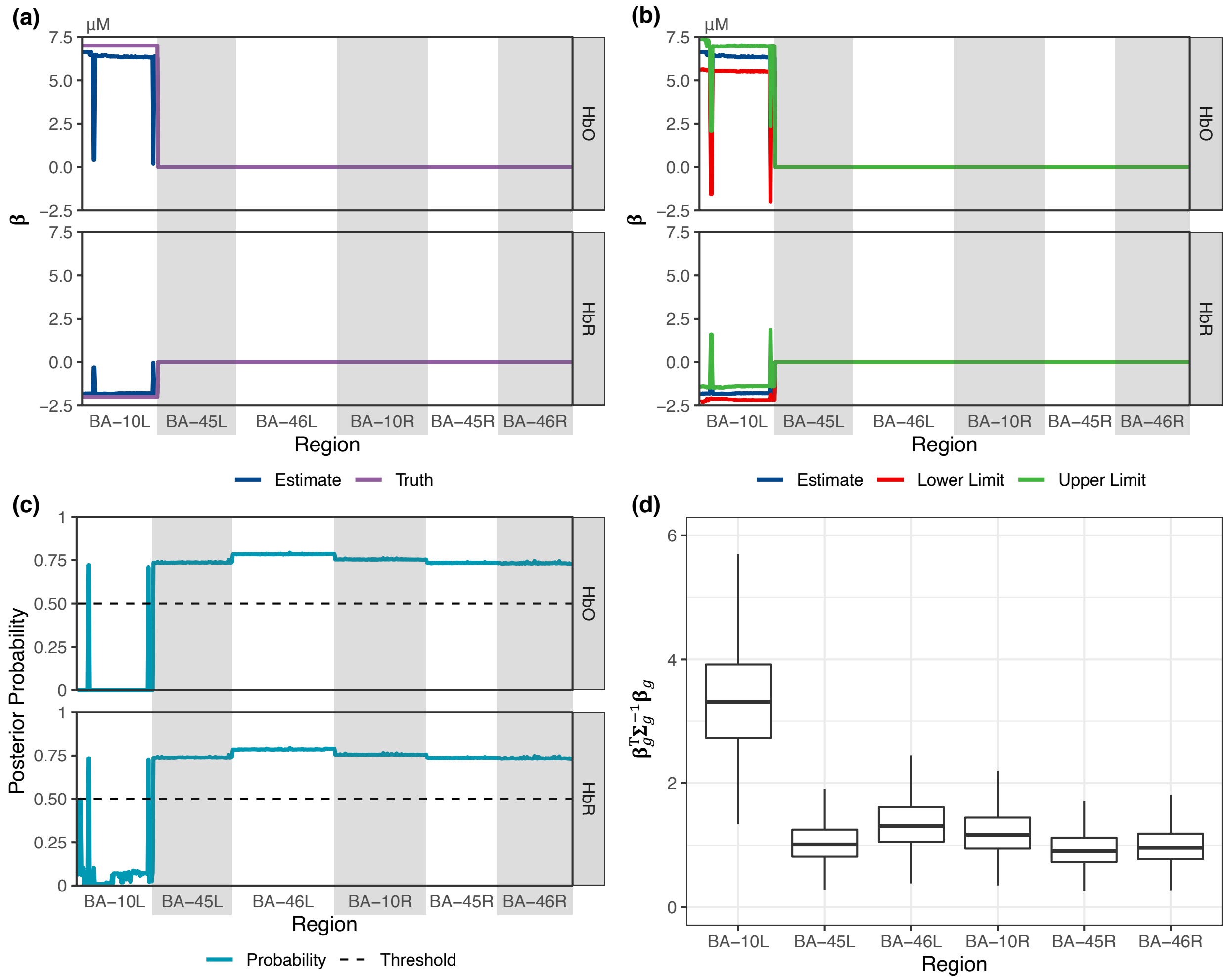

Figure 6.11: Four subplots showing the statistical inference for the image reconstruction of 100 datasets with brain activity simulated in BA-10 left. (a) The line plot of the ground truth and the estimated hemoglobin changes. (b) The estimated hemoglobin changes and the 50% CIs. (c) The posterior probability that β_p is within the scaled neighborhood interval $\left[-\sqrt{\mathrm{Var}\left(\beta_p \mid \mathbf{X}, \mathbf{y}\right)}, \sqrt{\mathrm{Var}\left(\beta_p \mid \mathbf{X}, \mathbf{y}\right)}\right]$ and the 50% probability threshold. (d) The boxplot of $\boldsymbol{\beta}_g^{\mathrm{T}} \Sigma_g^{-1} \boldsymbol{\beta}_g$ for all available Brodmann Areas. Note that each point of the lines in (a) – (c) represents the value at a voxel belonging to the region indicated on the horizontal axis and separated using the grey-shaded/white areas. Subplots (b) – (d) respectively show the statistical inference via the three approaches described in Section 6.3.1.4, from which we can conclude that the hemoglobin changes at most individual voxels in BA-10 left are significant based on the CI and the probability within the scaled neighborhood interval, and the brain activity in BA-10 left is significantly larger than that in the remaining ROIs as an entirety.

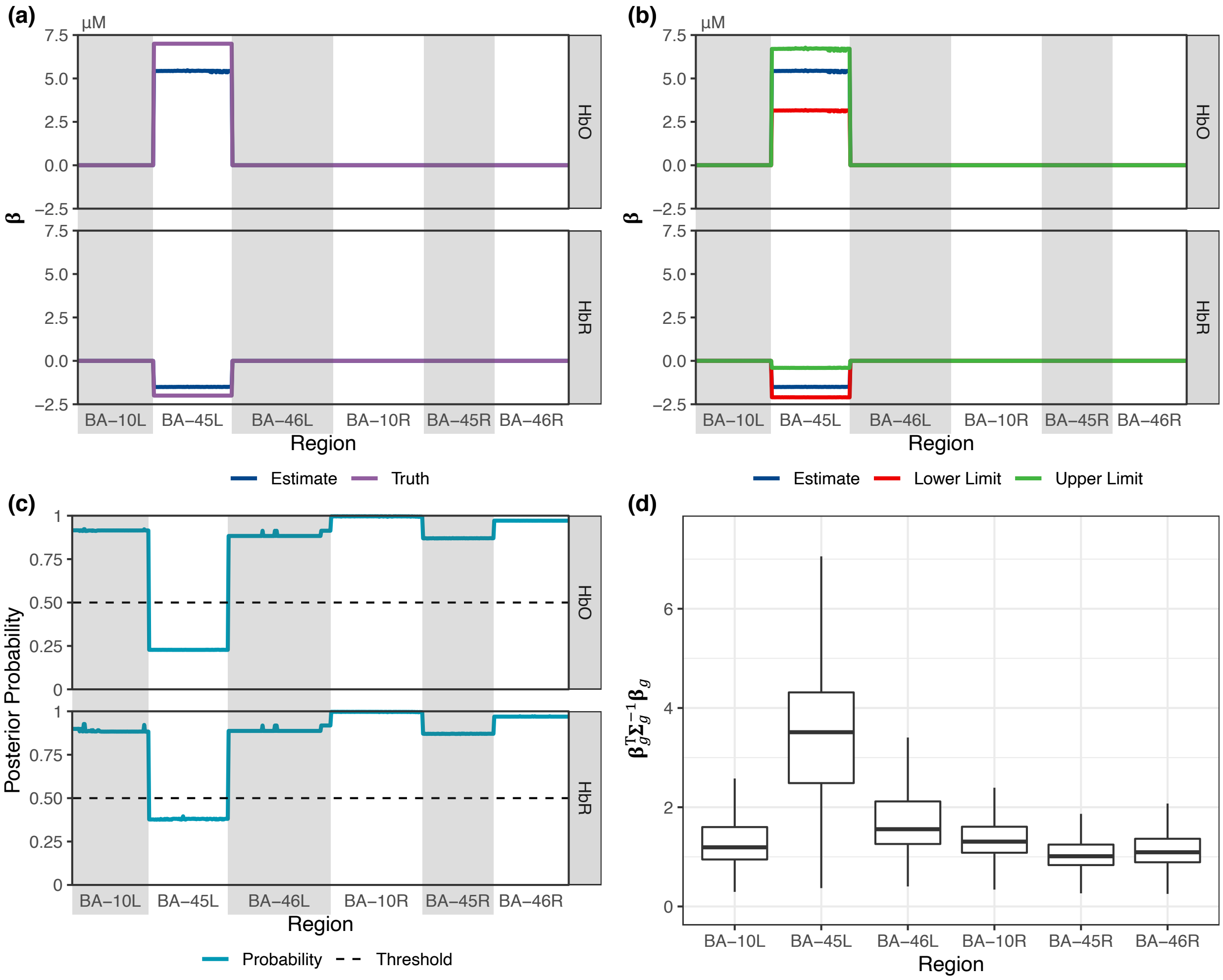

Figure 6.12: Four subplots showing the statistical inference for the image reconstruction of 100 datasets with brain activity simulated in BA-45 left. (a) The line plot of the ground truth and the estimated hemoglobin changes. (b) The estimated hemoglobin changes and the 50% CIs. (c) The posterior probability that β_p is within the scaled neighborhood interval $\left[-\sqrt{\operatorname{Var}\left(\beta_p \mid \mathbf{X}, \mathbf{y}\right)}, \sqrt{\operatorname{Var}\left(\beta_p \mid \mathbf{X}, \mathbf{y}\right)}\right]$ and the 50% probability threshold. (d) The boxplot of $\boldsymbol{\beta}_g^{\mathrm{T}}\Sigma_g^{-1}\boldsymbol{\beta}_g$ for all available Brodmann Areas. Note that each point of the lines in (a) – (c) represents the value at a voxel belonging to the region indicated on the horizontal axis and separated using the grey-shaded/white areas. Subplots (b) – (d) respectively show the statistical inference via the three approaches described in Section 6.3.1.4, from which we can conclude that the hemoglobin changes at all individual voxels in BA-45 left are significant based on the CI and the probability within the scaled neighborhood interval, and the brain activity in BA-45 left is significantly larger than that in the remaining ROIs as an entirety.

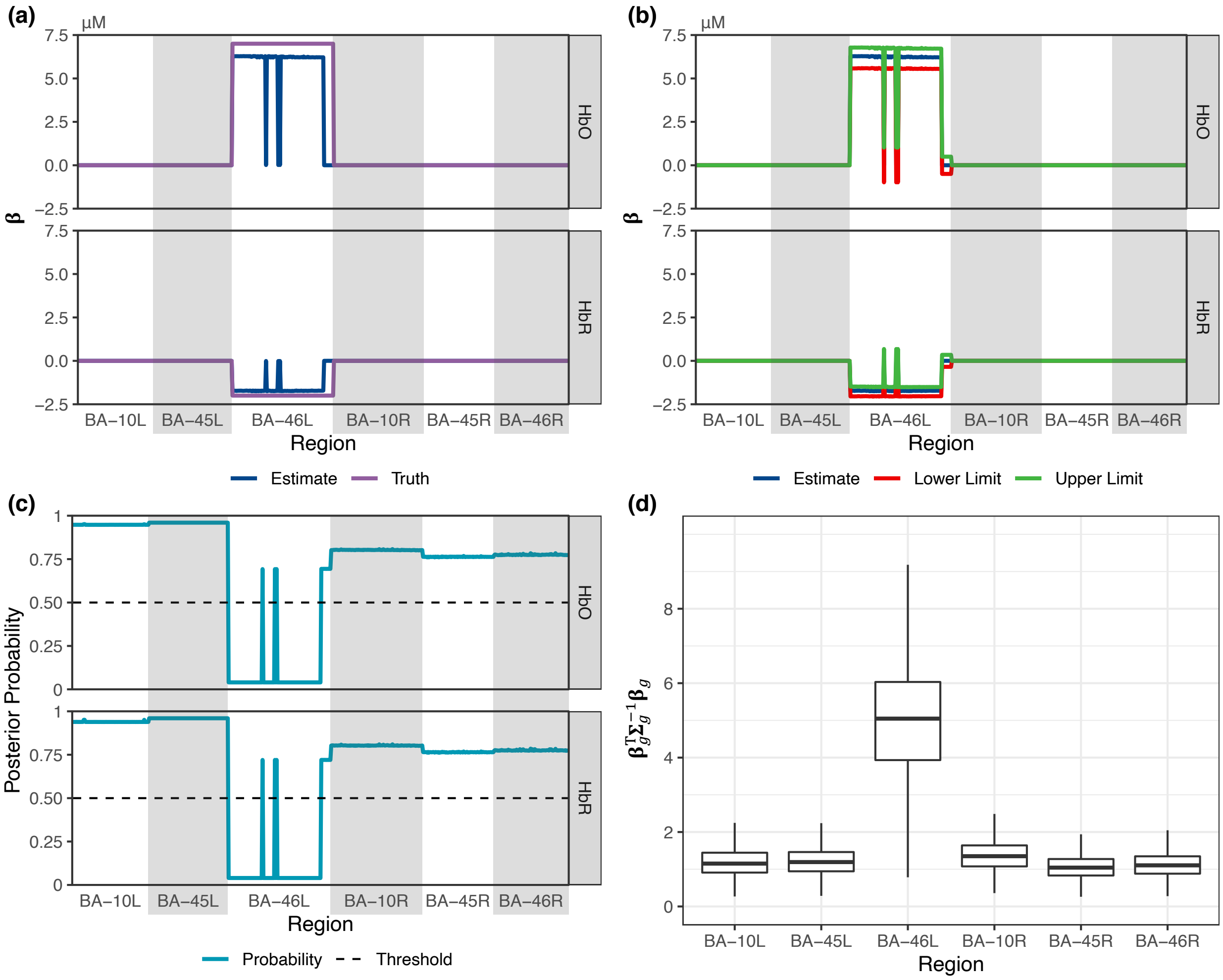

Figure 6.13: Four subplots showing the statistical inference for the image reconstruction of 100 datasets with brain activity simulated in BA-46 left. (a) The line plot of the ground truth and the estimated hemoglobin changes. (b) The estimated hemoglobin changes and the 50% CIs. (c) The posterior probability that β_p is within the scaled neighborhood interval $\left[-\sqrt{\operatorname{Var}(\beta_p \mid \mathbf{X}, \mathbf{y})}, \sqrt{\operatorname{Var}(\beta_p \mid \mathbf{X}, \mathbf{y})}\right]$ and the 50% probability threshold. (d) The boxplot of $\boldsymbol{\beta}_g^{\mathrm{T}} \Sigma_g^{-1} \boldsymbol{\beta}_g$ for all available Brodmann Areas. Note that each point of the lines in (a) – (c) represents the value at a voxel belonging to the region indicated on the horizontal axis and separated using the grey-shaded/white areas. Subplots (b) – (d) respectively show the statistical inference via the three approaches described in Section 6.3.1.4, from which we can conclude that the hemoglobin changes at most individual voxels in BA-46 left are significant based on the CI and the probability within the scaled neighborhood interval, and the brain activity in BA-46 left is significantly larger than that in the remaining ROIs as an entirety.

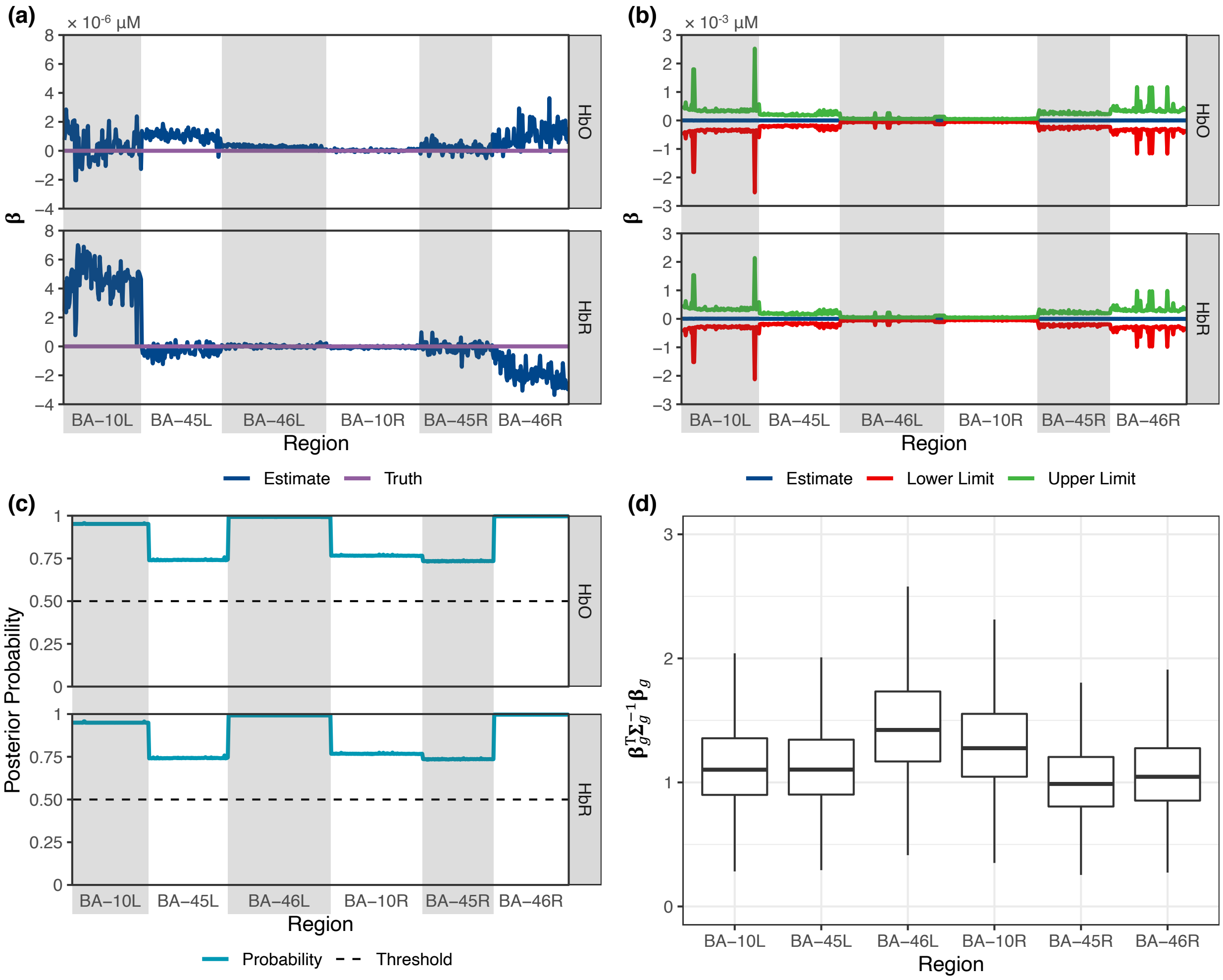

Figure 6.14: Four subplots showing the statistical inference for the image reconstruction of 100 datasets with no brain activity simulated in any areas. (a) The line plot of the ground truth and the estimated hemoglobin changes. (b) The estimated hemoglobin changes and the 50% CIs. (c) The posterior probability that β_p is within the scaled neighborhood interval $\left[-\sqrt{\operatorname{Var}\left(\beta_p \mid \mathbf{X}, \mathbf{y}\right)}, \sqrt{\operatorname{Var}\left(\beta_p \mid \mathbf{X}, \mathbf{y}\right)}\right]$ and the 50% probability threshold. (d) The boxplot of $\boldsymbol{\beta}_g^{\mathrm{T}} \Sigma_g^{-1} \boldsymbol{\beta}_g$ for all available Brodmann Areas. Note that each point of the lines in (a) – (c) represents the value at a voxel belonging to the region indicated on the horizontal axis and separated using the grey-shaded/white areas. Subplots (b) – (d) respectively show the statistical inference via the three approaches described in Section 6.3.1.4, from which we can conclude that the hemoglobin changes at all individual voxels are insignificant based on the CI and the probability within the scaled neighborhood interval, and there is no brain activity in any ROI that is significantly larger than that in the remaining ROIs as an entirety.

voxels in active regions do not show statistical significance (type-II error), we never see any statistical significance in any inactive regions (type-I error).

6.4.3 Image Evaluation

6.4.3.1 Mean Squared Error and Contrast-to-noise Ratio The results of MSE and CNR are summarized in Table 6.2. For each dataset, the MSE and CNR are calculated using Eq. 6.27 and 6.28. The median of MSE and CNR of each 100 datasets with activity in BA-10, BA-45, and BA-46 left are shown in the table. Since CNR is not available for noise data, we only list the MSE median of the 300 noise datasets here. The reason we use median instead of mean of MSE and CNR here is because the FPs make remarkable detrimental contributions to the mean values although there are only a few FP cases. The values in this table indicate small discrepancies between the estimations and the simulation truths as well as large contrasts to distinguish the reconstructed brain activities from the background noise.

Table 6.2: The median of mean squared errors and the contrast-to-noise ratios (dB) of the HbO and HbR changes estimation for the datasets with different active regions

	MSE Median		CNR Median (dB)	
Active Region	HbO	HbR	HbO	HbR
BA-10 Left	0.42	0.07	12.03	9.01
BA-45 Left	0.55	0.11	10.42	7.29
BA-46 Left	1.34	0.12	7.24	6.61
None (noise)	1.84×10^{-10}	2.37×10^{-10}	NA	NA

6.4.3.2 ROC Performance Fig. 6.15 shows the ROI-ROC curves for the image reconstruction of the datasets with simulated activity in three different Brodmann Areas against the corresponding noise data. The three active regions are indicated by the line color, and the two levels of ROC curve are indicated by the title of the three panels – two at voxel level (HbO and HbR) and one at ROI level. The AUCs of the ROC curves are shown at the lower-right corner of each panel. The AUC means the probability that the active voxels/regions have a higher rating than the inactive ones. As we can see, the AUCs are all greater than 0.89, which indicates the good ROC performance of the Ba-FSOGL model on fNIRS image reconstruction.

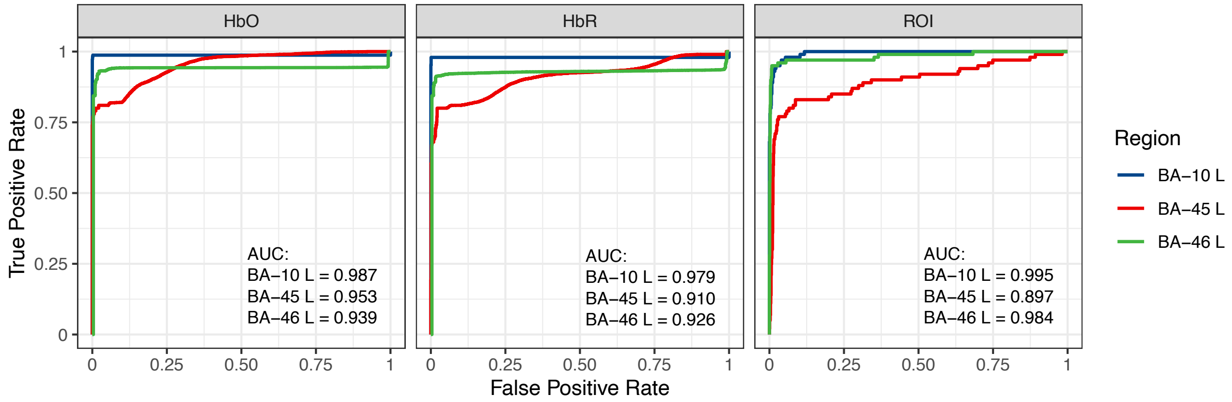

Figure 6.15: The ROI-ROC curves for the image reconstruction of the datasets with simulated activity in three different Brodmann Areas against the corresponding noise data. The three active regions are indicated by the line color, and the two levels of ROC curve are indicated by the title of the three panels – two at voxel level (HbO and HbR) and one at ROI level. The large AUCs indicate the good ROC performance of the Ba-FSOGL model on fNIRS image reconstruction.

In addition to the ROI-ROC performance, we also checked where FPs are easier to appear. Our hypothesis is that it is more common to see FPs in the neighboring regions next to the active region due to the low spatial resolution of fNIRS imaging. To test this hypothesis, we report the FPR in different regions when the TPR in the active region achieves 80% in Fig. 6.16, in which the subplots on the main diagonal of the plot matrix show the FPR in the contralateral ROI whereas the remaining subplots show that in the neighboring ROIs. As we can see, the FPRs in the contralateral ROIs are always smaller than those in the neighboring ROIs especially when BA-45 left is active. Therefore, our hypothesis is valid.

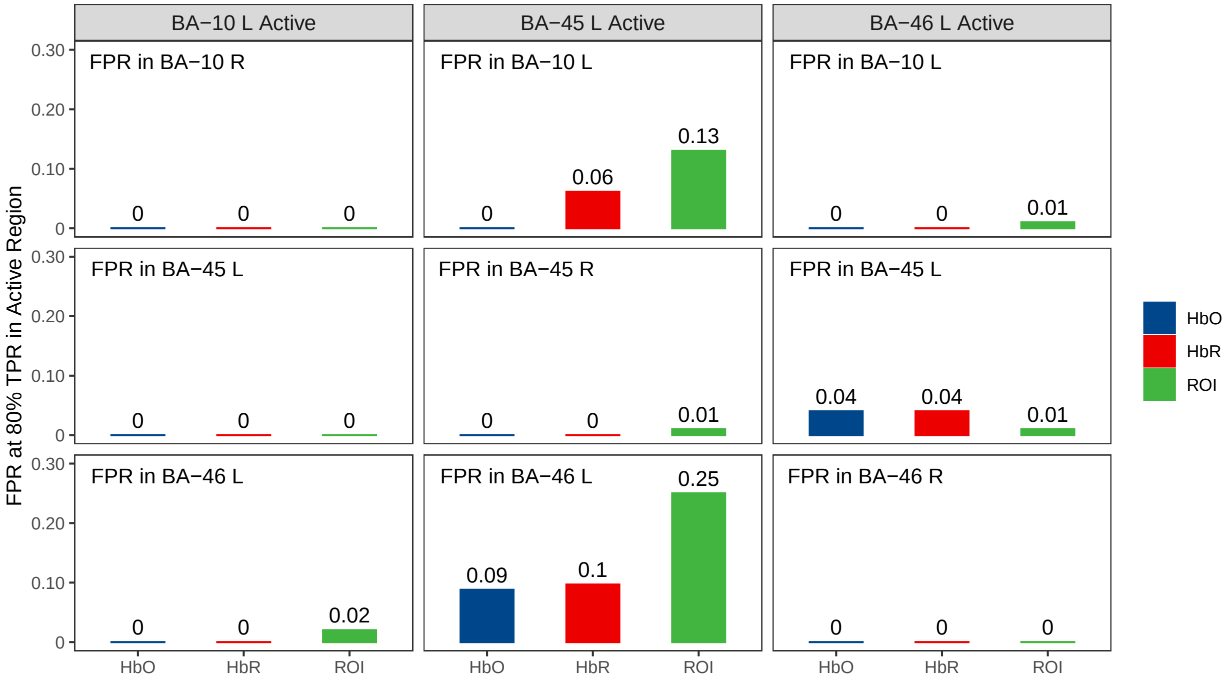

Figure 6.16: The bar chart showing the FPR in the region annotated at the up-left corner of each subplot when the TPR in the active region achieves 80%. The active region is indicated by the title of each column. The subplots on the main diagonal of the plot matrix show the FPR in the contralateral ROI whereas the remaining subplots show that in the neighboring ROIs. It can be seen that the FPRs in the contralateral ROIs are always smaller than those in the neighboring ROIs especially when BA-45 left is active.

6.5 Discussion

In this paper, we have described the proposed Ba-FSOGL model that involves anatomical and hemodynamics prior information in fNIRS image reconstruction and validated the model via numerical simulations. Now we will discuss the findings from the results in the following aspects.

6.5.1 Advantages of Ba-FSOGL

The model proposed in this paper combines several common regularization terms. Each of them applies a type of constraint to the model based on the prior information. The fused lasso penalty minimizes the difference between neighboring connected coefficients. The group lasso term selects or excludes variables in the same group as much as possible and maintains the correlation between variables. The sparse term allows every individual variable in a group to be selected or excluded. The variable transformation of overlapping group lasso resolves the overlapping challenge by converting the problem into an equivalent regular minimization. From the results we show in Section 6.4, we can see that the anatomy and hemodynamics priors are all reflected in the reconstructed images. Thus, we can conclude the penalty terms we include in the proposed model are all appropriate and necessary. In addition, we use the adaptive version of regularization in this model, which allows different tuning parameters for groups. This is also an important feature will be discussed in Section 6.5.2. Finally, the model is solved in a Bayesian framework, which has several advantages over frequentist approaches. First, the samples from the Markov chain can be used for uncertainty estimation and statistical inference. Second, the optimization of the tuning parameters is integrated into the Gibbs sampling process. Third, it is fairly easy to incorporate the prior information into the model by involving multiple level latent variables. Lastly, the hierarchical approach reduces the sensitivity of the latent variables to the measurement noise, especially in this high-dimensional inverse problem. Although the model's hierarchy is enough to include the prior information of fNIRS image reconstruction, it is straightforward to extend the model for a more complex problem if necessary. For example, if the measurement noise cannot be easily decorrelated via whitening transformation, we can extend the model by replacing the identity matrix in Eq.6.7 with the noise covariance matrix and adding an extra layer to model its pattern. Although we only validate this method using Brodmann parcellation as the anatomical prior, our model can actually handle different parcellation as long as the group membership of each β is reasonably determined. For instance, one may use the parcellation of motor cortex according to the motor homunculus for a movement-involved experiment. Besides the anatomy and hemodynamic prior information considered in this paper, some the other types of prior information can also be incorporated using this model. For example, taking the advantage of the adaptive tuning parameter, one may assign small penalty weight for the group representing the area that is expected to be active in the experiment, e.g., Broca's area for speech- or language-related tasks.

To sum up, each penalty term of the proposed Ba-FSOGL model appropriately incorporate a type of prior information of fNIRS image reconstruction. The Bayesian algorithm allows statistical inference and provides extensionality.

6.5.2 Convergence of the Algorithm

The convergence for the algorithm usually needs to be examined for MCMC-based approaches. Here we show an example trace plot of λ_g for a dataset containing brain activity in BA-46 left in Fig. 6.17.

It can be seen from the figure that the tuning parameter for the active region achieves a stable range while those for the inactive regions still increase at the end of the sampling chain. It looks diverging, however, the truth values of $\boldsymbol{\beta}_g$ for inactive regions are zero. Thus, the diverging tuning parameter indicates the estimates converges to the truth. We examined all the trace plots and found they are all similar to Fig. 6.17. Therefore, we would consider the algorithm successfully converges. This also proves that the use of the adaptive regularization is necessary, since it allows the tuning parameter for different regions to be different. Otherwise, the algorithm would be impossible to converge to the same results with an equal tuning parameter for all regions.

6.5.3 Missed voxels

It can be clearly seen from Fig. 6.11 and Fig. 6.13 that the image reconstruction of datasets containing brain activity in BA-10 and BA-46 left have several false negatives where the estimates of the hemoglobin changes for some active voxels are insignificant. The two voxels missed in the BA-10 left image reconstruction can be seen in the brain space (Fig. 6.7), which indicates in the truth image that there are two voxels on a different gyrus. The two voxels are not connected to any other voxels in the spatial structure encoding matrix for

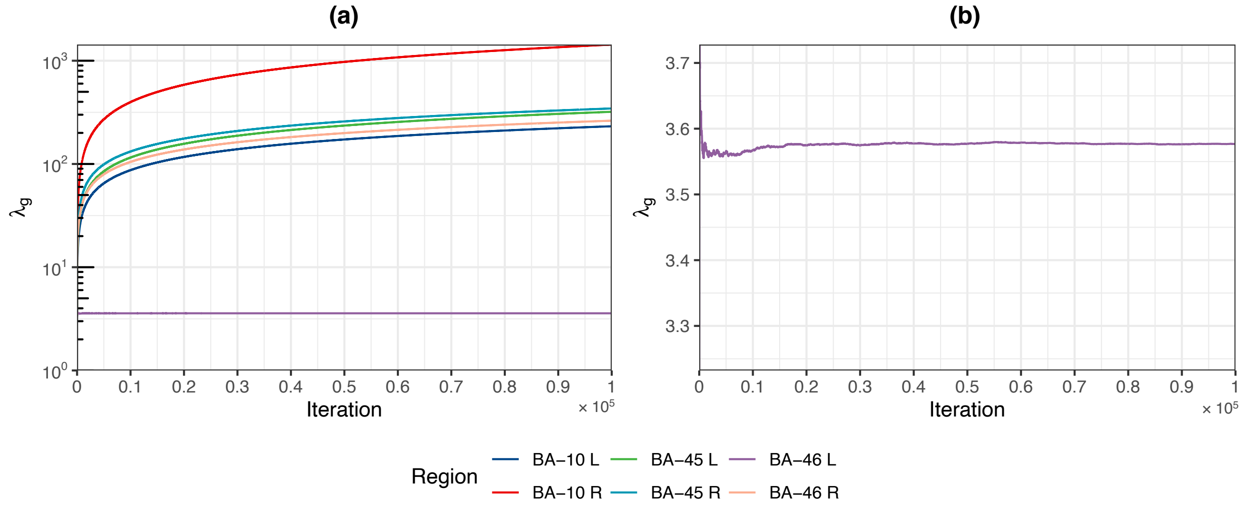

Figure 6.17: An example trace plot of λ_g for a dataset containing brain activity in BA-46 left. (a) plot the value of tuning parameters for all regions (indicated by the line color) in the log scale as a function of sampling iteration. (b) plot the value of the tuning parameter for the active region (BA-46 left in this example) in the original scale as a function of sampling iteration. It can be found from the plots that the tuning parameters of inactive regions increase as the sampling iteration while that of the active region fluctuates at the beginning and converges to a stable value at the end.

BA-10 left. Since they are not connected to the main part of the region and further from the probe than the main part, the regularization approach would tend to drop them as the estimates on them are larger but the difference between the main region is not constrained. The reason caused missed voxels in BA-46 left is the same, although they cannot be seen in the brain space (Fig. 6.9). The missed voxels are located on a layer under and not connected to the recovered part of BA-46 left either. Therefore, we can conclude that the missed voxels are caused by the anatomical prior information, and the algorithm does not have a problem.

6.5.4 Effects of Channel-space Prior

A question might be raised about the selection on the initial value of the tuning parameter. Since there is a possibility that the most active region indicated by channel-space ROI analysis is different from the truth, one may worry about the channel-space results mislead the image reconstruction model. In our simulation study using the 600 datasets, we also tried to provide the ground truth prior of the active region, which is impossible to known in a practical situation, to the image reconstruction model, however, the results do not change. In other words, the datasets leading the channel-space analysis a false active region are impossible to be correctly reconstructed regardless of the initial value of the tuning parameter. Thus, we can conclude that the prior information of active region provided by channel-space ROI analysis does not negatively affect the image reconstruction model.

6.5.5 Limitations and Future Plans

Although this paper demonstrates the good performance of the novelly proposed image reconstruction model – Ba-FSOGL, there are still several limitations. First, the Gibbs sampling algorithm is time consuming. As we mentioned in Section 6.4, this work costs about 30,000 hours in total, which cannot be completed without a computer cluster. Second, we assume only one region is active in the datasets. Since it is challenging for the channel-space analysis to compare the significance in a small active region and a larger region containing a small active region, we make this assumption at this point. Third, unlike a frequentist approach, there is no p-value reported by the Bayesian model, so cannot analyze the type-I error level of the model by comparing the empirical FPR to the type-I error control.

Therefore, the next steps of this work will include implementing this model using a faster optimization algorithm, investigating on a more effective approach to determine the initial value of tuning parameter, and a frequentist approach for statistical inference.

6.6 Conclusion

In this work, we propose a novel approach for fNIRS image reconstruction by combining multiple lasso-based regularizations and solving the model in a Bayesian framework. The model is validated via numerical simulation. The results of image reconstruction and statistical inference indicates the prior information on cerebral anatomy and hemodynamics is appropriately incorporated. The MSE, CNR, and ROC curves demonstrate the good performance of the model.

7.0 Conclusions and Future Works

The overall goal of this dissertation is to development statistical models that improve fNIRS imaging. In Chapter 1, we reviewed the challenges in fNIRS data analysis. First, a small change in brain anatomy or optical probe positioning can create huge differences in fNIRS measurements even though the underlying brain activity remains the same due to the existence of “blind-spots” when using a common nearest-neighbor probe. Second, fNIRS image reconstruction is a high-dimensional, ill-posed, and under-determined problem, in which there are thousands of parameters to estimate while only tens of measurements available and existing methods notably overestimate the false positive rate. The major contribution of this dissertation is to propose and validate novel statistical models addressing these two problems.

Chapter 2, 3, and 4 provide an overview of background knowledge relative to this project including the calculation of light propagation in brain tissues, existing models and methods for fNIRS data analyses, and statistical tools used in this dissertation.

The work presented in Chapter 5 investigates the non-involvement of specific cortex regions in an evoked task using an ROI-based statistical test. The method is implemented based on the definition of contrast in statistics, which is a linear combination of variables. In this chapter, a novel tapered contrast vector is proposed and compared with the conventionally used uniform contrast vector. The calculation of the tapered contrast vector depends on brain anatomy and probe registration. Simulation studies are conducted to validate this new method. The tapered and uniform vector are both used in the statistical test on a same simulated dataset. Two types of analysis are performed – analyses on single ROI and difference between ROIs – with different simulation parameters such as ROI size and distance. ROC curves are constructed for each method on each analysis. According to the significance testing on the AUC difference between the two methods, we find that the tapered contrast vector performs consistently better than the conventional uniform contrast vector in both types of analysis regardless of changes in simulation parameters. From the AUC change pattern across ROI size and distance, it can be found that the analysis results using the uniform contrast vector are remarkably affected by the "blind-spots" while this effect is reduced if the tapered contrast vector is used.

Chapter 6 explores the fNIRS image reconstruction problem by incorporating anatomical and physiological prior information that a specific region is usually active in an evoked task and the changes in HbO and HbR are negatively correlated. The prior information is conveyed via a penalty combination of fused and group lasso regularization. The fused lasso regularization constrains the difference of hemoglobin changes within a same ROI while the group lasso regularization controls the ROI level variable selection and maintains the correlation between HbO and HbR changes. The model is optimized in a Bayesian hierarchical modeling framework whose hyperparameters are determined by cross-validation using the channel-space ROI analysis results with the model described in Chapter 5. The method is also validated via numerical simulations. The results demonstrate that the new method successfully reconstructed the simulated images in most cases without generating excessive false positives.

To sum up, the two methods proposed in this dissertation properly addressed the two major challenges in fNIRS data analysis using statistical methods incorporating anatomical information of brain. However, they still have limitations and can be extended. First of all, an obvious future plan is to validate these two new methods using multi-modal clinical dataset. The other modality, such as fMRI, can be used as the ground truth. Considering the limitations of the proposed channel-space analysis, potential future plans are as follows. First, a close check on the underestimation of type-I error using small significance level. Although the overall performance is appropriate. solving this problem is necessary as smaller significance levels, e.g., 0.05, are commonly used. Second, the performance for the comparison of two ROIs is not good enough. There is still a large space for ROC AUC improvement. Third, the model is still based on a mis-registered probe when the registration information is unknown. An optimization of a common probe as a random effect across subjects could potentially improve the analysis further. Last, anatomical difference between subjects is not considered in this study. The validation of this method involving anatomy variation is expected. Regarding the limitations of the image reconstruction problem, we propose following future works. First, a single active regions is assumed in this project. A method searching for prior of multiple active regions will be useful for a more complicated situation. Second, the Bayesian modeling and MCMC algorithm is time-consuming. A better optimization method is required to perform a real-time analysis. Third, it can be extended to a group-level model using mixed-effects model where the group-level image and the deviation of subject-level images from it can be treated as a fixed- and random-effect respectively. Taking the advantages of Bayesian hierarchical modeling, two more layers for the individual random-effects can be easily inserted to the current subject-level image-reconstruction model. The group-level model is expected to handle variation in anatomy and probe registration across subjects.

Bibliography

[1] D. A. Boas, A. M. Dale, and M. A. Franceschini, “Diffuse optical imaging of brain activation: approaches to optimizing image sensitivity, resolution, and accuracy,” *Neuroimage*, vol. 23, pp. S275–S288, 2004.

[2] T. J. Huppert, M. S. Allen, S. G. Diamond, and D. A. Boas, “Estimating cerebral oxygen metabolism from fmri with a dynamic multicompartment windkessel model,” *Human brain mapping*, vol. 30, no. 5, pp. 1548–1567, 2009.

[3] R. N. Aslin and J. Mehler, “Near-infrared spectroscopy for functional studies of brain activity in human infants: promise, prospects, and challenges,” *Journal of biomedical optics*, vol. 10, no. 1, p. 011009, 2005.

[4] M. Ferrari and V. Quaresima, “A brief review on the history of human functional near-infrared spectroscopy (fnirs) development and fields of application,” *Neuroimage*, vol. 63, no. 2, pp. 921–935, 2012.

[5] V. Quaresima and M. Ferrari, “Functional near-infrared spectroscopy (fnirs) for assessing cerebral cortex function during human behavior in natural/social situations: a concise review,” *Organizational Research Methods*, vol. 22, no. 1, pp. 46–68, 2019.

[6] V. Quaresima and M. Ferrari, “A mini-review on functional near-infrared spectroscopy (fnirs): Where do we stand, and where should we go?,” in *Photonics*, vol. 6, p. 87, Multidisciplinary Digital Publishing Institute, 2019.

[7] A. Blasi, S. Lloyd-Fox, L. Katus, and C. E. Elwell, “fnirs for tracking brain development in the context of global health projects,” in *Photonics*, vol. 6, p. 89, Multidisciplinary Digital Publishing Institute, 2019.

[8] J. Gervain, J. Mehler, J. F. Werker, C. A. Nelson, G. Csibra, S. Lloyd-Fox, M. Shukla, and R. N. Aslin, “Near-infrared spectroscopy: a report from the mcdonnell infant methodology consortium,” *Developmental cognitive neuroscience*, vol. 1, no. 1, pp. 22–46, 2011.

[9] S. Lloyd-Fox, A. Blasi, and C. Elwell, “Illuminating the developing brain: the past, present and future of functional near infrared spectroscopy,” *Neuroscience & Biobehavioral Reviews*, vol. 34, no. 3, pp. 269–284, 2010.

[10] C. M. Aasted, M. A. Yücel, R. J. Cooper, J. Dubb, D. Tsuzuki, L. Becerra, M. P. Petkov, D. Borsook, I. Dan, and D. A. Boas, “Anatomical guidance for functional near-infrared spectroscopy: Atlasviewer tutorial,” *Neurophotonics*, vol. 2, no. 2, p. 020801, 2015.

[11] S. Lloyd-Fox, J. E. Richards, A. Blasi, D. G. Murphy, C. E. Elwell, and M. H. Johnson, “Coregistering functional near-infrared spectroscopy with underlying cortical areas in infants,” *Neurophotonics*, vol. 1, no. 2, p. 025006, 2014.

[12] L. Pollonini, H. Bortfeld, and J. S. Oghalai, “Phoebe: a method for real time mapping of optodes-scalp coupling in functional near-infrared spectroscopy,” *Biomedical optics express*, vol. 7, no. 12, pp. 5104–5119, 2016.

[13] D. Tsuzuki, D.-s. Cai, H. Dan, Y. Kyutoku, A. Fujita, E. Watanabe, and I. Dan, “Stable and convenient spatial registration of stand-alone nirs data through anchor-based probabilistic registration,” *Neuroscience Research*, vol. 72, no. 2, pp. 163–171, 2012.

[14] L. L. Emberson, J. E. Richards, and R. N. Aslin, “Top-down modulation in the infant brain: Learning-induced expectations rapidly affect the sensory cortex at 6 months,” *Proceedings of the National Academy of Sciences*, vol. 112, no. 31, pp. 9585–9590, 2015.

[15] J. A. Hanley and B. J. McNeil, “The meaning and use of the area under a receiver operating characteristic (roc) curve.,” *Radiology*, vol. 143, no. 1, pp. 29–36, 1982.

[16] A. Beer, “Bestimmung der absorption des rothen lichts in farbigen flussigkeiten,” *Ann. Physik*, vol. 162, pp. 78–88, 1852.

[17] J. H. Lambert, *Photometria sive de mensura et gradibus luminis, colorum et umbrae.* Klett, 1760.

[18] P. Bouguer, *Essai d’optique sur la gradation de la lumière.* chez Claude Jombert, ruë S. Jacques, au coin de la ruë des Mathurins, à l . . . , 1729.

[19] S. Prahl, “Optical absorption of hemoglobin.”

[20] A. P. A. T. R. C. R.L.P. van Veen, H.J.C.M. Sterenborg, "Optical absorption of fat."

[21] D. J. Segelstein, *The complex refractive index of water.* PhD thesis, University of Missouri–Kansas City, 1981.

[22] L. Wang, S. L. Jacques, and L. Zheng, "Mcml—monte carlo modeling of light transport in multi-layered tissues," *Computer methods and programs in biomedicine*, vol. 47, no. 2, pp. 131–146, 1995.

[23] S. L. Jacques, "Optical properties of biological tissues: a review," *Physics in Medicine & Biology*, vol. 58, no. 11, p. R37, 2013.

[24] J. Ripoll, "Derivation of the scalar radiative transfer equation from energy conservation of maxwell's equations in the far field," *JOSA A*, vol. 28, no. 8, pp. 1765–1775, 2011.

[25] Q. Fang and D. A. Boas, "Monte carlo simulation of photon migration in 3d turbid media accelerated by graphics processing units," *Optics express*, vol. 17, no. 22, pp. 20178–20190, 2009.

[26] E. Alerstam, W. C. Y. Lo, T. D. Han, J. Rose, S. Andersson-Engels, and L. Lilge, "Next-generation acceleration and code optimization for light transport in turbid media using gpus," *Biomedical optics express*, vol. 1, no. 2, pp. 658–675, 2010.

[27] N. Ren, J. Liang, X. Qu, J. Li, B. Lu, and J. Tian, "Gpu-based monte carlo simulation for light propagation in complex heterogeneous tissues," *Optics express*, vol. 18, no. 7, pp. 6811–6823, 2010.

[28] W. C. Y. Lo, T. D. Han, J. Rose, and L. Lilge, "Gpu-accelerated monte carlo simulation for photodynamic therapy treatment planning," in *European Conference on Biomedical Optics*, p. 7373_13, Optical Society of America, 2009.

[29] M. Schweiger, S. Arridge, M. Hiraoka, and D. Delpy, "The finite element method for the propagation of light in scattering media: boundary and source conditions," *Medical physics*, vol. 22, no. 11, pp. 1779–1792, 1995.

[30] S. Arridge, M. Schweiger, M. Hiraoka, and D. Delpy, "A finite element approach for modeling photon transport in tissue," *Medical physics*, vol. 20, no. 2, pp. 299–309, 1993.

[31] H. Santosa, X. Zhai, F. Fishburn, and T. Huppert, “The nirs brain analyzir toolbox,” *Algorithms*, vol. 11, no. 5, p. 73, 2018.

[32] T. J. Huppert, S. G. Diamond, M. A. Franceschini, and D. A. Boas, “Homer: a review of time-series analysis methods for near-infrared spectroscopy of the brain,” *Applied optics*, vol. 48, no. 10, pp. D280–D298, 2009.

[33] T. J. Huppert, “Commentary on the statistical properties of noise and its implication on general linear models in functional near-infrared spectroscopy,” *Neurophotonics*, vol. 3, no. 1, p. 010401, 2016.

[34] J. W. Barker, A. Aarabi, and T. J. Huppert, “Autoregressive model based algorithm for correcting motion and serially correlated errors in fnirs,” *Biomedical optics express*, vol. 4, no. 8, pp. 1366–1379, 2013.

[35] A. C. Whiteman, H. Santosa, D. F. Chen, S. B. Perlman, and T. Huppert, “Investigation of the sensitivity of functional near-infrared spectroscopy brain imaging to anatomical variations in 5-to 11-year-old children,” *Neurophotonics*, vol. 5, no. 1, p. 011009, 2017.

[36] F. Abdelnour, C. Genovese, and T. Huppert, “Hierarchical bayesian regularization of reconstructions for diffuse optical tomography using multiple priors,” *Biomedical optics express*, vol. 1, no. 4, pp. 1084–1103, 2010.

[37] R. A. Chowdhury, J. M. Lina, E. Kobayashi, and C. Grova, “Meg source localization of spatially extended generators of epileptic activity: comparing entropic and hierarchical bayesian approaches,” *PloS one*, vol. 8, no. 2, p. e55969, 2013.

[38] C. Grova, J. Daunizeau, J.-M. Lina, C. G. Bénar, H. Benali, and J. Gotman, “Evaluation of eeg localization methods using realistic simulations of interictal spikes,” *Neuroimage*, vol. 29, no. 3, pp. 734–753, 2006.

[39] C. Amblard, E. Lapalme, and J.-M. Lina, “Biomagnetic source detection by maximum entropy and graphical models,” *IEEE transactions on biomedical engineering*, vol. 51, no. 3, pp. 427–442, 2004.

[40] F. Tian, H. Niu, S. Khadka, Z.-J. Lin, and H. Liu, “Algorithmic depth compensation improves quantification and noise suppression in functional diffuse optical tomography,” *Biomedical Optics Express*, vol. 1, no. 2, pp. 441–452, 2010.

[41] T. Bhowmik, H. Liu, Z. Ye, and S. Oraintara, "Dimensionality reduction based optimization algorithm for sparse 3-d image reconstruction in diffuse optical tomography," *Scientific reports*, vol. 6, p. 22242, 2016.

[42] C. E. Metz, "Basic principles of roc analysis," in *Seminars in nuclear medicine*, vol. 8, pp. 283–298, WB Saunders, 1978.

[43] A. I. Bandos and N. A. Obuchowski, "Evaluation of diagnostic accuracy in free-response detection-localization tasks using roc tools," *Statistical Methods in Medical Research*, vol. 28, no. 6, pp. 1808–1825, 2019.

[44] N. A. Obuchowski, M. L. Lieber, and K. A. Powell, "Data analysis for detection and localization of multiple abnormalities with application to mammography," *Academic radiology*, vol. 7, no. 7, pp. 516–525, 2000.

[45] P. Bunch, B. PC, and S. GH, "A free-response approach to the measurement and characterization of radiographic-observer performance," 1978.

[46] D. P. Chakraborty, "A brief history of free-response receiver operating characteristic paradigm data analysis," *Academic radiology*, vol. 20, no. 7, pp. 915–919, 2013.

[47] D. P. Chakraborty, "Observer performance methods for diagnostic imaging," in *Imaging in Medical Diagnosis and Therapy*, CRC Press, 2017.

[48] D. P. Chakraborty, "Maximum likelihood analysis of free-response receiver operating characteristic (froc) data," *Medical physics*, vol. 16, no. 4, pp. 561–568, 1989.

[49] D. P. Chakraborty and L. Winter, "Free-response methodology: alternate analysis and a new observer-performance experiment.," *Radiology*, vol. 174, no. 3, pp. 873–881, 1990.

[50] D. P. Chakraborty and X. Zhai, "On the meaning of the weighted alternative free-response operating characteristic figure of merit," *Medical physics*, vol. 43, no. 5, pp. 2548–2557, 2016.

[51] E. R. DeLong, D. M. DeLong, and D. L. Clarke-Pearson, "Comparing the areas under two or more correlated receiver operating characteristic curves: a nonparametric approach," *Biometrics*, pp. 837–845, 1988.

[52] D. D. Dorfman, K. S. Berbaum, and C. E. Metz, "Receiver operating characteristic rating analysis: generalization to the population of readers and patients with the jackknife method," *Investigative radiology*, vol. 27, no. 9, pp. 723–731, 1992.

[53] S. L. Hillis, "A comparison of denominator degrees of freedom methods for multiple observer roc analysis," *Statistics in medicine*, vol. 26, no. 3, pp. 596–619, 2007.

[54] C. A. Roe and C. E. Metz, "Dorfman-berbaum-metz method for statistical analysis of multireader, multimodality receiver operating characteristic data: validation with computer simulation," *Academic radiology*, vol. 4, no. 4, pp. 298–303, 1997.

[55] N. A. Obuchowski Jr and H. E. Rockette Jr, "Hypothesis testing of diagnostic accuracy for multiple readers and multiple tests an anova approach with dependent observations," *Communications in Statistics-simulation and Computation*, vol. 24, no. 2, pp. 285–308, 1995.

[56] S. L. Hillis, N. A. Obuchowski, K. M. Schartz, and K. S. Berbaum, "A comparison of the dorfman–berbaum–metz and obuchowski–rockette methods for receiver operating characteristic (roc) data," *Statistics in medicine*, vol. 24, no. 10, pp. 1579–1607, 2005.

[57] S. L. Hillis and K. S. Berbaum, "Power estimation for the dorfman-berbaum-metz method1," *Academic radiology*, vol. 11, no. 11, pp. 1260–1273, 2004.

[58] S. L. Hillis, N. A. Obuchowski, and K. S. Berbaum, "Power estimation for multireader roc methods: an updated and unified approach," *Academic radiology*, vol. 18, no. 2, pp. 129–142, 2011.

[59] B. D. Gallas and S. L. Hillis, "Generalized roe and metz receiver operating characteristic model: analytic link between simulated decision scores and empirical auc variances and covariances," *Journal of Medical Imaging*, vol. 1, no. 3, p. 031006, 2014.

[60] S. L. Hillis, "A marginal-mean anova approach for analyzing multireader multicase radiological imaging data," *Statistics in medicine*, vol. 33, no. 2, pp. 330–360, 2014.

[61] N. A. Obuchowski, S. V. Beiden, K. S. Berbaum, S. L. Hillis, H. Ishwaran, H. H. Song, and R. F. Wagner, "Multireader, multicase receiver operating characteristic analysis:: an empirical comparison of five methods1," *Academic radiology*, vol. 11, no. 9, pp. 980–995, 2004.

[62] N. A. Obuchowski, B. D. Gallas, and S. L. Hillis, “Multi-reader roc studies with split-plot designs: a comparison of statistical methods,” *Academic radiology*, vol. 19, no. 12, pp. 1508–1517, 2012.

[63] C. E. Metz and X. Pan, ““proper” binormal roc curves: theory and maximum-likelihood estimation,” *Journal of mathematical psychology*, vol. 43, no. 1, pp. 1–33, 1999.

[64] X. Pan and C. E. Metz, “The “proper” binormal model: parametric receiver operating characteristic curve estimation with degenerate data,” *Academic radiology*, vol. 4, no. 5, pp. 380–389, 1997.

[65] L. L. Pesce and C. E. Metz, “Reliable and computationally efficient maximum-likelihood estimation of “proper” binormal roc curves,” *Academic radiology*, vol. 14, no. 7, pp. 814–829, 2007.

[66] D. D. Dorfman, K. S. Berbaum, and E. A. Brandser, “A contaminated binormal model for roc data: Part i. some interesting examples of binormal degeneracy,” *Academic radiology*, vol. 7, no. 6, pp. 420–426, 2000.

[67] D. D. Dorfman and K. S. Berbaum, “A contaminated binormal model for roc data: Part ii. a formal model,” *Academic Radiology*, vol. 7, no. 6, pp. 427–437, 2000.

[68] D. D. Dorfman and K. S. Berbaum, “A contaminated binormal model for roc data: Part iii. initial evaluation with detection roc data,” *Academic Radiology*, vol. 7, no. 6, pp. 438–447, 2000.

[69] C. E. Metz, P.-L. Wang, and H. B. Kronman, “A new approach for testing the significance of differences between roc curves measured from correlated data,” in *Information processing in medical imaging*, pp. 432–445, Springer, 1984.

[70] C. Metz, H. Kronman, J. Shen, and P. Wang, “Corroc2: a program for roc analysis of correlated, inherently categorical, rating-scale data,” *Department of Radiology, University of Chicago*, 1989.

[71] C. E. Metz, B. A. Herman, and C. A. Roe, “Statistical comparison of two roc-curve estimates obtained from partially-paired datasets,” *Medical Decision Making*, vol. 18, no. 1, pp. 110–121, 1998.

[72] X. Zhai and D. P. Chakraborty, “A bivariate contaminated binormal model for robust fitting of proper roc curves to a pair of correlated, possibly degenerate, roc datasets,” *Medical Physics*, vol. 44, no. 6, pp. 2207–2222, 2017.

[73] A. Gelman, J. B. Carlin, H. S. Stern, D. B. Dunson, A. Vehtari, and D. B. Rubin, *Bayesian data analysis*. CRC press, 2013.

[74] X. Zhai, H. Santosa, and T. J. Huppert, “Using anatomically defined regions-of-interest to adjust for head-size and probe alignment in functional near-infrared spectroscopy,” *Neurophotonics*, vol. 7, no. 3, p. 035008, 2020.

[75] K. Brodmann, *Brodmann's: Localisation in the cerebral cortex*. Springer Science & Business Media, 2007.

[76] M. Cope, D. Delpy, E. Reynolds, S. Wray, J. Wyatt, and P. Van der Zee, “Methods of quantitating cerebral near infrared spectroscopy data,” in *Oxygen Transport to Tissue X*, pp. 183–189, Springer, 1988.

[77] J. C. Ye, S. Tak, K. E. Jang, J. Jung, and J. Jang, “Nirs-spm: statistical parametric mapping for near-infrared spectroscopy,” *Neuroimage*, vol. 44, no. 2, pp. 428–447, 2009.

[78] S. Tak and J. C. Ye, “Statistical analysis of fnirs data: a comprehensive review,” *Neuroimage*, vol. 85, pp. 72–91, 2014.

[79] H. Dehghani, M. E. Eames, P. K. Yalavarthy, S. C. Davis, S. Srinivasan, C. M. Carpenter, B. W. Pogue, and K. D. Paulsen, “Near infrared optical tomography using nirfast: Algorithm for numerical model and image reconstruction,” *Communications in numerical methods in engineering*, vol. 25, no. 6, pp. 711–732, 2009.

[80] Q. Fang, “Mesh-based monte carlo method using fast ray-tracing in plücker coordinates,” *Biomedical optics express*, vol. 1, no. 1, pp. 165–175, 2010.

[81] C. J. Holmes, R. Hoge, L. Collins, R. Woods, A. W. Toga, and A. C. Evans, “Enhancement of mr images using registration for signal averaging,” *Journal of computer assisted tomography*, vol. 22, no. 2, pp. 324–333, 1998.

[82] E. T. Rolls, M. Joliot, and N. Tzourio-Mazoyer, “Implementation of a new parcellation of the orbitofrontal cortex in the automated anatomical labeling atlas,” *Neuroimage*, vol. 122, pp. 1–5, 2015.

[83] B. W. Zeff, B. R. White, H. Dehghani, B. L. Schlaggar, and J. P. Culver, "Retinotopic mapping of adult human visual cortex with high-density diffuse optical tomography," *Proceedings of the National Academy of Sciences*, vol. 104, no. 29, pp. 12169–12174, 2007.

[84] N. C. for Health Statistics, "Data table of infant head circumference-for-age charts."

[85] M. Jermyn, H. R. Ghadyani, M. A. Mastanduno, W. D. Turner, S. C. Davis, H. Dehghani, and B. W. Pogue, "Fast segmentation and high-quality three-dimensional volume mesh creation from medical images for diffuse optical tomography," *Journal of biomedical optics*, vol. 18, no. 8, p. 086007, 2013.

[86] S. Yan, A. P. Tran, and Q. Fang, "Dual-grid mesh-based monte carlo algorithm for efficient photon transport simulations in complex three-dimensional media," *Journal of Biomedical Optics*, vol. 24, no. 2, p. 020503, 2019.

[87] R. Yao, S. Yan, X. Intes, and Q. Fang, "Accelerating monte carlo forward model with structured light illumination via "photon sharing"(conference presentation)," in *Optical Tomography and Spectroscopy of Tissue XIII*, vol. 10874, p. 108740B, International Society for Optics and Photonics, 2019.

[88] L. Yu, F. Nina-Paravecino, D. R. Kaeli, and Q. Fang, "Scalable and massively parallel monte carlo photon transport simulations for heterogeneous computing platforms," *Journal of biomedical optics*, vol. 23, no. 1, p. 010504, 2018.

[89] J. J. Stott, J. P. Culver, S. R. Arridge, and D. A. Boas, "Optode positional calibration in diffuse optical tomography," *Applied optics*, vol. 42, no. 16, pp. 3154–3162, 2003.

[90] J. L. Lancaster, M. G. Woldorff, L. M. Parsons, M. Liotti, C. S. Freitas, L. Rainey, P. V. Kochunov, D. Nickerson, S. A. Mikiten, and P. T. Fox, "Automated talairach atlas labels for functional brain mapping," *Human brain mapping*, vol. 10, no. 3, pp. 120–131, 2000.

[91] J. Talairach and G. Szikla, "Application of stereotactic concepts to the surgery of epilepsy," in *Advances in Stereotactic and Functional Neurosurgery 4*, pp. 35–54, Springer, 1980.

[92] J. Talairach and P. Tournoux, "Co-planar stereotaxic atlas of the human brain. 1988," *Theime, Stuttgart, Ger*, vol. 270, no. 132, pp. 90128–5, 1988.

[93] S. R. Arridge, "Optical tomography in medical imaging," *Inverse problems*, vol. 15, no. 2, p. R41, 1999.

[94] M. Kyung, J. Gill, M. Ghosh, G. Casella, *et al.*, "Penalized regression, standard errors, and bayesian lassos," *Bayesian Analysis*, vol. 5, no. 2, pp. 369–411, 2010.

[95] C. Leng, M.-N. Tran, and D. Nott, "Bayesian adaptive lasso," *Annals of the Institute of Statistical Mathematics*, vol. 66, no. 2, pp. 221–244, 2014.

[96] Q. Li, N. Lin, *et al.*, "The bayesian elastic net," *Bayesian analysis*, vol. 5, no. 1, pp. 151–170, 2010.

[97] T. Park and G. Casella, "The bayesian lasso," *Journal of the American Statistical Association*, vol. 103, no. 482, pp. 681–686, 2008.

[98] X. Xu, M. Ghosh, *et al.*, "Bayesian variable selection and estimation for group lasso," *Bayesian Analysis*, vol. 10, no. 4, pp. 909–936, 2015.

[99] R. Tibshirani, "Regression shrinkage and selection via the lasso," *Journal of the Royal Statistical Society: Series B (Methodological)*, vol. 58, no. 1, pp. 267–288, 1996.

[100] A. E. Hoerl and R. W. Kennard, "Ridge regression: Biased estimation for nonorthogonal problems," *Technometrics*, vol. 12, no. 1, pp. 55–67, 1970.

[101] H. Zou and T. Hastie, "Regularization and variable selection via the elastic net," *Journal of the royal statistical society: series B (statistical methodology)*, vol. 67, no. 2, pp. 301–320, 2005.

[102] R. Tibshirani, M. Saunders, S. Rosset, J. Zhu, and K. Knight, "Sparsity and smoothness via the fused lasso," *Journal of the Royal Statistical Society: Series B (Statistical Methodology)*, vol. 67, no. 1, pp. 91–108, 2005.

[103] M. Yuan and Y. Lin, "Model selection and estimation in regression with grouped variables," *Journal of the Royal Statistical Society: Series B (Statistical Methodology)*, vol. 68, no. 1, pp. 49–67, 2006.

[104] N. Simon, J. Friedman, T. Hastie, and R. Tibshirani, "A sparse-group lasso," *Journal of computational and graphical statistics*, vol. 22, no. 2, pp. 231–245, 2013.

[105] P. Broca, “Remarques sur le siège de la faculté du langage articulé, suivies d’une observation d’aphémie (perte de la parole),” *Bulletin et Memoires de la Societe anatomique de Paris*, vol. 6, pp. 330–357, 1861.

[106] S. S. Keller, T. Crow, A. Foundas, K. Amunts, and N. Roberts, “Broca’s area: nomenclature, anatomy, typology and asymmetry,” *Brain and language*, vol. 109, no. 1, pp. 29–48, 2009.

[107] R. M. Lazar and J. Mohr, “Revisiting the contributions of paul broca to the study of aphasia,” *Neuropsychology review*, vol. 21, no. 3, p. 236, 2011.

[108] S.-Q. He, R. P. Dum, and P. L. Strick, “Topographic organization of corticospinal projections from the frontal lobe: motor areas on the medial surface of the hemisphere,” *Journal of Neuroscience*, vol. 15, no. 5, pp. 3284–3306, 1995.

[109] J. D. Meier, T. N. Aflalo, S. Kastner, and M. S. Graziano, “Complex organization of human primary motor cortex: a high-resolution fmri study,” *Journal of neurophysiology*, vol. 100, no. 4, pp. 1800–1812, 2008.

[110] G. S. Gandhoke, E. Belykh, X. Zhao, R. Leblanc, and M. C. Preul, “Edwin boldrey and wilder penfield’s homunculus: A life given by mrs. cantlie (in and out of realism),” *World Neurosurgery*, vol. 132, pp. 377–388, 2019.

[111] W. Penfield and E. Boldrey, “Somatic motor and sensory representation in the cerebral cortex of man as studied by electrical stimulation,” *Brain*, vol. 60, no. 4, pp. 389–443, 1937.

[112] H. Zou, “The adaptive lasso and its oracle properties,” *Journal of the American statistical association*, vol. 101, no. 476, pp. 1418–1429, 2006.

[113] V. Viallon, S. Lambert-Lacroix, H. Höfling, and F. Picard, “Adaptive generalized fused-lasso: Asymptotic properties and applications,” 2013.

[114] H. Wang and C. Leng, “A note on adaptive group lasso,” *Computational statistics & data analysis*, vol. 52, no. 12, pp. 5277–5286, 2008.

[115] G. Obozinski, L. Jacob, and J.-P. Vert, “Group lasso with overlaps: the latent group lasso approach,” *arXiv preprint arXiv:1110.0413*, 2011.

[116] D. Percival *et al.*, "Theoretical properties of the overlapping groups lasso," *Electronic Journal of Statistics*, vol. 6, pp. 269–288, 2012.

[117] J. C. Beer, H. J. Aizenstein, S. J. Anderson, and R. T. Krafty, "Incorporating prior information with fused sparse group lasso: Application to prediction of clinical measures from neuroimages," *Biometrics*, vol. 75, no. 4, pp. 1299–1309, 2019.

[118] Y. F. Atchadé, "A computational framework for empirical bayes inference," *Statistics and computing*, vol. 21, no. 4, pp. 463–473, 2011.

[119] N. Tzourio-Mazoyer, B. Landeau, D. Papathanassiou, F. Crivello, O. Etard, N. Delcroix, B. Mazoyer, and M. Joliot, "Automated anatomical labeling of activations in spm using a macroscopic anatomical parcellation of the mni mri single-subject brain," *Neuroimage*, vol. 15, no. 1, pp. 273–289, 2002.

[120] R. S. Desikan, F. Ségonne, B. Fischl, B. T. Quinn, B. C. Dickerson, D. Blacker, R. L. Buckner, A. M. Dale, R. P. Maguire, B. T. Hyman, *et al.*, "An automated labeling system for subdividing the human cerebral cortex on mri scans into gyral based regions of interest," *Neuroimage*, vol. 31, no. 3, pp. 968–980, 2006.

[121] M. F. Glasser, T. S. Coalson, E. C. Robinson, C. D. Hacker, J. Harwell, E. Yacoub, K. Ugurbil, J. Andersson, C. F. Beckmann, M. Jenkinson, *et al.*, "A multi-modal parcellation of human cerebral cortex," *Nature*, vol. 536, no. 7615, pp. 171–178, 2016.

[122] C. Rorden and M. Brett, "Stereotaxic display of brain lesions," *Behavioural neurology*, vol. 12, no. 4, pp. 191–200, 2000.